Controlled *n*-Doping of Naphthalene Diimide-Based Two-Dimensional Polymers

*Austin M. Evans, Kelsey A. Collins, Sangni Xun, Taylor G. Allen, Samik Jhulki, Ioannina Castano, Hannah L. Smith, Michael J. Strauss, Alexander K. Oanta, Lujia Liu, Lei Sun, Obadiah G. Reid, Gjergji Sini, Danilo Puggioni, James M. Rondinelli, Tijana Rajh, Nathan C. Gianneschi, Antoine Kahn, Danna E. Freedman, Hong Li, Stephen Barlow, Garry Rumbles, Jean-Luc Brédas, Seth R. Marder, William R. Dichtel***

A. M. Evans, K. A., Collins, I. Castano, M. J. Strauss, A. K. Oanta, L. Liu, N. C. Gianneschi, D. E. Freedman, W. R. Dichtel
Department of Chemistry, Northwestern University, Evanston, IL, 60208, USA
E-mail: wdichtel@northwestern.edu

S. Xun, S. Jhulki, S. Barlow, S.R. Marder
School of Chemistry and Biochemistry, Georgia Institute of Technology, Atlanta, GA, 30332, USA
Center for Organic Photonics and Electronics, Georgia Institute of Technology, Atlanta, GA, 30332, USA

S. Xun
College of Environmental Science and Engineering, Hunan University, Changsha 410082, P. R. China

T. G. Allen, O. G. Reid, G. Rumbles
Center for Chemistry and Nanoscience, National Renewable Energy Laboratory, 15013 Denver West Parkway, Golden, CO 80401, USA

H. L. Smith, A. Kahn
Department of Electrical Engineering, Princeton University, Princeton, NJ, 08544, USA

L. Sun, T. Rajh
Center for Nanoscale Materials, Argonne National Laboratory, Lemont, IL 60439, USA

O. G. Reid, G. Rumbles
Renewable and Sustainable Energy Institute, Department of Chemistry, University of Colorado Boulder, Boulder, CO 80309, USA

G. Sini, H. Li, J.-L. Brédas
Department of Chemistry and Biochemistry, The University of Arizona, Tucson, AZ 85721 USA,

G. Sini
CY Cergy Paris Université, Laboratoire de Physicochimie des Polymères et des Interfaces, EA 2528, 5 mail Gay-Lussac, Cergy-Pontoise Cedex, 95031, France.

D. Puggioni, J. R. Rondinelli, N.C. Gianneschi
Department of Materials Science and Engineering, Northwestern University, Evanston, IL 60208, USA

N.C. Gianneschi
International Institute for Nanotechnology, Department of Biomedical Engineering, Department of Pharmacology, Simpson Querrey Institute, and Chemistry of Life Processes Institute, Evanston, IL 60208, USA

Keywords: Organic semiconductor, two-dimensional polymers, *n*-type molecular doping, conductive polymers

Abstract

Two-dimensional polymers (2DPs) are promising as structurally well-defined, permanently porous, organic semiconductors. However, 2DPs are nearly always isolated as closed shell organic species with limited charge carriers, which leads to low bulk conductivities. Here, we enhance the bulk conductivity of two naphthalene diimide (NDI)-containing 2DP semiconductors by controllably *n*-doping the NDI units using cobaltocene ($CoCp_2$). Optical and transient microwave spectroscopy reveals that both as-prepared NDI-containing 2DPs are semiconducting with <2 eV optical bandgaps and photoexcited charge-carrier lifetimes of tens of nanoseconds. Following reduction with $CoCp_2$, both 2DPs largely retain their periodic structures and exhibit optical and electron-spin resonance spectroscopic features consistent with the presence of NDI-radical anions. While the native NDI-based 2DPs are electronically insulating, substoichiometric levels of *n*-doping lead to maximum bulk conductivities of $>10^{-4}$ S cm^{-1}. Density functional theory calculations show that the strongest electronic couplings in these 2DPs exist in the out-of-plane (π-stacking) crystallographic directions, which indicates that cross-plane electronic transport through NDI stacks is primarily responsible for the observed electronic conductivity. Taken together, this study underlines that controlled molecular doping is a useful approach to access structurally well-defined, paramagnetic, 2DP *n*-type semiconductors with measurable bulk electronic conductivities of interest for electronic or spintronic devices.

Manuscript

Two-dimensional polymers (2DPs) are macromolecular sheets that combine permanent porosity with long-range order.[1] This periodicity enables the deterministic placement of chemical functionality in porous organic materials. This structural regularity, in principle, can lead to tailored emergent electronic and magnetic phenomena that are of interest for electronic and spintronic devices.[1, 2, 3] For example, computational and spectroscopic investigations have exposed that long-lived charge-separated states exist in some semiconducting 2DPs.[1, 3, 4, 5] However, the experimentally measured electronic conductivities of 2DPs are low, which have historically limited fundamental investigations and the use of 2DPs in some applications. Low conductivities are expected for most high-quality 2DPs, as a low number of free charge carriers is expected in closed shell organic systems with bandgaps >1 eV. Even when free charge carriers can be deliberately introduced through doping, many 2DPs exhibit low conductivities, likely attributable to the poor conjugation afforded by many 2D polymerization chemistries and/or the high densities of trap states in defect-prone materials. Addressing the long-standing challenge of developing highly conductive 2DPs that are porous, structurally precise, organic semiconductors is of potential interest for many devices including chemical sensors,[6] optoelectronics,[7] spin-valves,[8] and thermoelectrics.[9]

Electrical doping with molecular redox agents can be used to increase conductivity by chemical oxidation (*p*-doping) or reduction (*n*-doping) both through increasing the number of charge carriers and increasing the mobility of charge carriers by filling trap states.[10, 11] Despite the development of molecular doping techniques for organic molecules and linear polymers, doping of 2DPs has not been extensively investigated.[11, 12, 13] Currently, experimental 2DP doping efforts have focused on *p*-type doping,[14] primarily using I_2 vapor as an oxidant,[5] a method which provides little control over the number of free carriers introduced into these materials.[15], [16] Here, we explore controlled *n*-doping using cobaltocene ($CoCp_2$) that is introduced in well-defined stoichiometric amounts and undergoes an exergonic redox process with semiconducting 2DPs (**Figure 1**). This controlled *n*-doping enables an unprecedented systematic investigation of 2DP electronic and magnetic properties at precise carrier densities.

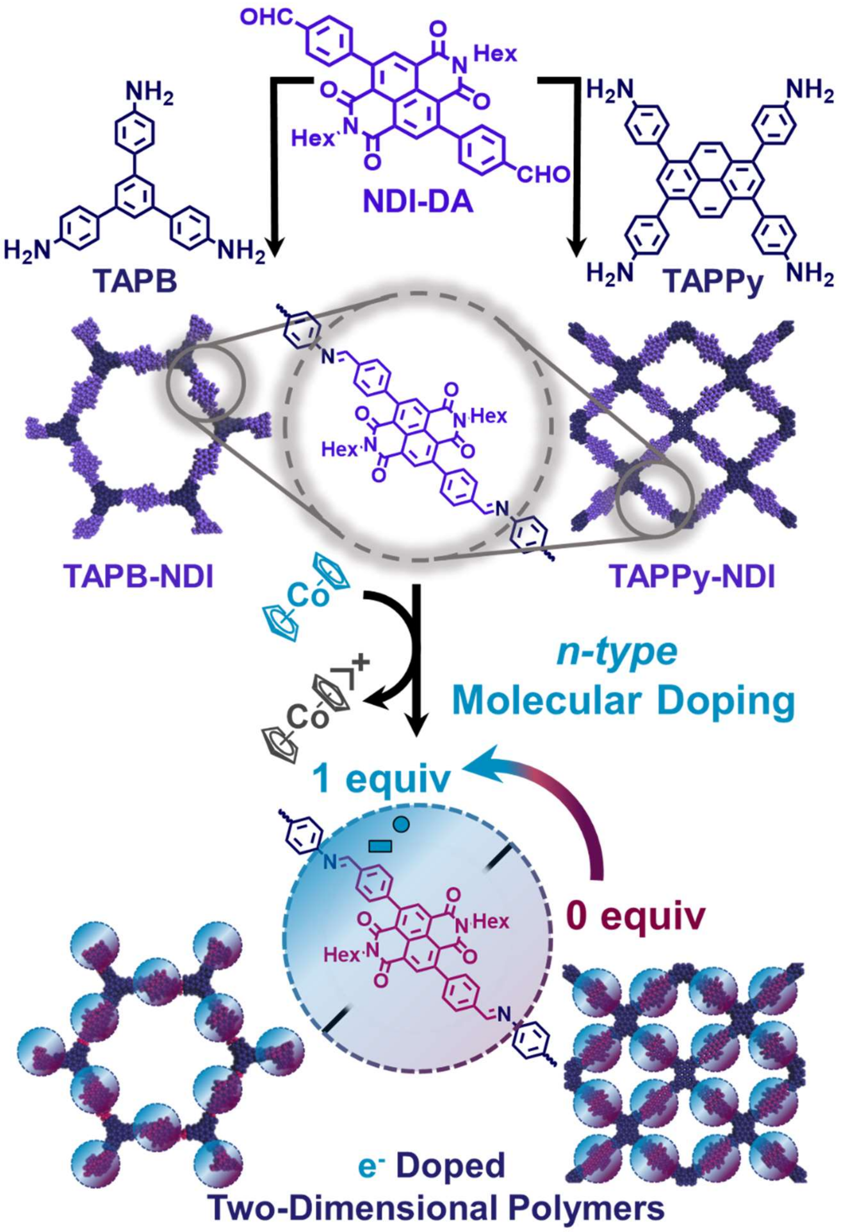

Figure 1. Synthesis of redox-active NDI-containing 2DPs followed by doping with defined stoichiometric amounts of molecular $CoCp_2$ (*n*-doping). The arrow from 0 to 1 equiv signifies the ability to systematically tune the amounts of NDI radical anions within the 2DP by changing the added amount of $CoCp_2$.

We synthesized two semiconducting 2DPs that contain naphthalene diimide (NDI) moieties and then *n*-doped them in defined stoichiometric amounts using $CoCp_2$ (**Figure 1**). $CoCp_2$ is only capable of singly reducing NDI-species within the polymer to NDI-radical anions (NDI$^{\bullet-}$), thus producing paramagnetic *n*-doped 2DPs. One critical feature is that both 2DPs retain their crystallinity after doping, thus yielding structurally defined, organic semiconductors with well-controlled numbers of charge carriers. Maximum electronic conductivities of >10^{-4} S cm^{-1} are observed at substoichiometric doping levels.[17] Although π-bridges were incorporated between adjacent NDI units to promote in-plane coupling, in keeping with the prevalent design paradigm for electronically active 2DPs to-date, computational and experimental studies suggest that electronic coupling is stronger, and thus electronic conductivity is larger, in the inter-plane π-stacking direction.[18] These conductivities are observed despite appreciable in-plane conjugation, which has been the prevalent design focus for electronically active 2DPs to-date. Taken together, controlled molecular doping is shown to be a powerful strategy to access paramagnetic 2DP semiconductors, which are of interest for organic electronic and spintronic devices.

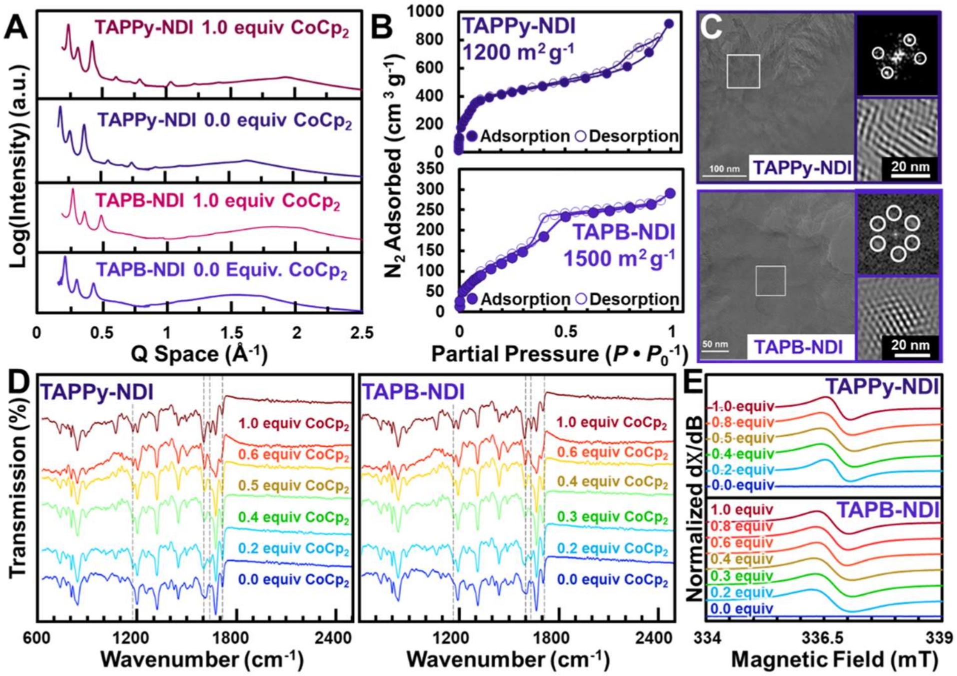

Figure 2. Chemical and structural characterization of undoped and *n*-doped 2DPs. **A)** Synchrotron X-ray diffraction of both as-synthesized undoped and fully doped (1 equiv $CoCp_2$ per NDI) NDI-based 2DPs. **B)** N_2 sorption isotherms for TAPPy-NDI (top) and TAPB-NDI (bottom). **C)** High-resolution transmission electron micrograph of TAPPy-NDI (top) and TAPB-NDI (bottom) with a Fourier-transform of a particular region (white box insets in Figure 2C, top right) and a band-

pass filtered image of that region (bottom right). **D)** Fourier-transform infrared spectra of 2DPs variably doped with $CoCp_2$. **E)** Continuous-wave electron paramagnetic resonance spectra of pristine and variably doped NDI-based 2DPs.

NDI was chosen as the electron acceptor for our studies because its well-defined reduction potentials are accessible by many molecular reductants, as well as being suitable for many organic semiconductor applications, leading to its extensive exploration in devices.[19] We have recently reported two-imine linked 2DPs based on a 3,7-di(4-formylphenyl)-functionalized NDI (NDI-DA) with different topologies; the condensation product of NDI-DA with 1,3,6,8-tetrakis(4-aminophenyl)pyrene (TAPPy, **Figure S7**) under acetic acid-catalyzed conditions has a tetragonal lattice – TAPPy-NDI – and was reported as an example in a study of synthesis and isolation methodology,[20] while the product of NDI-DA and 1,3,5-tris(4-aminophenyl)benzene (TAPB, **Figure S6**) has a hexagonal lattice – TAPB-NDI –and was studied as a lithium-ion battery material.[21] Both of these NDI-containing materials are suitable for *n*-doping studies and were resynthesized as high-quality polycrystalline powders using slightly modified conditions (**Figure S6** and **Figure S7**). Synchrotron X-ray diffraction (XRD) patterns collected at 13.3 keV (0.93 Å) of both TAPB-NDI and TAPPy-NDI powders have many sharp higher-order diffraction features (**Figure 2A**). The Pawley refined unit cells of the expected hexagonal TAPB-NDI lattice and tetragonal TAPPy-NDI lattice were found to match well with the respective experimental powder diffraction patterns.[22] When finite grain size feature broadening of the powder X-ray diffraction was considered, the average in-plane crystallographic length of both 2DPs was determined to be approximately 100 nm, consistent with current reports of high-quality 2DP powders.[23] Both 2DPs exhibited type IV N_2 isotherms with negligible hysteresis and high surface areas, which are representative of high quality materials. Brunauer-Emmet-Teller surface area analysis performed on these isotherms yield surface areas of 1500 m^2 g^{-1} and 1200 m^2 g^{-1} for TAPB-NDI and TAPPy-NDI, respectively (**Figure 2B**). From these N_2 isotherms, sharp pore size distributions centered at 2.9 nm and 3.4 nm were extracted for TAPB-NDI and TAPPy-NDI, both of which are consistent with their Pawley refined pore-structures. Transmission electron microscopy (TEM) images of both 2DPs corroborate that these powders are isolated as crystalline sheets with lateral dimensions of 100 nm (**Figure 2C** and **Figure S15**-**Figure S22**). Two-dimensional Fouriertransforms and band-pass filtered images of the TEM images are used to determine that hexagonally and tetragonally symmetric networks are isolated for TAPB-NDI and TAPPy-NDI, respectively (**Figure 2C insets**). Following polymerization and isolation, Fourier-transform infrared (FT-IR) spectroscopy exposed the emergence of the expected imine stretching frequency at 1670 cm^{-1} (**Figure 2D**). The amine (3000 cm^{-1}) and aldehyde (1710 cm^{-1}) FT-IR signals were reduced upon polymerization, which is consistent with the formation of imine bonds (**Figure S8** and **Figure S9**).[24] These measurements unambiguously demonstrate that both TAPB-NDI and TAPPy-NDI are prepared as highly crystalline powders with minimal unreacted functionalities.

Cobaltocene was used to singly reduce the incorporated NDI units to introduce unpaired electrons into both networks. Redox potentials evaluated by cyclic voltammetry (**Figure S50**) reveal that NDI units within the 2DP have a redox potentials (-0.9 V vs. $FeCp_2$) similar to molecular NDIs, which suggests that complete one electron reduction to the radical anion ($NDI^{\bullet-}$) by $CoCp_2$ (-1.3 V vs. $FeCp_2$)[25] is expected. Both 2DPs were *n*-doped by immersing a known amount of polycrystalline powder into $CoCp_2$ THF solutions for at least 16 h under a N_2 atmosphere (**Figure S23**). The 2DPs were then recovered by filtration, rinsed with deoxygenated THF, and characterized, all under an inert atmosphere. After introducing controlled substoichiometric amounts of $CoCp_2$, we observe an immediate and pronounced darkening of both NDI-based 2DPs. As both 2DPs are doped with increasing amounts of $CoCp_2$, a feature at 1720 cm^{-1} disappears and a feature at 1620 cm^{-1} appears, both of which are consistent with reduction of NDI to $NDI^{\bullet-}$ (**Figure 2D** and **Figure S10**). Double reduction NDI subunits to NDI^{2-} (-1.6 V vs. $FeCp_2$) by $CoCp_2$ is unexpected based on the redox potentials of molecular NDIs,[19, 25] which is consistent with cyclic voltammetry measurements of NDI-containing frameworks and the observation that infrared spectra of frameworks that had 2 equiv. of $CoCp_2$ added are indistinguishable from those to which 1 equiv of $CoCp_2$ are added.

Prior to doping with $CoCp_2$ both 2DPs give no signal when examined using continuous-wave electron paramagnetic resonance (CW-EPR) spectroscopy, as is expected for closed shell diamagnetic organic polymers. After doping both 2DPs with any amount of $CoCp_2$, a pronounced CW-EPR signal was observed. Simulation of the spectra with the Hamiltonian, $\hat{H} = g_{iso}\mu_B \boldsymbol{SH}$, yields values of 2.0042 ± 0.0001 for g_{iso}, for both TAPPY-NDI and TAPB-NDI. The simulation matches well with the experimental data and the g_{iso} tensors are consistent with NDI-centered radicals (**Figure 2E** and **Figures S41-47**). The semi-quantitative CW-EPR intensity of this feature is found to linearly increase with the quantity of $CoCp_2$ used until high doping levels, after which spin-spin interactions decrease the measured EPR intensity (**Figure S48** and **Figure S49**). Taken together, these results establish that NDIs within the 2DP can be singly reduced by exposure to controlled amounts of $CoCp_2$.

After complete reduction (1.0 equiv $CoCp_2$), the X-ray diffraction patterns of both 2DPs change only slightly (**Figure 2A**), which indicates that the lattice is not substantially perturbed by the presence of embedded $NDI^{\bullet-}$ radical anions or the $CoCp_2^+$ counterions, which are presumably located in the channels and along the periphery of 2DP crystallites. However, minor shifts of the in-plane diffraction feature (0.1 Å^{-1}< Q Space <0.5 Å^{-1}) to lower scattering vector and the out-of-plane diffraction feature (1.5 Å^{-1}< Q Space <2.5 Å^{-1}) to higher scattering vector are observed. This suggests that to accommodate the charges, counterions, and changes in bond length produced upon doping, the lattice becomes slightly more planar with tighter interlayer packing. These results demonstrate that NDI-based 2DPs with variable numbers of electronic carriers and paramagnetic centers can be produced through exposure to $CoCp_2$.

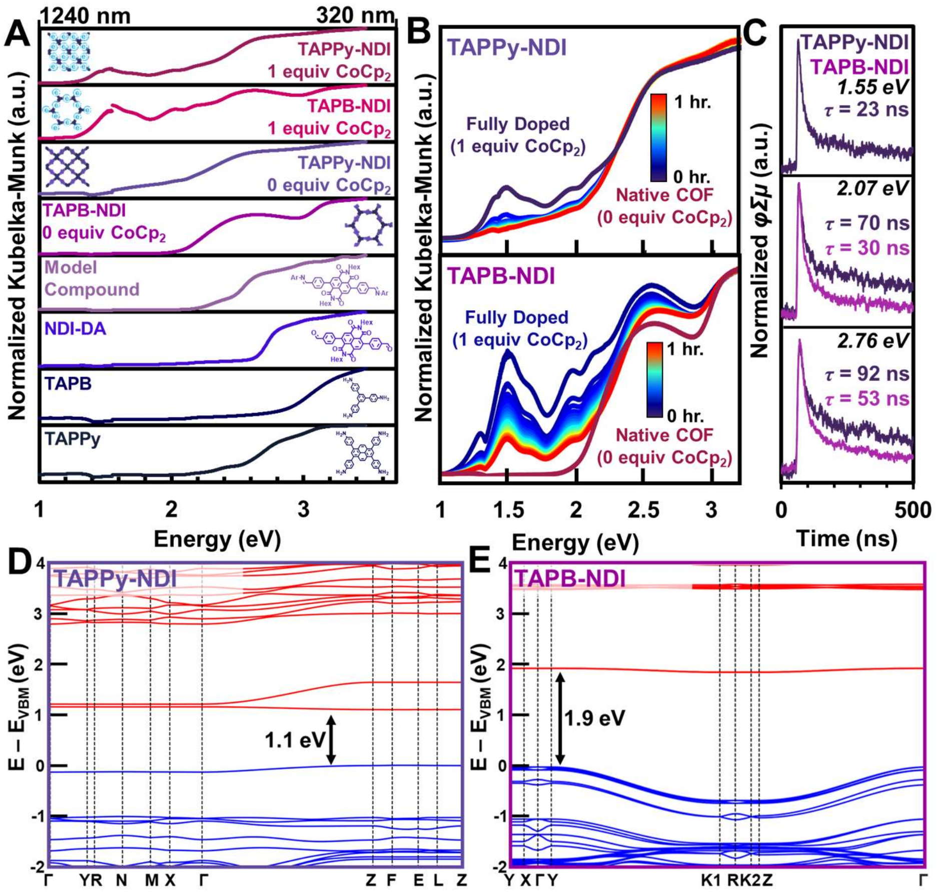

Figure 3. Optical characterization of monomers, model compounds, pristine 2DPs, and doped 2DPs and electronic structure of pristine 2DPs. A) Diffuse-reflectance ultraviolet-visible-near-IR spectroscopy of monomers, model compound, pristine NDI-containing 2DPs, and fully doped (1.0 equiv. $CoCp_2$ per NDI) NDI-containing 2DPs. The discontinuities in the spectra at 1.4 eV are due to a detector change-over within the instrument. **B)** Diffuse-reflectance ultraviolet-visible-near-IR spectroscopy during temporal evolution of fully doped NDI-containing 2DPs to entirely undoped upon exposure to air. **C)** Time-resolved flash-photolysis microwave conductivity of both pristine NDI-containing 2DPs and their charge-carrier lifetimes, inset text shows the excitation wavelength and the average amplitude-weighted lifetime, $\langle\tau\rangle$. **D)** Electronic band structures calculated at the PBE0 density functional theory level for pristine multilayer TAPPy-NDI and **E.** TAPB-NDI (valence bands in blue; conduction bands in red).

Both NDI-based 2DPs were found to have moderate energy optical transitions (<2 eV) in their undoped and doped states. Tauc analysis,[26] which is performed by extrapolating the linear region of absorbance to the abscissa, of diffuse-reflectance ultraviolet-visible (DR-UVVis) spectroscopy showed that powders of the NDI-DA, TAPB, and TAPPy monomers all have optical transitions above 2.25 eV, which likely originate from isolated molecular electronic transitions (and not infinitely delocalized electronic bands) (**Figure 3A** and **Figure S29**. By condensing NDI-DA with 4-*tert*-butylaniline, we determined that imine formation shifted the absorption edge of NDI-DA by 0.30 eV, consistent with both enhanced conjugation and charge-transfer behavior across an aromatic imine. However, 2D polymerization produced pronounced electronic shifts (>0.6 eV) to yield optical transitions of 1.8 eV and 1.3 eV for TAPB-NDI and TAPPy-NDI (**Figure 3A, Figure S26**). The electronic structure of pristine TAPPy-NDI was also confirmed by ultraviolet and inverse photoelectron spectroscopy (UPS and IPES), which showed a single-particle gap of 1.57 eV for this material (**Figure S27**). Electrostatic charging precluded this analysis for TAPB-NDI. These spectroscopic characterizations demonstrate that more electronically delocalized structures, likely in the cross-plane direction *vide infra*, are produced during polymerization of NDIs into a layered 2D polymer.

Flash-photolysis time-resolved microwave conductivity (fp-TRMC) measurements indicate that both 2DPs are intrinsically semiconducting and exhibit long-lived free charge carriers. Fp-TRMC operates by exciting undoped 2DPs with a laser pulse and then monitoring the 9GHz microwave absorption of photoinduced charge carriers, which then allows the product of charge carrier yield (φ) and the sum of their mobilities ($\Sigma\mu = \mu_{electron} + \mu_{hole}$) to be extracted (denoted as $\varphi\Sigma\mu$, **Figure S28** and **Supporting Information Section J**). Additionally, by monitoring the transient microwave absorption, the lifetimes of photoinduced charge carriers can be extracted in a contactless manner. When excited at 2.76 eV (450 nm) and 2.07 eV (600 nm), TAPPy-NDI and TAPB-NDI both showed appreciable photoconductivity with $\varphi\Sigma\mu$ values of *ca.* 5×10^{-5} cm^{2}V^{-1}s^{-1} (**Figure 3C**). When excited at 1.55 eV (800 nm), only the TAPPy-NDI exhibited a measurable photoconductivity ($\varphi\Sigma\mu$ of *ca.* 5×10^{-5} cm^{2}V^{-1}s^{-1}, **Figure S3029**, **Figure S30**, and **Tables S2-S3**), consistent with the lower energy optical bandgap of TAPPy-NDI assessed by DR-UVVis. Global biexponential fp-TRMC transients for both 2DPs at all photon energies are characterized by a short time component (τ_1, *ca.* 4 - 12 ns) over which a large reduction in free carrier population occurs and a longer one (τ_2, *ca.* 290 - 400 ns) characteristic of the charges that remain. Compared to the global biexponential fit parameters for TAPB-NDI, TAPPy-NDI generally showed a slightly smaller τ_1 lifetime component (by ~40%) at 2.07 and 2.76 eV. In contrast, TAPPy-NDI's τ_2 was larger than TAPB-NDI's by ~100 ns at each photon energy (**Figure 3C** and **Table S3**). For both 2DPs, τ_1 and τ_2 decreased with decreasing photon energy with τ_1 generally becoming more heavily weighted; suggesting that the fast dynamics increasingly dominate our fp-TRMC transients with lower energy excitation (**Figure S31**). Although various factors could explain the biexponential nature of these transients, the dynamics are consistent with sizeable trapping rate constants for either electrons or holes that quickly (≤12 ns) fill trap states with complementary longer-lived charge carriers (*ca.* 290 - 400 ns).[27] This is consistent with TEM images that reveal ill-defined 2DP particles indicative of structural defects that may introduce potential trap states. The photoconductivity of these NDI-based 2DPs is substantially different from its monomer species, highlighting how periodic arrays of chromophores can facilitate charge transport (See **Supporting Information Section J**). Overall, fp-TRMC measurements suggest that both NDI-based 2DPs are intrinsic semiconductors.

To gain insight into the electronic structure of the NDI-containing 2DPs, we performed electronic-structure calculations using density functional theory (DFT) (see **Supporting Information Section K** for the details of the DFT computational methodology). Briefly, the bulk crystal structures were optimized at the PBE level with the D3 van der Waals (vdW) dispersion corrections (**Table S4**); the band structures were then calculated using the PBE0 functional. The conduction band edges of both 2DPs (**Figure 3D** and **3E**) are dispersionless along the in-plane directions owing to poor in-plane conjugation from the large dihedral angles between the NDI moieties and the TAPPy or TAPB moieties. Along the out-of-plane directions (Γ-Z), there appears a weak dispersion in the lowest conduction band, 0.05 and 0.07 eV for TAPPy-NDI and TAPB-NDI, respectively, which is indicative of a weak electronic coupling among NDI fragments due to π-π stacking. This small dispersion implies that both NDI 2DPs are expected to exhibit hopping-type transport between localized redox sites in the out-of-plane direction. The calculations point to direct bandgaps ($E_{CB} - E_{VB}$) of 1.1 eV and 1.9 eV for TAPPy-NDI (**Figure 3D**) and TAPB-NDI (**Figure 3E**), respectively, both of which are qualitatively consistent with the optical absorption and fp-TRMC measurements. [28] To further characterize the inter-layer *vs*. intra-layer effects on the 2DP electronic structure, we also calculated the electronic band structure for monolayers of TAPB-NDI and TAPPy-NDI (**Figure S36**-**Figure S37**). In the absence of multilayer stacking, the bottom conduction (and top valence) bands are entirely flat and larger band gaps are obtained, which confirms that the intra-layer coupling among NDI units is vanishingly small. Therefore, ordered interlayer stacking is necessary to achieve significant electronic conductivities in these NDI-based 2DPs. In order to describe the nature of the optical gaps in the two NDI-based 2DPs, we analyzed the projected densities of states (PDOS) and simulated the optical absorption spectra (**Figure S32**). The weak and broad absorption peaks in both 2DPs display a charge-transfer character, associated with a transition from the top valence bands, dominated by contributions from the TAPPy/TAPB cores, to the bottom conduction bands, dominated by contributions from the NDI linkers.

When fully doped (1.0 equiv $CoCp_2$ per NDI) TAPB-NDI and TAPPy-NDI exhibit the emergence of 1.25 eV and 1.15 eV optical transitions, respectively, both of which are consistent with the presence of $NDI^{\bullet-}$ subunits observed by electron paramagnetic resonance spectroscopy.[29],[30] When exposed to air, $NDI^{\bullet-}$ is known to oxidize back to its native state (NDI),[19] which we observed over the course of one hour for $NDI^{\bullet-}$-containing frameworks using FT-IR spectroscopy (**Figure S11-Figure S14**). Therefore, continually collecting DR-UVVis spectra of a fully doped 2DP sample while the sample is exposed to air allows us to examine many intermediate doped states within a single experiment. As both 2DPs are exposed to air, we find that the optical absorption features associated with the $NDI^{\bullet-}$ state gradually decrease. Similarly, the FT-IR spectra and XRD patterns of doped NDI-containing 2DPs following oxidation are indistinguishable from those of the pristine material. These findings suggest that $NDI^{\bullet-}$-containing 2DPs have low energy optical transitions and can be chemically reduced and then re-oxidized without significant chemical or structural degradation. The combination of theoretical calculations and static- and transient-optical spectroscopies motivated us to interrogate the bulk electronic conductivity of *n*-doped 2DP semiconductors.

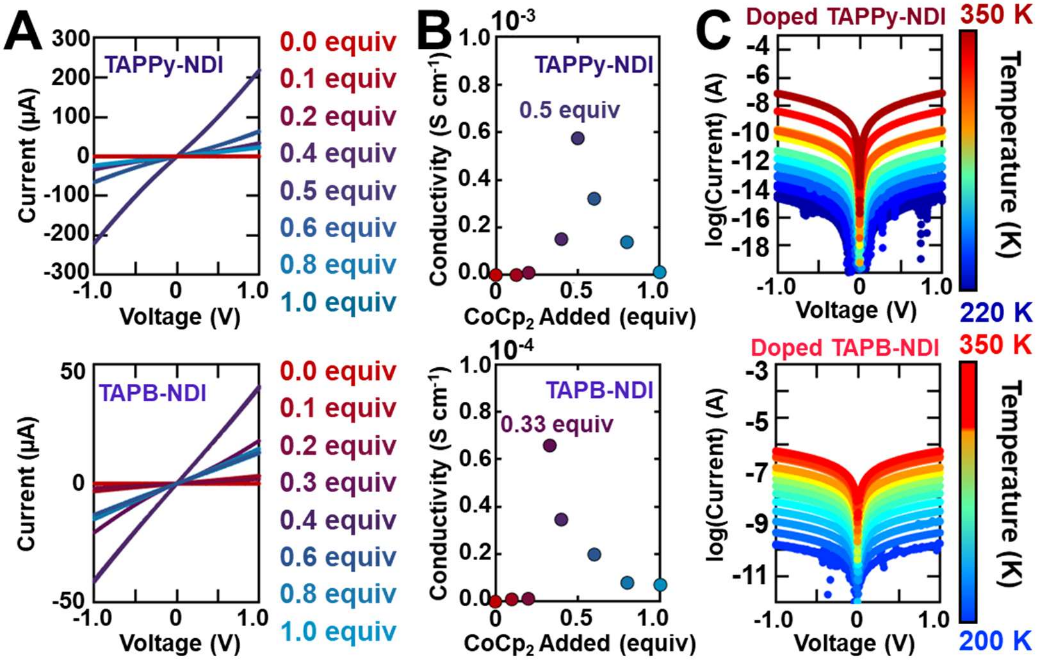

Figure 4. Conductivity measurements of controllably doped NDI-containing 2DPs. **A)** Current-voltage measurements of variably doped TAPPy-NDI (top) and TAPB-NDI (bottom) and **B)** extracted conductivities from **A**. **C)** Temperature-dependent conductivity of TAPPy-NDI (0.5 equiv $CoCp_2$, top) and of TAPB-NDI (1.0 equiv $CoCp_2$, bottom).

Two-probe pressed pellet conductivity measurements show that both 2DPs become several orders-of-magnitude more conductive upon doping. To measure the room-temperature bulk electronic conductivity of NDI-based 2DPs, powders were gently pressed between two copper rods in a nitrogen atmosphere and current was measured as a function of applied bias, with several voltage sweeps in both polarization directions (**Figure 4A** and **Figure S38**). In all cases, no hysteresis was observed, which led us to treat these pressed pellets as idealized Ohmic resistors (**Figure S39**). From this analysis, undoped TAPB-NDI and TAPPy-NDI are both found to be insulating with conductivities of <10^{-9} S cm^{-1}, which is consistent with expectations of chemically pure intrinsic semiconductors with greater than 1 eV bandgaps at room temperature (**Figure 4A-B**). The electronic conductivities gradually increased to a maximum of 6×10^{-4} S cm^{-1} for TAPPy-NDI and 7×10^{-5} S cm^{-1} for TAPB-NDI as charge-carriers are contributed by chemical reduction (**Figure 4A-B**). This order-of-magnitude difference in conductivity is qualitatively consistent with DFT calculation and spectroscopic measurements that show more delocalized character and longer lived charge-carriers, consistent with larger relative carrier mobilities, in TAPPy-NDI. In both cases, maximum conductivity is observed at substoichiometric $CoCp_2$ doping, with TAPB-NDI having an optimal doping of 0.33 equiv $CoCp_2$ and TAPPy-NDI having an optimal doping of 0.50 equiv $CoCp_2$, which likely reflects a balancing of charge carrier density and open hopping sites that is commonly observed in semiconducting polymers. This finding highlights another advantage of controlled stoichiometric doping, for which optimal charge carrier concentrations can be reliably targeted.

Variable-temperature conductivity experiments indicate a thermally activated process. As the temperature is decreased by 100 K, the electronic conductivity of both doped 2DPs decreases over 5 orders-of-magnitude (**Figure 4C**) following an Arrhenius relationship with temperature (**Figure S40**, again consistent with a hopping mechanism, which is frequently observed when redox-active sites within weakly dispersive bands are held in close proximity, such as the van der Waals contact in the macromolecular sheets studied here.[18] However, more mechanistic analysis is necessary to definitively determine the charge-transport pathways that lead to the temperature-enhanced electronic conductivities observed here.

The maximum conductivities demonstrated at these substoichiometric doping levels are comparable with those obtained in many studies of doped linear NDI polymers, although falling short of the highest values reported for NDI-containing polymers.[31] However, they are substantially lower than the highest conductivity values reported for the most developed *p*- (>10^4 S cm^{-1})[12, 32] and *n*-doped (>90 S cm^{-1})[33], [34] organic materials. The low density of electronically active NDI-sites, their weak electronic couplings, and the substantial porosity of the 2DPs reported here explain, at least in part, this difference in electronic conductivity. However, there exists substantial design potential to enhance the subunit electronic coupling either in-plane or out-of-plane, both of which would increase the bulk electronic conductivity of 2DPs. Specifically, this report demonstrates that moderate electronic conductivities, comparable to those in similar linear polymers, can be realized by intimate van der Waals contact, which can likely be systematically engineered in macromolecular sheets. Finally, the isotropic bulk conductivities reported here are likely diminished by the pressed pellet sample geometry, which are limited by the least conductive crystallographic direction and are significantly deteriorated due to interfacial resistance at the electrodes and particle boundaries. Therefore, it is conceivable that intrinsic intracrystallite transport may be significantly higher than the bulk values observed here. To address these limitations, future studies should aim to improve 2DP molecular design and better control 2DP morphology (*e.g.* synthesis as highly crystalline and oriented thin films), both of which are expected to enhance bulk conductivities.

This report demonstrates that paramagnetic, semiconducting 2DPs with meaningful electronic transport can be accessed by controlled molecular doping. More importantly, this approach enables the systematic investigation of paramagnetic and electronic behavior in covalently linked crystalline organic systems at controlled carrier densities, which is critical for the advancement of electronic 2DP design. As such, controlled molecular doping of 2DPs is a promising strategy that will undoubtedly inspire future investigations of other chemically and topologically distinct redox-active 2DPs and their associated electronic and spintronic devices.

Methods

General 2DP doping procedure: polycrystalline powders (typically 25-50 mg) were preweighed into prelabeled vials under a N_2 atmosphere. Then, separately, a $CoCp_2$ solution was prepared at a known concentration in anhydrous THF (See **Table S1** below for representative calculation details). Then, a volume of this molecular dopant solution was added to the powders in amounts to target the desired doping ratio. Nearly immediately the undoped powders were found to transform from a light yellow orange to a dark burgundy. 2DP powders then sat undisturbed within the dopant solution for at least 16 h. These solutions were then filtered and rinsed extensively (50 mL) with clean solvent THF.

Synchrotron X-ray Diffraction. Synchrotron powder X-ray diffraction was collected at either Sector 5 or 12 of the Advanced Photon Source, Argonne National Lab. All two-dimensional frames were collected in a transmission geometry then summed and radially integrated to produce a linear PXRD pattern using proprietary software available at the APS. The sample-to-detector distance was adjusted to measure across relevant detection ranges of q. Scattering intensity is reported as a function of the modulus of the scattering vector Q, related to the scattering angle 2θ by the equation $Q = (4\pi/\lambda) \sin \theta$, where λ is the x-ray wavelength.

Two-probe pressed pellet measurements: Powders were loaded into a hollowed glass rod. The powders were finger tightened between the rods and the two copper bars were then equipped to a potentiostat. We ran several potential sweeps in both bias directions to check for hysteretic behavior. In all cases, we observed no hysteresis, which led us to consider these materials as idealized Ohmic resistors. At the end of the experiment, we measured the length of the pressed pellet using dial calipers by measuring the difference of the full assembly with and without the powders. This distance, with the obtained IV curves, was used to evaluate the Ohmic resistance.

Electron paramagnetic resonance measurements: Continuous wave electron paramagnetic resonance (CW-EPR) spectra were acquired using a Bruker ELEXYS E500 spectrometer operating at X-band (9.4 GHz) frequencies with an Oxford ESR900 He flow cryostat with an ITC-5025 temperature controller and a Bruker High QE (HQE) cavity resonator (ER 4122SHQE).

Supporting Information

Supporting Information is available from the Wiley Online Library or the author.

Acknowledgements

We thank the Army Research Office for a Multidisciplinary University Research Initiatives (MURI) award under grant W911NF-15-1-0447, which supported the preparation of electroactive 2DPs, their optical characterization, and their study using density functional theory. We also thank the Department of Energy grant DE-SC0019356 for supporting efforts at controlled molecular doping, including the investigation of charge transport, electronic structure, and paramagnetic behavior. A.M.E. (DGE-1324585), K.A.C. (DGE-1842165), I.C. (DGE-11842165), M.J.S (DGE-11842165) are supported by the National Science Foundation Graduate Research Fellowship. S.J. thanks the United States-India Educational Foundation (USIEF, India) and the Institute of International Education (IIE, USA) for a Fulbright-Nehru Postdoctoral Fellowship (grant no. 2266/FNPDR/2017). Work in Princeton was supported in part by a grant of the National Science Foundation (DMR-1807797) (H.L.S and A.K.) and by a National Science Foundation Graduate Research Fellowship (DGE-1656466) (H.L.S.). This study made use of the IMSERC and EPIC at Northwestern University, both of which have received support from the Soft and Hybrid Nanotechnology Experimental (SHyNE) Resource (NSF NNCI-1542205 and NSF ECCS1542205, respectively), the Materials Research Science and Engineering Center (NSF DMR-1720139), the State of Illinois, and the International Institute for Nanotechnology (IIN). Portions of this work were performed at the DuPont-Northwestern-Dow Collaborative Access Team (DND-CAT) located at Sector 5 and Sector 8 of the Advanced Photon Source (APS). DND-CAT is supported by Northwestern University, E.I. DuPont de Nemours & Co., and the Dow Chemical Company. This research used resources of the Advanced Photon Source and Center for Nanoscale Materials, both U.S. Department of Energy (DOE) Office of Science User Facilities operated for the DOE

Office of Science by Argonne National Laboratory under contract DE-AC02-06CH11357, and the National Energy Research Scientific Computing Center, a DOE Office of Science User Facility supported by the Office of Science of the U.S. Department of Energy under Contract No. DE-AC02-05CH11231. Resources at the Advanced Photon Source were funded by NSF under award 0960140. This work was authored by the National Renewable Energy Laboratory, operated by Alliance for Sustainable Energy, LLC, for the U.S. Department of Energy (DOE) under Contract No. DE-AC36-08GO28308. Funding for microwave measurements was provided by Department of Energy, Office of Basic Energy Sciences, Division of Chemical Sciences, Biosciences, and Geosciences. The views expressed in the article do not necessarily represent the views of the DOE or the U.S. Government. The U.S. Government retains and the publisher, by accepting the article for publication, acknowledges that the U.S. Government retains a nonexclusive, paid-up, irrevocable, worldwide license to publish or reproduce the published form of this work, or allow others to do so, for U.S. Government purposes. T.G.A and G.R. thank Obadiah Reid for helpful discussions regarding microwave measurements.

Conflict of Interest

The authors declare no competing interests.

References

[1] K. Geng, T. He, R. Liu, S. Dalapati, K. T. Tan, Z. Li, S. Tao, Y. Gong, Q. Jiang, D. Jiang, *Chem. Rev.* **2020**, *120*, 8814.

[2] Y. Yusran, Q. Fang, V. Valtchev, *Adv. Mater.* **2020**, 2002038; A. P. Cote, A. I. Benin, N. W. Ockwig, M. O'Keeffe, A. J. Matzger, O. M. Yaghi, *Science* **2005**, *310*, 1166.

[3] M. Dogru, T. Bein, *Chem. Comm.* **2014**, *50*, 5531.

[4] S. Jin, X. Ding, X. Feng, M. Supur, K. Furukawa, S. Takahashi, M. Addicoat, M. E. El-Khouly, T. Nakamura, S. Irle, S. Fukuzumi, A. Nagai, D. Jiang, *Angew. Chem. Int. Ed.* **2013**, *125*, 2071; X. Ding, L. Chen, Y. Honsho, X. Feng, O. Saengsawang, J. Guo, A. Saeki, S. Seki, S. Irle, S. Nagase, V. Parasuk, D. Jiang, *J. Am. Chem. Soc.* **2011**, *133*, 14510; D. D. Medina, M. L. Petrus, A. N. Jumabekov, J. T. Margraf, S. Weinberger, J. M. Rotter, T. Clark, T. Bein, *ACS Nano* **2017**, *11*, 2706; N. Keller, D. Bessinger, S. Reuter, M. Calik, L. Ascherl, F. C. Hanusch, F. Auras, T. Bein, *J. Am. Chem. Soc.* **2017**, *139*, 8194; B. Sun, C.-H. Zhu, Y. Liu, C. Wang, L.-J. Wan, D. Wang, *Chem. Mater.* **2017**, *29*, 4367; T. Sick, A. G. Hufnagel, J. Kampmann, I. Kondofersky, M. Calik, J. M. Rotter, A. Evans, M. Döblinger, S. Herbert, K. Peters, D. Böhm, P. Knochel, D. D. Medina, D. Fattakhova-Rohlfing, T. Bein, *J. Am. Chem. Soc.* **2017**, *140*, 2085;

M. Dogru, M. Handloser, F. Auras, T. Kunz, D. Medina, A. Hartschuh, P. Knochel, T. Bein, *Angew. Chem. Int. Ed.* **2013**, *125*, 2992; D. Bessinger, L. Ascherl, F. Auras, T. Bein, *J. Am. Chem. Soc.* **2017**, *139*, 12035; G. H. Bertrand, V. K. Michaelis, T.-C. Ong, R. G. Griffin, M. Dincă, *Proc. Nat. Acad. Sci.* **2013**, *110*, 4923; T. Li, W.-D. Zhang, Y. Liu, Y. Li, C. Cheng, H. Zhu, X. Yan, Z. Li, Z.-G. Gu, *J. Mat. Chem. A* **2019**, *7*, 19676.

[5] S. Wan, J. Guo, J. Kim, H. Ihee, D. Jiang, *Angew. Chem. Int. Ed.* **2009**, *48*, 5439; E. Jin, M. Asada, Q. Xu, S. Dalapati, M. A. Addicoat, M. A. Brady, H. Xu, T. Nakamura, T. Heine, Q. Chen, D. Jiang, *Science* **2017**, *357*, 673; V. Lakshmi, C.-H. Liu, M. Rajeswara Rao, Y. Chen, Y. Fang, A. Dadvand, E. Hamzehpoor, Y. Sakai-Otsuka, R. S. Stein, D. F. Perepichka, *J. Am. Chem. Soc.* **2020**, *142*, 2155.

[6] S. Jhulki, A. M. Evans, X.-L. Hao, M. W. Cooper, C. H. Feriante, J. Leisen, H. Li, D. Lam, M. C. Hersam, S. Barlow, W. R. Dichtel, S. R. Marder, *J. Am. Chem. Soc.* **2020**, *142*, 783; A. M. Evans, N. P. Bradshaw, B. Litchfield, M. J. Strauss, B. Seckman, M. R. Ryder, I. Castano, C. Gilmore, N. C. Gianneschi, C. R. Mulzer, M. C. Hersam, W. R. Dichtel, *Adv. Mater.* **2020**, *32*, 2004205; L. Ascherl, E. W. Evans, J. Gorman, S. Orsborne, D. Bessinger, T. Bein, R. H. Friend, F. Auras, *J. Am. Chem. Soc.* **2019**, *141*, 15693.

[7] S. Fratini, M. Nikolka, A. Salleo, G. Schweicher, H. Sirringhaus, *Nat. Mater.* **2020**; B. Lussem, C.-M. Keum, D. Kasemann, B. Naab, Z. Bao, K. Leo, *Chem. Rev.* **2016**, *116*, 13714.

[8] J. Devkota, R. Geng, R. C. Subedi, T. D. Nguyen, *Adv. Func. Mater.* **2016**, *26*, 3881.

[9] B. Russ, A. Glaudell, J. J. Urban, M. L. Chabinyc, R. A. Segalman, *Nat. Rev. Mater.* **2016**, *1*, 1.

[10] K. Walzer, B. Maennig, M. Pfeiffer, K. Leo, *Chem. Rev.* **2007**, *107*, 1233; S. Barlow, S. R. Marder, X. Lin, F. Zhang, A. Kahn, in *Conjugated Polymers: Properties, Processing, and Applications*, 2019.

[11] I. E. Jacobs, A. J. Moulé, *Adv. Mater.* **2017**, *29*, 1703063; I. Salzmann, G. Heimel, M. Oehzelt, S. Winkler, N. Koch, *Acc. Chem Res.* **2016**, *49*, 370.

[12] Y. Yamashita, J. Tsurumi, M. Ohno, R. Fujimoto, S. Kumagai, T. Kurosawa, T. Okamoto, J. Takeya, S. Watanabe, *Nature* **2019**, *572*, 634.

[13] H. Li, H. Li, S. Xun, J.-L. Brédas, *Chem. Mater.* **2020**, *32*, 9228.

[14] J. M. Rotter, R. Guntermann, M. Auth, A. Mähringer, A. Sperlich, V. Dyakonov, D. D. Medina, T. Bein, *Chem. Sci.* **2020**, *11*, 12843.

[15] Q. Zhang, M. Dai, H. Shao, Z. Tian, Y. Lin, L. Chen, X. C. Zeng, *ACS Appl. Mater. Interfaces* **2018**, *10*, 43595.

[16] I_2 is a not an ideal dopant because it is challenging to introduce in controlled amounts, has an oxidation potential not well-matched with most aromatic systems, is volatile and desorbs over time, and produces an I_3^- counterion that is itself electronically conductive. These factors complicate understanding of the electronic properties of 2DPs doped with iodine.

[17] J. Petersen, C. Schramm, D. Stojakovic, B. M. Hoffman, T. J. Marks, *J. Am. Chem. Soc.* **1977**, *99*, 286.

[18] L. S. Xie, G. Skorupskii, M. Dincă, *Chem. Rev.* **2020**.

[19] M. Al Kobaisi, S. V. Bhosale, K. Latham, A. M. Raynor, S. V. Bhosale, *Chem. Rev.* **2016**, *116*, 11685.

[20] C. H. Feriante, S. Jhulki, A. M. Evans, R. R. Dasari, K. Slicker, W. R. Dichtel, S. R. Marder, *Adv. Mater.* **2020**, *32*, 1905776.

[21] S. Jhulki, C. H. Feriante, R. Mysyk, A. M. Evans, A. Magasinski, A. S. Raman, K. Turcheniuk, S. Barlow, W. R. Dichtel, G. Yushin, S. R. Marder, *ACS Appl. Energy Mater.* **2020**.

[22] G. Pawley, *J. Appl. Crystallogr.* **1981**, *14*, 357.
[23] M. C. Daugherty, E. Vitaku, R. L. Li, A. M. Evans, A. D. Chavez, W. R. Dichtel, *Chem. Commun.* **2019**, *55*, 2680.
[24] Although the signal at 1710 cm–1, corresponding to the aldehyde C=O stretching mode, does not completely disappear, this is attributable to overlap with a carbonyl stretching mode of the NDI core
[25] N. G. Connelly, W. E. Geiger, *Chem. Rev.* **1996**, *96*, 877.
[26] T. Sick, A. G. Hufnagel, J. Kampmann, I. Kondofersky, M. Calik, J. M. Rotter, A. Evans, M. Doeblinger, S. Herbert, K. Peters, D. Boehm, P. Knochel, D. D. Medina, D. Fattakhova-Rohlfing, T. Bein, *J. Am. Chem. Soc.* **2018**, *140*, 2085.
[27] A. C. Jakowetz, T. F. Hinrichsen, L. Ascherl, T. Sick, M. Calik, F. Auras, D. D. Medina, R. H. Friend, A. Rao, T. Bein, *J. Am. Chem. Soc.* **2019**, *141*, 11565.
[28] V. Coropceanu, J. Cornil, D. A. da Silva Filho, Y. Olivier, R. Silbey, J.-L. Brédas, *Chem. Rev.* **2007**, *107*, 926.
[29] Cobaltecinium is weakly absorbing in the visible, with a peak at 405 nm and an extinction coefficient of only 200 M^-1 cm^-1. This highlights an advantage of CoCp2 for systematic studies of controlled doping in NDI systems.
[30] G. Andric, J. F. Boas, A. M. Bond, G. D. Fallon, K. P. Ghiggino, C. F. Hogan, J. A. Hutchison, M. A.-P. Lee, S. J. Langford, J. R. Pilbrow, *Aust. J. Chem.* **2004**, *57*, 1011.
[31] J. Liu, L. Qiu, R. Alessandri, X. Qiu, G. Portale, J. Dong, W. Talsma, G. Ye, A. A. Sengrian, P. C. Souza, *Adv. Mater.* **2018**, *30*, 1704630.
[32] K. Kang, S. Watanabe, K. Broch, A. Sepe, A. Brown, I. Nasrallah, M. Nikolka, Z. Fei, M. Heeney, D. Matsumoto, *Nat. Mater.* **2016**, *15*, 896; V. Vijayakumar, Y. Zhong, V. Untilova, M. Bahri, L. Herrmann, L. Biniek, N. Leclerc, M. Brinkmann, *Adv. Energy Mater.* **2019**, *9*, 1900266.
[33] Y. Lu, J.-Y. Wang, J. Pei, *Chem. Mater.* **2019**, *31*, 6412.
[34] Y. Lu, Z. D. Yu, H. I. Un, Z. F. Yao, H. Y. You, W. Jin, L. Li, Z. Y. Wang, B. W. Dong, S. Barlow, S. R. Marder, J. Pei, **2021**, *33*, 2005946.

Figures and Captions

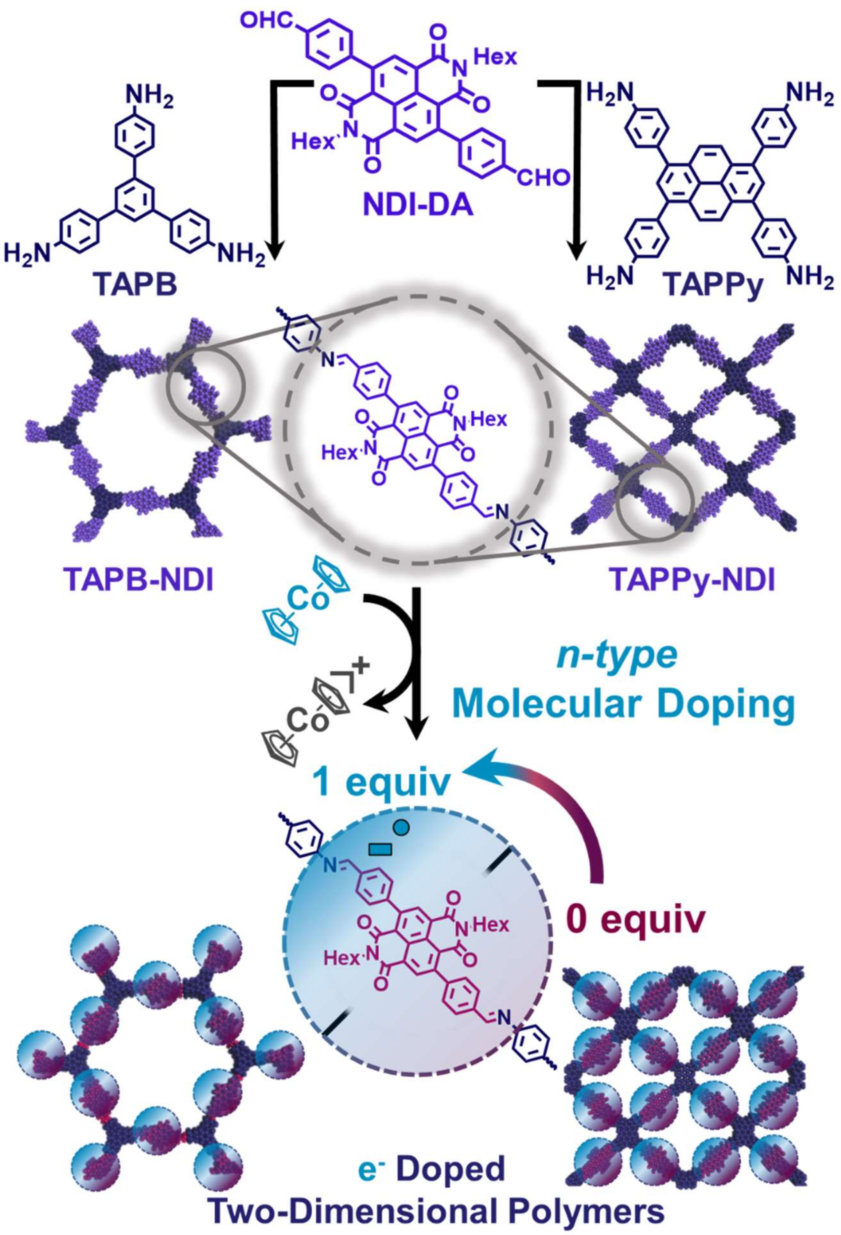

Figure 1. Synthesis of redox-active NDI-containing 2DPs followed by doping with defined stoichiometric amounts of molecular $CoCp_2$ (*n*-doping). The arrow from 0 to 1 equiv signifies the ability to systematically tune the amounts of NDI radical anions within the 2DP by amount of $CoCp_2$ added.

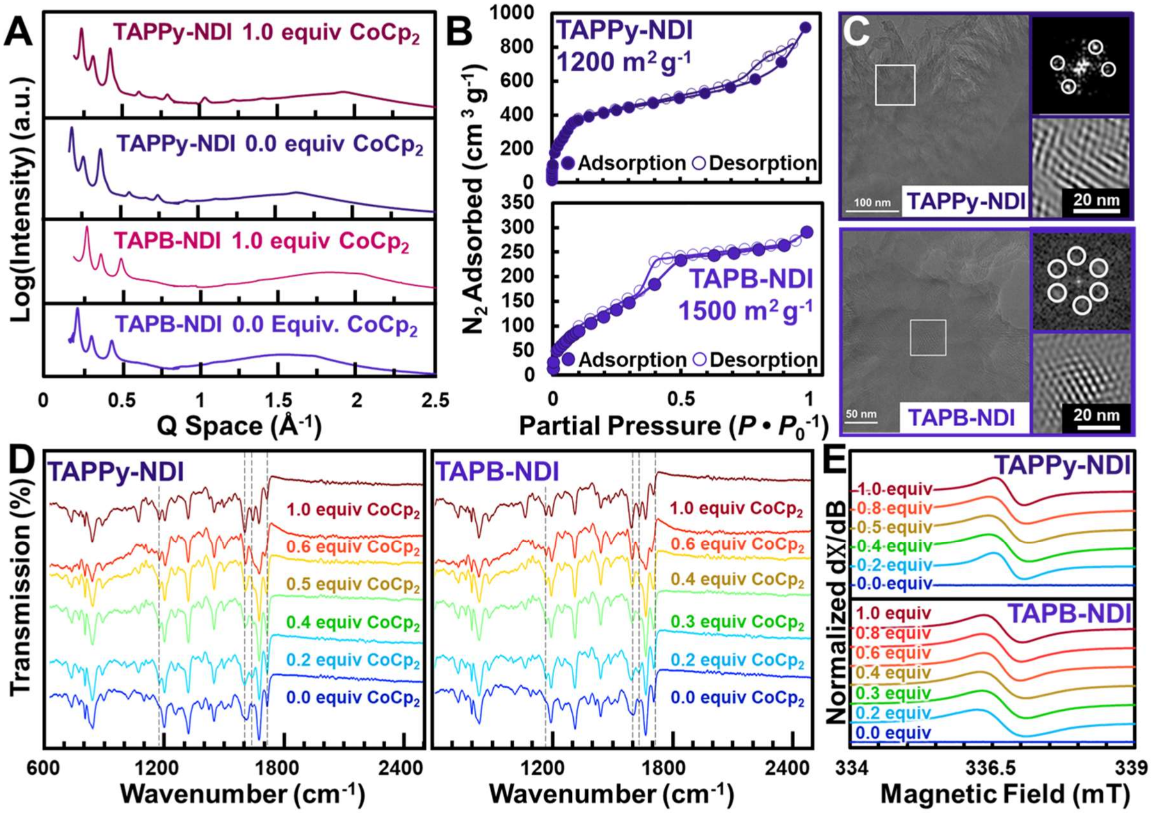

Figure 2. Chemical and structural characterization of undoped and *n*-doped 2DPs**. A)** Synchrotron X-ray diffraction of both as-synthesized undoped and fully doped (1 equiv $CoCp_2$ per NDI) NDI-based 2DPs. **B)** N_2 sorption isotherms for TAPPy-NDI (top) and TAPB-NDI (bottom). **C)** High-resolution transmission electron micrograph of TAPPy-NDI (top) and TAPB-NDI (bottom) with a Fourier-transform of a particular region (white box in Figure 2C, top right) and a band-pass filtered image of that region (bottom right).**D)** Fourier-transform infrared spectra of 2DPs variably doped with $CoCp_2$. **E)** Continuous-wave electron paramagnetic resonance spectra of pristine and variably doped NDI-based 2DPs.

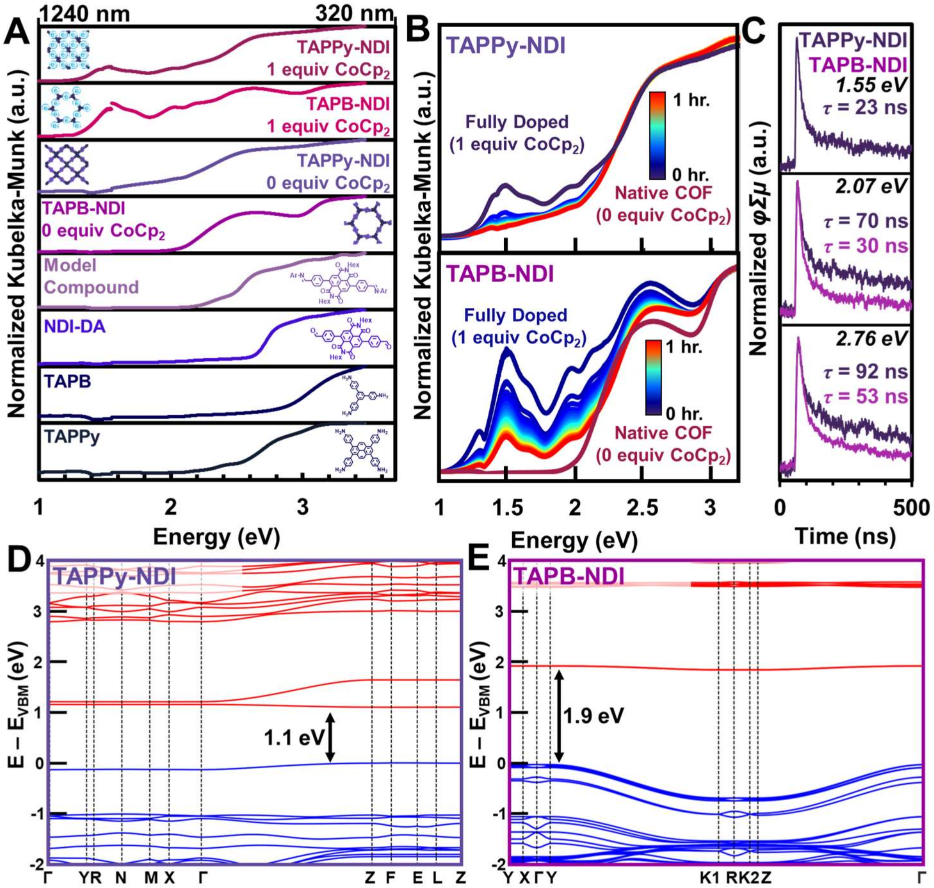

Figure 3. Optical characterization of monomers, model compounds, pristine 2DPs, and doped 2DPs and electronic structure of pristine 2DPs. **A)** Diffuse-reflectance ultraviolet-visible-near-IR spectroscopy of monomers, model compound, pristine NDI-containing 2DPs, and fully doped (1.0 equiv. $CoCp_2$ per NDI) NDI-containing 2DPs. The discontinuities in the spectra ~1.4 eV are due to a detector change-over within the instrument. **B)** Diffuse-reflectance ultraviolet-visible-near-IR spectroscopy during temporal evolution of fully doped NDI-containing 2DPs to entirely undoped upon exposure to air. **C)** Time-resolved flash-photolysis microwave conductivity of both pristine NDI-containing 2DPs and their charge-carrier lifetimes, inset text shows the excitation wavelength and the amplitude-weighted lifetime, <τ>. **D)** Electronic band structures calculated at the PBE0 density functional theory level for pristine multilayer TAPPy-NDI and E. TAPB-NDI (valence bands in blue; conduction bands in red).

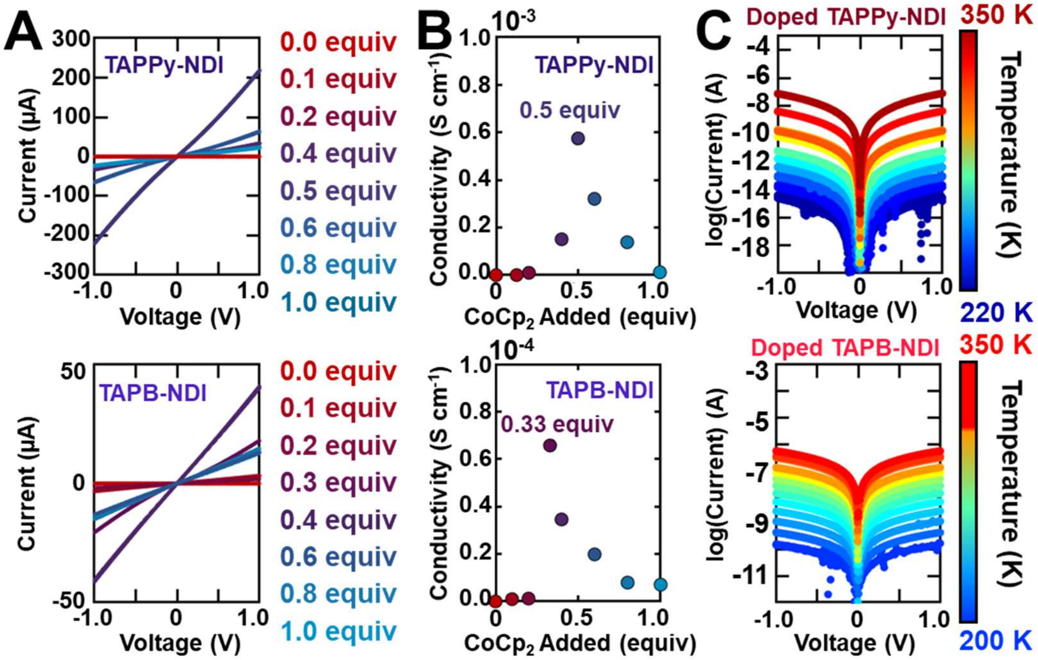

Figure 4. Conductivity measurements of controllably doped NDI-containing 2DPs. **A)** Current-voltage measurements of variably doped TAPPy-NDI (top) and TAPB-NDI (bottom) and **B)** extracted conductivities from **A**. **C)** Temperature-dependent conductivity of TAPPy-NDI (0.5 equiv $CoCp_2$, top) and of TAPB-NDI (1.0 equiv $CoCp_2$, bottom).

Table of Contents

TOC Text: The bulk conductivity of naphthalene diimide-based two-dimensional polymers is increased by controlled stoichiometric *n*-doping with cobaltocene. Following single-electron reduction, these 2DPs retain their periodic structure and become paramagnetic. Substoichiometric doping leads to the highest bulk electronic conductivities, which is found to proceed through a hopping-mechanism.

Keywords: Two-dimensional polymers, controlled *n*-doping, organic semiconductors

Primary Keyword: Two-dimensional polymer doping

Austin M. Evans, Kelsey A. Collins, Sangni Xun, Taylor G. Allen, Samik Jhulki, Ioannina Castano, Hannah L. Smith, Michael J. Strauss, Alexander K. Oanta, Lujia Liu, Lei Sun, Obadiah G. Reid, Gjergji Sini, Danilo Puggioni, James M. Rondinelli, Tijana Rajh, Nathan C. Gianneschi, Antoine Kahn, Danna E. Freedman, Hong Li, Stephen Barlow, Garry Rumbles, Jean-Luc Brédas, Seth R. Marder, William R. Dichtel*

Controlled *n*-Doping of Naphthalene Diimide-Based Two-Dimensional Polymers

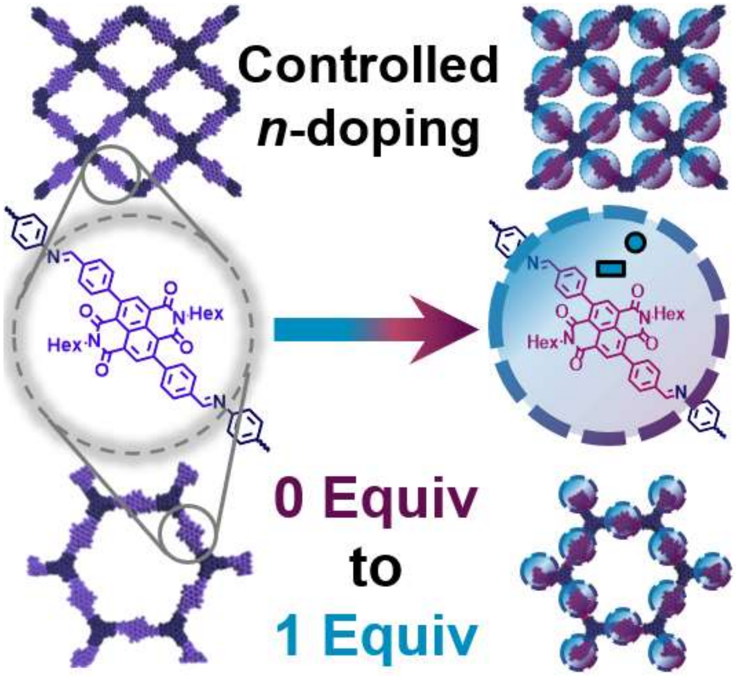

Supporting Information

Controlled *n*-Doping of Naphthalene Diimide-Based Two-Dimensional Polymers

*Austin M. Evans, Kelsey A. Collins, Sangni Xun, Taylor G. Allen, Samik Jhulki, Ioannina Castano, Hannah L. Smith, Michael J. Strauss, Alexander K. Oanta, Lujia Liu, Lei Sun, Obadiah G. Reid, Gjergji Sini, Danilo Puggioni, James M. Rondinelli, Tijana Rajh, Nathan C. Gianneschi, Antoine Kahn, Danna E. Freedman, Hong Li, Stephen Barlow, Garry Rumbles, Jean-Luc Brédas, Seth R. Marder, William R. Dichtel***

Correspondence Addresses

Professor William R. Dichtel
Department of Chemistry
Northwestern University
2145 Sheridan Road
Evanston, IL 60208, USA
wdichtel@northwestern.edu

Table of Contents

List of Figures in Supporting Information

A. Materials and Methods

Materials

All monomers, solvents, and catalysts were either purchased from commercial sources or prepared following literature reported protocols. All materials were used as received without further purification. Anhydrous THF was obtained from a solvent purification system (JC Myer System). Specifically, the following chemicals were obtained from the noted suppliers.

napthalene-1,4,5,8-tetracarboxylic acid: Sigma-Aldrich, Item No. N818
1,3-dibromo-5,5-dimethylhydantoin: Sigma-Aldrich, Item No. 157902
n-hexylamine: Sigma-Aldrich, Item No. 219703
4-formylbenzene(boronic acid): TCI America, Item No. F0446
tetrabromopyrene: TCI America, Item No. T2716
4-aminophenyl(boronic acid): Sigma Aldrich, Item No. 708887
cobaltocene: Sigma Aldrich, Item No. 339164

Instrumentation

Nuclear Magnetic Resonance. ^{1}H NMR spectra were acquired on a 400 MHz Agilent DD MR-400 system or Bruker Avance III 500 MHz spectrometer and recorded at 25 °C. All chemical shifts were calibrated using residual protic solvent as internal reference ($CDCl_3$: 7.26 ppm for ^{1}H NMR and 77.0 ppm for ^{13}C NMR. DMSO: 2.5 ppm for ^{1}H NMR and 35.9 for ^{13}C NMR).

Sonication. Sonication was performed with a Branson 3510 ultrasonic cleaner with a power output of 100W and a frequency of 42 kHz.

Supercritical CO_2 Drying. The supercritical drying procedure was performed in Tousimis Samdri795 critical point dryer. Prior to the supercritical drying process, all samples were placed in tea bags (ETS Drawstring Tea Filters, sold by English Tea Store, Amazon.com) and then soaked in absolute ethanol to keep the samples wet (typically 5-15 min). The drying chamber is first cooled ('cool' valve meter set to 0.40), and the tea bags containing the samples were then placed in it, and the chamber is filled with absolute ethanol and then sealed. The chamber was then filled with liquid CO2 ('fill' valve meter set to 0.40), and after 2 min, the samples were purged for 30 min ('purge-vent' valve meter set to 0.15, and 'purge timer' valve meter set to 6). The temperature was then raised to 40 °C resulting in a chamber pressure of around 1300 psi, which is well above the critical point of CO_2. The chamber was held above the critical point for 30 min, after which the CO_2 source was turned off, and the pressure was released over a period of 30 min ('bleed' valve meter set at 0.07). The samples were then transferred to vials and their final mass were weighed.

Nitrogen Porosimetry. N_2 sorption isotherms were collected on a Micromeritics ASAP 2420 Accelerated Surface Area and Porosity Analyzer. Typically, 20-50 mg samples were transferred to dried and tared analysis tubes equipped with filler rods and capped with a Transeal. The samples were heated to 40 °C at a rate of 1 °C min^{-1} and evacuated at 40 °C for 20 min, then heated to 100

°C at a rate of 1 °C min^{-1} heat, and evacuated at 100 °C until the outgas rate was ≤0.3 µmHg min^{-1} (holding the samples at 100 °C for 5 hr was found to be sufficient), at which point the tube was weighed again to determine the mass of the activated sample. The tube was then transferred to the analysis port of the instrument. UHP-grade (99.999% purity) N_2 was used for all adsorption measurements. N_2 isotherms were generated by incremental exposure to nitrogen up to 760 mmHg (1 atm) in a liquid nitrogen (77 K) bath. Oil-free vacuum pumps and oil-free pressure regulators were used for all measurements. Brunauer-Emmett-Teller (BET) surface areas were calculated from the linear region of the N_2 isotherm at 77 K within the pressure range $P\ P_0^{-1}$ shown in BET plots below.

Ambient Atmosphere Fourier-transform Infrared Spectroscopy. Infrared spectra were recorded on a Nicolet iS10 FT-IR spectrometer equipped with a ZnSe ATR attachment. All spectra are recorded with a resolution of 4 cm^{-1}. All spectra are background subtracted and shown normalized to the same feature.

Inert Atmosphere Fourier-transform Infrared Spectroscopy. Infrared spectra were recorded on a Bruker Alpha FTIR spectrometer equipped with an attenuated total reflectance accessory and diamond anvil with a resolution of 4cm^{-1}. All spectra are background subtracted and shown normalized to the same feature.

Continuous Wave Electron Paramagnetic Resonance Spectroscopy. Continuous wave electron paramagnetic resonance (CW-EPR) spectra were acquired using a Bruker ELEXYS E500 spectrometer operating at X-band (9.4 GHz) frequencies with an Oxford ESR900 He flow cryostat with an ITC-5025 temperature controller and a Bruker High QE (HQE) cavity resonator (ER 4122SHQE). *g* tensors were calibrated for accuracy using known BDPA and Mn^{2+} in SrO standards. The acquisition parameters such as the receiver gain, modulation amplitude, and microwave power were all optimized and then kept constant to enable comparison of multiple samples under the same conditions. The modulation amplitude was set to 0.05G and the microwave power was 0.01mW. The samples were sealed under He and the EPR spectra were recorded at 5.0 K. The EPR signals exhibited linear dependence vs square root of power up to 2mW power. All spectra are simulated using EasySpin software package Release 6.0.0-dev.26 (2020-10-12).[1] The spectra were simulated by the EasySpin solid state function pepper using spin system ½, isotropic g tensor, frequency used in each experiment, and linewidth (peak to peak) with Lorentzian/ Gaussian lineshape. Quantitative analysis of TAPPy-NDI and TAPB-NDI samples obtained using *X-EPR Quantitative Analysis, SpinCount Module*.

Diffuse Reflectance Ultraviolet-Visible Spectroscopy. Diffuse-reflectance ultraviolet-visible spectra were taken with a Varian Cary 5000 spectrophotometer using a Praying Mantis diffuse reflectance attachment. In all cases, samples were manually aligned to yield appropriate signal at low wavelengths. When samples were taken under inert atmosphere, a self-contained sample holder was loaded under inert atmosphere.

Flash-Photolysis Time-resolved Microwave Conductivity (fp-TRMC). Our fp-TRMC measurement system and methods has been described in detail elsewhere.[2, 3] Photoexcitation was performed using a Nd:YAG (Spectraphysics Quanta Ray SP Pro 230-30H) laser (355 nm) with a laser power of 9 W at 30 Hz to pump an optical parametric oscillator (Spectraphysics GWU PremiScan ULD/500) with variable output over the range of 410 – 2500 nm with *ca.* 5 ns pulses. Samples were purged continuously with N_2 during these measurements. Clean quartz substrates were used to evaluate the lower limit of measurable microwave signal and thus yield-mobility products. For more information on sample preparation and measurement details, we direct readers to a more thorough description Section I.

Fabrication of 2PD: and monomer:polystyrene films for fp-TRMC. Due to the insolubility of 2PD compounds, 2PD powder was dispersed in an electrochemically inert polystyrene matrix to facilitate the formation of somewhat uniform films with ~25 mm x 10 mm dimensions suitable for TRMC. 4.20 and 4.54 mg of TAPB-NDI and TAPPy-NDI, respectively, were mixed with 0.5 mL of a 40 mg/mL polystyrene (Sigma-Aldrich, product # 182427, Mw ~ 280 kDa) solution in chloroform (Sigma-Aldrich, product # C2432-500mL). The 2DP:polystyrene solutions were sonicated for ~60 seconds to break up large particulates and then stirred for 30 min at room temperature. Once thoroughly mixed, 150 µL of the 2DP:polystyrene solutions were drop casted onto clean quartz substrates. NDIDA monomer (**Figure S1**):polystyrene control films were made similarly (1.80 mg NDI monomer used). All solution and film preparation done inside a nitrogen glovebox (< 1 ppm O_2). Quartz slides were cleaned by three, 15 min sonication steps in acetone, blowing dry with nitrogen after each sonication step, and then UV-ozone for 15 min.

Integrating Sphere Absorption Spectroscopy to Quantify Fraction of Absorbed Photons. Absorptance spectra for 2DP: and monomer:polystyrene films were acquired using an integrating sphere system to quantify the fraction of absorbed photons (FA) with minimal deleterious scattering contributions to the measured signal that is typically more significant normal transmission/reflection measurements. This system consisted of an Ocean Optics halogen lamp (DH-2000) fiber-coupled to an integrating sphere (LabSphere model) whose output is relayed via optical fiber to the liquid nitrogen cooled Si and InGaAs CCDs of a Princeton photoluminescence spectrometer (SpectraPro HRS-300). Spectra were acquired with a 150 line/mm grating with 800 nm blaze, 250 micron slit width, 300 ms exposure (1 s for NIR), while averaging 20 scans per spectrum. For scans over 400-800 nm, a 390 nm long pass filter was used to avoid secondary diffraction signal at ca. 800 nm. Similarly, a 500 nm long pass filter was used for spectra collected in the 500-1000 nm range. Backgrounds were taken with a clean quartz slide to remove substrate contributions. Absorption spectra acquired for TAPPy-NDI: and TAPB-NDI:polystyrene films in this manner were consistent with the diffuse reflectance UV-vis described in the main text.

Electrochemistry. Electrochemistry experiments were conducted on a Princeton Applied Research VersaSTAT 3 potentiostat. All experiments were conducted using a standard three electrode cell configuration using a fritted three compartment cell with a modified glassy carbon as the working electrode, a 27-gauge Pt wire coiled as the counter electrode, and an Ag/AgCl reference electrode in CH_3CN. Potentials were referenced to the ferrocenium/ferrocene couple.

Synchrotron X-ray Diffraction. Synchrotron powder X-ray diffraction was collected at either Sector 5 or 12 of the Advanced Photon Source, Argonne National Lab. Experiments were collected at either 17 keV or 13.3 keV. In all cases, the number of frames and exposure times was optimized for signal-to-noise. All frames were then summed and radially integrated to produce a linear PXRD pattern using proprietary software available at the APS. All experiments were conducted using a transmission geometry with samples placed in 2.0 mm OD borosilicate capillaries with 0.2 mm wall thicknesses purchased from Hilgenberg GmbH. When doped samples were measured, the samples were sealed within these capillaries under a nitrogen atmosphere. The sample-to-detector distance was adjusted to measure across relevant detection ranges of q. Scattering intensity is reported as a function of the modulus of the scattering vector Q, related to the scattering angle 2θ by the equation Q = (4π/λ) sin θ, where λ is the x-ray wavelength (**Equation 1**).

$$Q = \frac{4\pi}{\lambda}\sin(\theta) \qquad \text{(Equation 1)}$$

Simulated X-ray Diffraction. Simulations of 2DP X-ray scattering profiles were carried out in MaterialsStudio (ver.5.0). First, the unit cell was constructed piecewise in a primitive P6 unit cell with the *a*=*b* lattice parameter set to be approximately the distance between two 2DP vertices based on approximate molecular bond lengths. The *c* parameter was set to be 3.5 Å, which is the interlayer spacing of graphene. We then used a Forcite geometry optimization routine with a universal forcefield to optimize the unit cell size with convergence tolerances of Energy = 10^{-3} kcal mol^{-1} and Force = 0.5 kcal mol^{-1} Å^{-1}.

Diffraction simulation and Pawley refinement were carried out using the Reflex software package. 2DP models and their simulated patterns were Pawley refined to experimental patterns iteratively until the RWP value converges. The pseudo-Voigt profile function was used for whole profile fitting. The final RWP and RP values were calculated to be less than 5% in all cases. Simulated XRD patterns were calculated from the refined unit cell and compared with the experimentally observed patterns.

Ultraviolet and Inverse Photoelectron Spectroscopy. UPS and IPES measurements were performed in an ultrahigh vacuum chamber with a base pressure of 5 x 10^{-10} Torr. For UPS, the He I photon line (21.22 eV) from a discharge lamp was used to excite electrons from the occupied states. The unoccupied states were measured by IPES in isochromat mode. The resolutions for UPS and IPES are 0.15 eV and 0.45 eV, respectively.

Connolly Surface Area Calculation. After a refined structure was simulated via diffraction modeling as described above, we went on to calculate the theoretical surface area for our structures. This was done using a Connolly method (sometimes known as a solvent-excluded surface method or molecular surface method). This method can be described as rolling a ball along a molecular surface to assess its accessible surface. We performed this calculation using the Crystal Surfaces and Volumes module of MaterialsStudio using the parameters for molecular nitrogen as the adsorbate. This yielded a surface area per unit cell, which could then be converted to the surface area per gram value which is reported in the manuscript.

Transmission Electron Microscopy. All samples were prepared by placing a lacey carbon copper TEM grid in a vial containing a few milligrams of the COF powder and then tapping/shaking off the excess powder. TEM was performed using a JEOL (JEOL USA, Inc., Peabody, MA) ARM200CF Aberration-Corrected STEM/TEM operated at 200 keV equipped with a Gatan (Gatan, Inc., Pleasanton, CA) K2 "direct electron" detector (FEG Emission: 15 µA, spot size 5, 150 µm CL aperture). The ARM200CF was aligned for low-dose imaging, measuring the dose rate on the K2 detector through vacuum (no grid inserted). The dose rate was measured to be 6.8 e^{-} $Å^{-2}$ s^{-1} (3710 x 3838 pixels) for TAPPy-NDI and 10.9 e^{-} $Å^{-2}$ s^{-1} (3710 x 3838 pixels) for TAPB-NDI with image exposure times of 0.98 s (6.7 and 10.7 e^{-} $Å^{-2}$ cumulative dose per image, respectively). All image acquisition was done using the Gatan Microscopy Suite (GMS), Digital Micrograph (Gatan, Inc., Pleasanton, CA). All samples were prepared by placing a lacey carbon copper TEM grid in a vial containing ~1-10 mg of 2DP powder and then tapping/shaking off excess powder.

Variable-Doping Pressed Pellet Electronic Conductivity. Doping protocols are explained extensively in Section D. Briefly, polycrystalline 2DP powders were exposed to variable stoichiometric amounts of $CoCp_2$ in a THF solution for a minimum of 16 h. These powders were then isolated by filtration. Then, we loaded these powders into a hollowed glass rod. The powders were finger tightened between the rods and the two copper bars were then equipped to a potentiostat. We ran several potential sweeps in both bias directions to check for hysteretic behavior. In all cases, we observed no hysteresis, which led us to consider these materials as idealized Ohmic resistors. At the end of the experiment, we measured the length of the pressed pellet using dial calipers by measuring the difference of the full assembly with and without the powders. This distance, with the obtained IV curves, was used to evaluate the Ohmic resistance.

Variable-Temperature Pressed Pellet Electronic Conductivity. Variable-temperature conductivity measurements were obtained by loading powder samples pressed between two copper electrodes into a cryostat. Starting at high temperatures we monitored the I-V response of these pressed pellets. Then, we repeated this behavior as we iteratively dropped the sample temperature. In all cases, we waited for the temperature to stabilize.

B. Molecular Syntheses

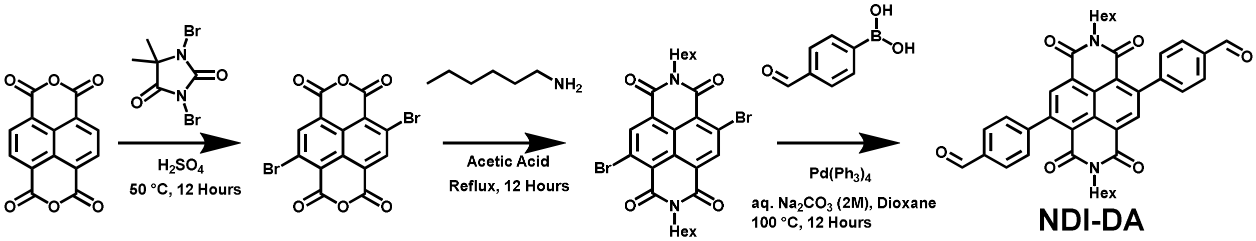

Figure S1. Synthesis of NDI-DA.

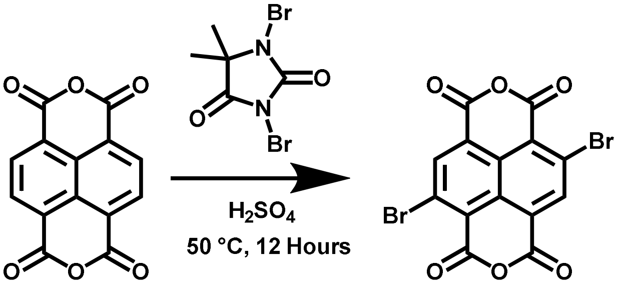

Figure S2. Synthesis of 3,7-dibromonapthalenedianhydride

This synthesis was adapted from a previous report.[4]

In single-necked round bottom flask (500 mL), NDA (10 g, 37.3 mmol, 1.0 equiv.) was slurried in concentrated sulfuric acid (150 mL) at ambient temperature. This mixture was stirred at room temperature for 5 min to obtain a solution. 1,3-Dibromo-5,5-dimethylhydantoin (15 g, 52.6 mmol, 1.4 equiv.) was added in four portions over a period of 1 h at room temperature. The resulting brown solution was then stirred at 50 °C for 10 hr. The mixture was then poured into crushed ice (250 g), which resulted in a precipitated solid. The precipitated solid was filtered, washed with water (200 mL) then with methanol (200 mL), and finally dried under vacuum to afford crude product, which was further purified by crystallization from DMF. During crystallization, the ring-opened carboxylic acid containing side products preferentially crystallized, leaving the supernatant with pure 3,7-dibromonapthalenediimide, which was isolation through precipitation by addition of methanol. The product was then obtained as a yellow solid by filtration and dried under vacuum (11.05 g, 69% yield). Characterization of this molecule was consistent with a previous report.[4]

^{1}H NMR (400 MHz, DMSO-d_6): H=8.78 ppm (s, 2H)

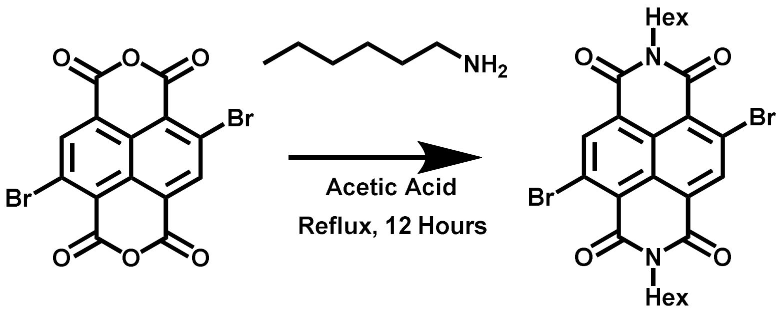

Figure S3. Synthesis of *N*-hexyl 3,7-di(bromo)napthalenediimide

This synthesis was adapted from a previous report.[4]

3,7-dibromonapthalene-1,8,4,5-tetracarboxylic (5 g, 11.7 mmol, 1.0 equiv.) was added to a flame-dried 500 mL round bottom flask filled with glacial acetic acid (350 mL) and *n*-hexylamine (5.9 g, 7.7 mL, 58.5 mmol, 5 equiv.). This reaction mixture was refluxed for 30 min under a constant stream of dry N_2, allowed to cool for 16 hr, and then was poured into methanol (500 mL). The precipitate of this reaction was collected by filtration, washed extensively with methanol, and dried under vacuum. The product was then isolated from this crude solid by dissolving the product in $CHCl_3$, stirring this mixture, and then adding methanol dropwise to this mixture until the desired product begins to precipitate. This yellow solid was then collected by filtration and identified as pure *N*-hexyl 3,7-di(bromo)napthalenediimide (9.6 g, 82% yield). Characterization of this molecule was consistent with a previous report.[4]

^{1}H NMR (400 MHz, $CDCl_3$): δ 8.98 (s, 2H), 4.17 (t, J = 7.8 Hz, 4H), 1.72 (quint., J = 7.8 Hz, 4H), 1.49-1.20 (m, 12H), 0.88 (t, J = 7.1 Hz, 6H).

^{13}C{^{1}H} NMR (100 MHz, $CDCl_3$) δ 160.73, 139.06, 128.96, 128.32, 127.72, 125.34, 124.08, 41.61, 31.45, 27.84, 26.73, 22.54, 14.02.

*Note: We observed that small amounts of water led to partial ring opening of our anhydride under these reaction conditions. Removing this side-product was found to be challenging and required separation by column chromatography (silica, 3:2 dichloromethane/hexanes). Drying procedures (flame drying glassware and operating under a dry N_2 stream) were found to limit the formation of this side-product substantially.

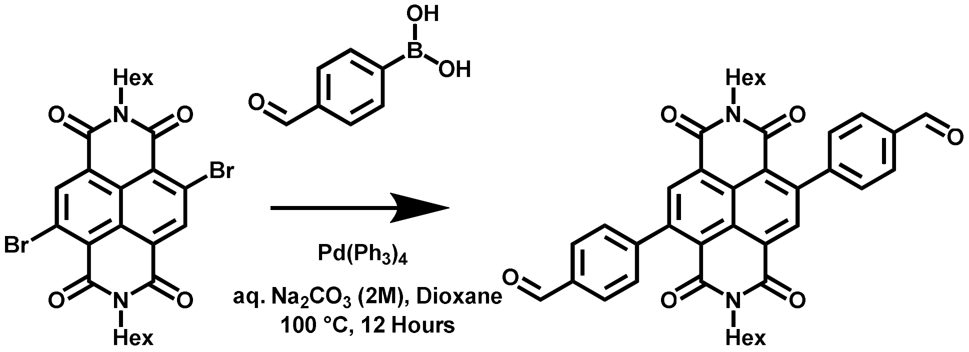

Figure S4. Synthesis of *N*-hexyl 3,7-di(formylbenzene)napthalenediimide

This synthesis was adapted from a previous report.[4] *N,N'*-dihexyl-3,7-di(bromo)naphthalene-1,8,4,5-tetracarboxylic diimide (4g, 7.75 mmol) was combined with 1-formyl, 4-boronic acid benzene (3g, 20.2 mmol) in 100 mL of dioxane and 33 mL of H_2O and 7g Na_2CO_3. This mixture was degassed for 30 min and 150 mg PdPh34 was then refluxed for three days. The solvent was removed, the solid collected, and was then subjected to a column (50%-0% Hexanes, 50%-100% DCM) and flushed with DCM until the second band came off the column (orange). The third band was collected by flushing with MeOH. Characterization of this molecule was consistent with a previous report.[4]

^{1}H NMR ($CDCl_3$, 400 MHz): δ (ppm) = 10.14 (s, 2H), 8.64 (s, 2H), 8.05 (d, *J* = 8.4 Hz, 4H), 7.56 (d, *J* = 8.0 Hz, 4H), 4.04-4.08 (m, 4H), 1.60-1.65 (m, 4H), 1.25-1.35 (m, 12H), 0.84-0.92 (m, 6H).

^{13}C{^{1}H} NMR ($CDCl_3$, 100 MHz): δ (ppm) = 191.7, 162.1, 162.0, 146.6, 146.4, 135.9, 135.0, 129.8, 128.7, 127.3, 125.9, 123.1, 41.1, 31.4, 27.9, 26.6, 22.5, 14.0

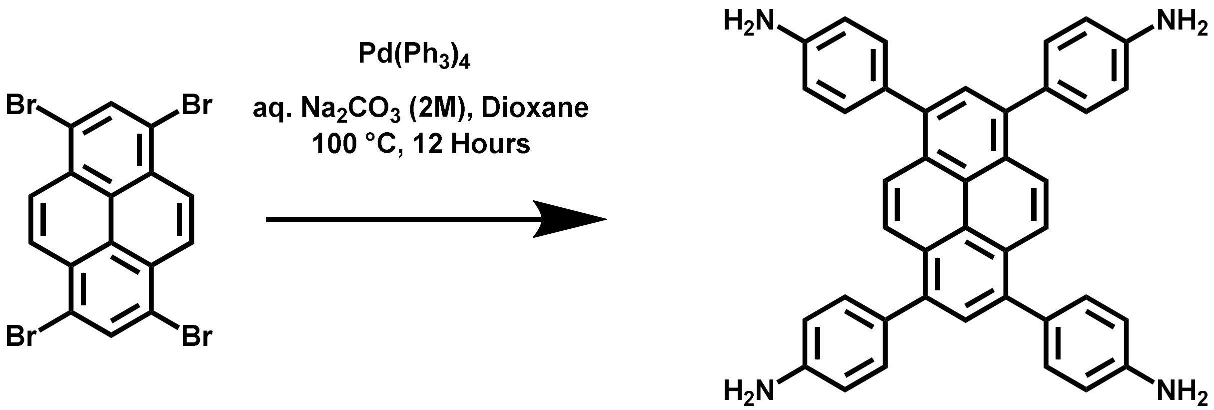

Figure S5. Synthesis of 1,3,6,8-tetra(aminophenyl)pyrene.

This synthesis was adapted from a previous report.[5]

A solution of 1,3,6,8-tetrabromopyrene (7.4 g, 14.3 mmol, 1.0 eq.), 4-aminophenylboronic acid pinacol ester (15 g, 68.5 mmol, 4.8 eq.), K_2CO_3 (10.9 g, 15.7 mmol, 5.5 eq.) and $Pd(PPh_3)_4$ (1.65 g, 1.45 mmol, 10 mol%) in 32 mL 1,4-dioxane and 8 mL H2O was heated to reflux (115 °C) for 3 days. After cooling to room temperature, H2O was added. The resulting precipitate was collected via filtration and was washed with H2O and MeOH. Recrystallization from 1,4-dioxane, followed by drying under high vacuum furnished the title compound, co-crystallized with approximately 1.5 dioxane molecules per formula unit, as a bright yellow powder (7.2 mg, 10.2 mmol, 72%). Characterization was consistent with a previous report.[5]

^{1}H NMR (400 MHz, DMSO-d6): 8.13 (s, 4 H), 7.79 (s, 2 H), 7.34 (d, *J* = 8.4 Hz, 8 H), 6.77 (d, *J* = 8.5 Hz, 8 H), 5.30 (s, 8 H), 3.56 (s, 12 H, dioxane).

^{13}C{^{1}H} NMR (100 MHz, DMSO-d6): 148.2, 137.1, 131.0, 129.0, 127.6, 126.7, 126.1, 124.4, 113.9, 66.3 (dioxane).

C. Two-Dimensional Polymerization

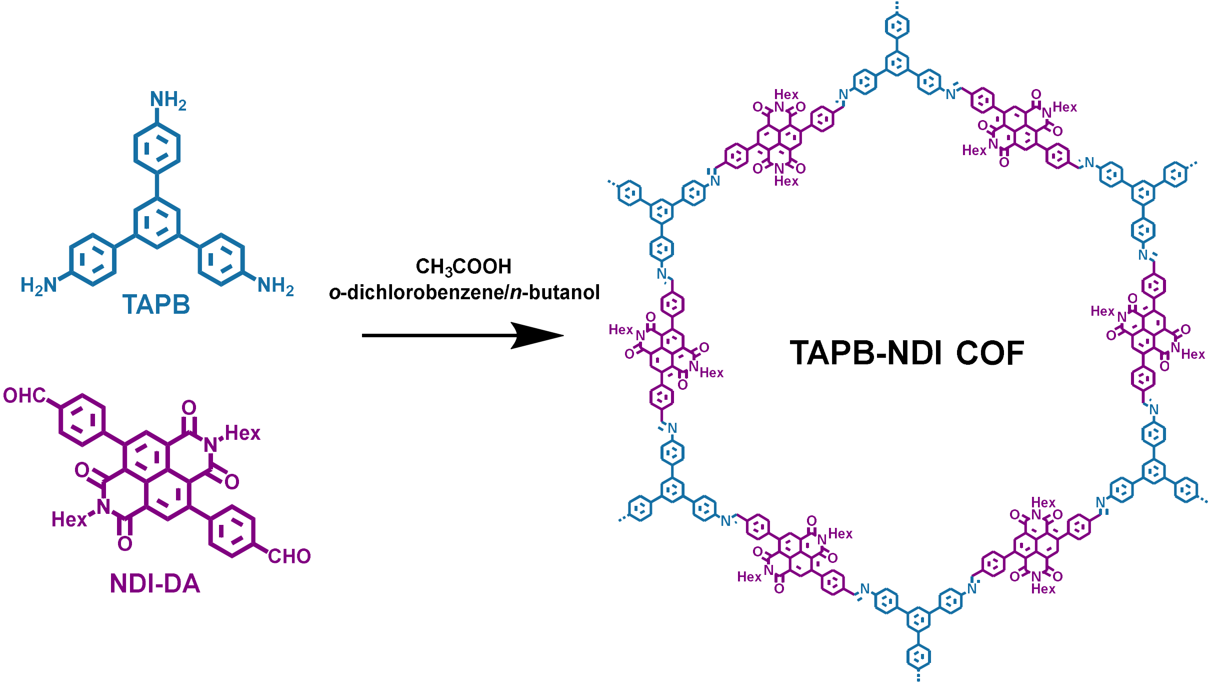

Figure S6. Synthesis of TAPB-NDI

TAPB-NDI powders were synthesized under solvothermal conditions. To produce these materials, 1,3,5-tris(4-aminophenyl)benzene (TAPB, 35 mg, 5 mM, 1 equiv.) and NDI-DA (100 mg, 7.5 mM, 1.5 equiv.) were dissolved in a mixture of 1:1 *o*-dichlorobenzene:*n*-butanol (20 mL) by sonicating for 10 min. Then, a 9M CH_3COOH (acetic acid, 10 vol%) was added to the mixture. At this point, the mixture was sealed and heated to 90°C in a scintillation vial on an aluminum pie block. These samples were allowed to heat for 3 d, at which point they were filtered and rinsed extensively with MeOH (100 mL). Finally, these samples were subjected to $scCO_2$ drying.

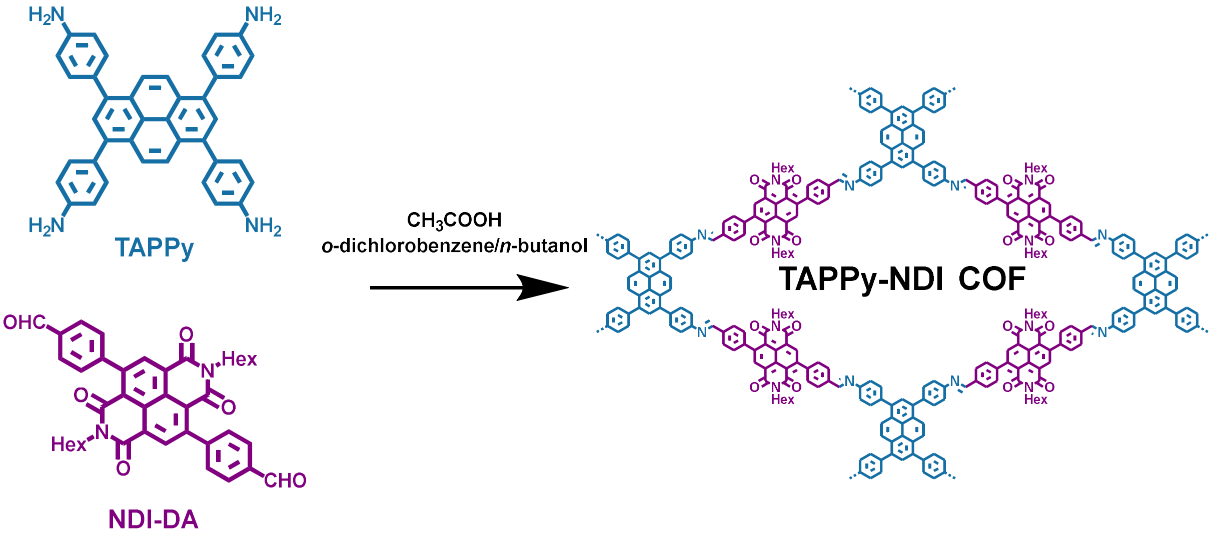

Figure S7. Synthesis of TAPPy-NDI

TAPPy-NDI powders were synthesized under solvothermal conditions. To produce these materials, 1,3,6,8-tetra(4-aminophenyl)pyrene (TAPPy, 57 mg, 5 mmol, 1 equiv.) and NDI-DA (134 mg. 7.5 mM, 1.5 equiv.) were dissolved in a mixture of 1:1 *o*-dichlorobenzene:*n*-butanol by sonicating for 10 min. Then, a 9M CH_3COOH (acetic acid, 10 vol%) was added to the mixture. At this point, the mixture was sealed and heated to 90°C in a scintillation vial on an aluminum pie block. These samples were allowed to heat for 3 d, at which point they were filtered and rinsed extensively with MeOH (100 mL). Finally, these samples were subjected to $scCO_2$ drying.

D. Fourier-Transform Infrared Spectroscopy

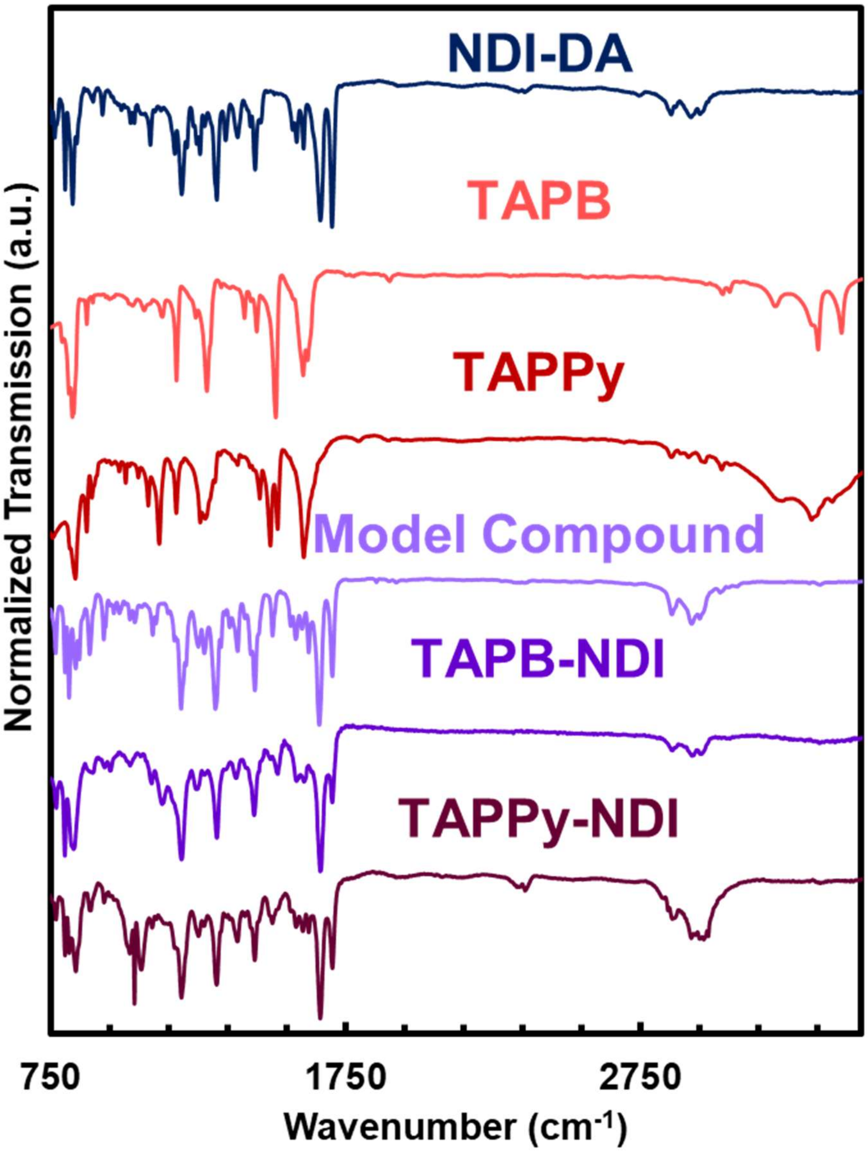

Figure S8. Comparison of FT-IR spectra of monomers, an imine model compound, and the two undoped 2DPs.

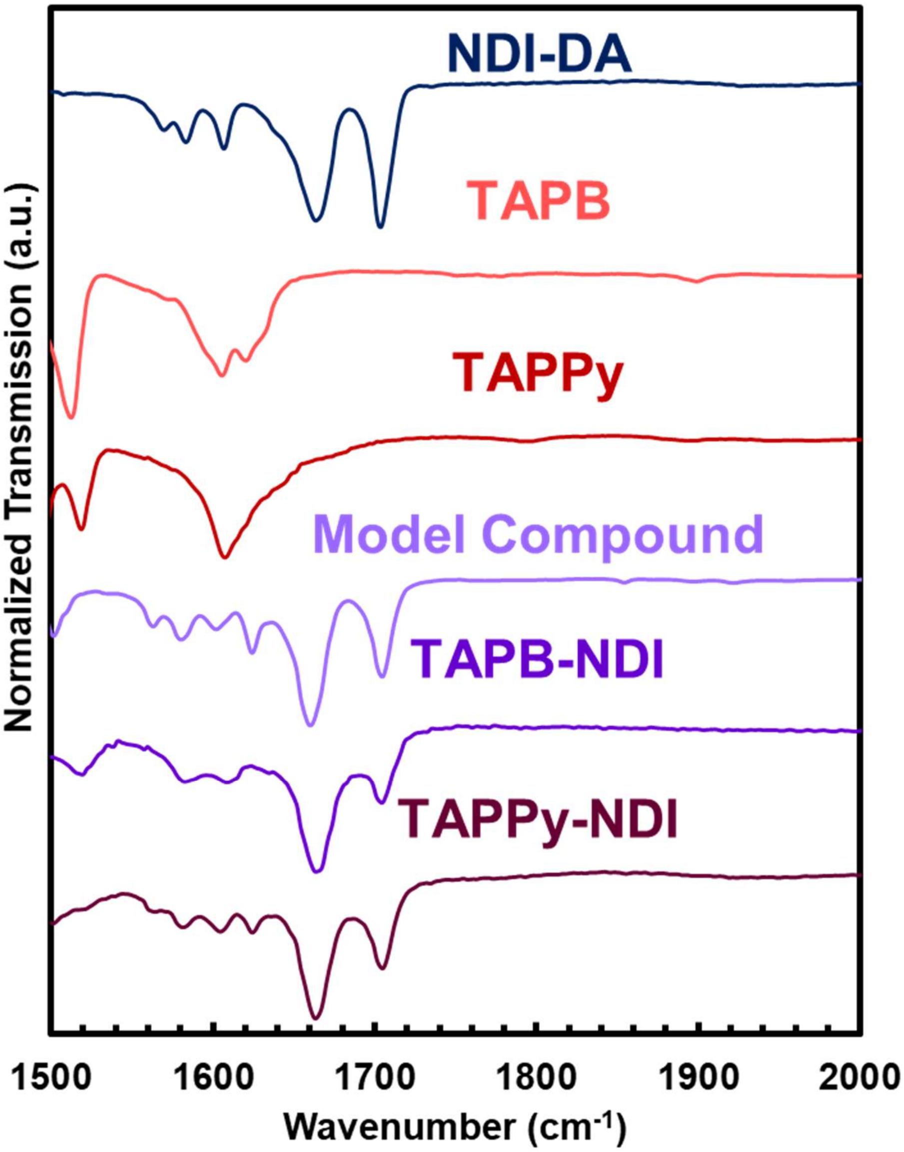

Figure S9. Comparison of FT-IR spectra of monomers, an imine model compound, and the two undoped 2DPs over a more limited frequency range.

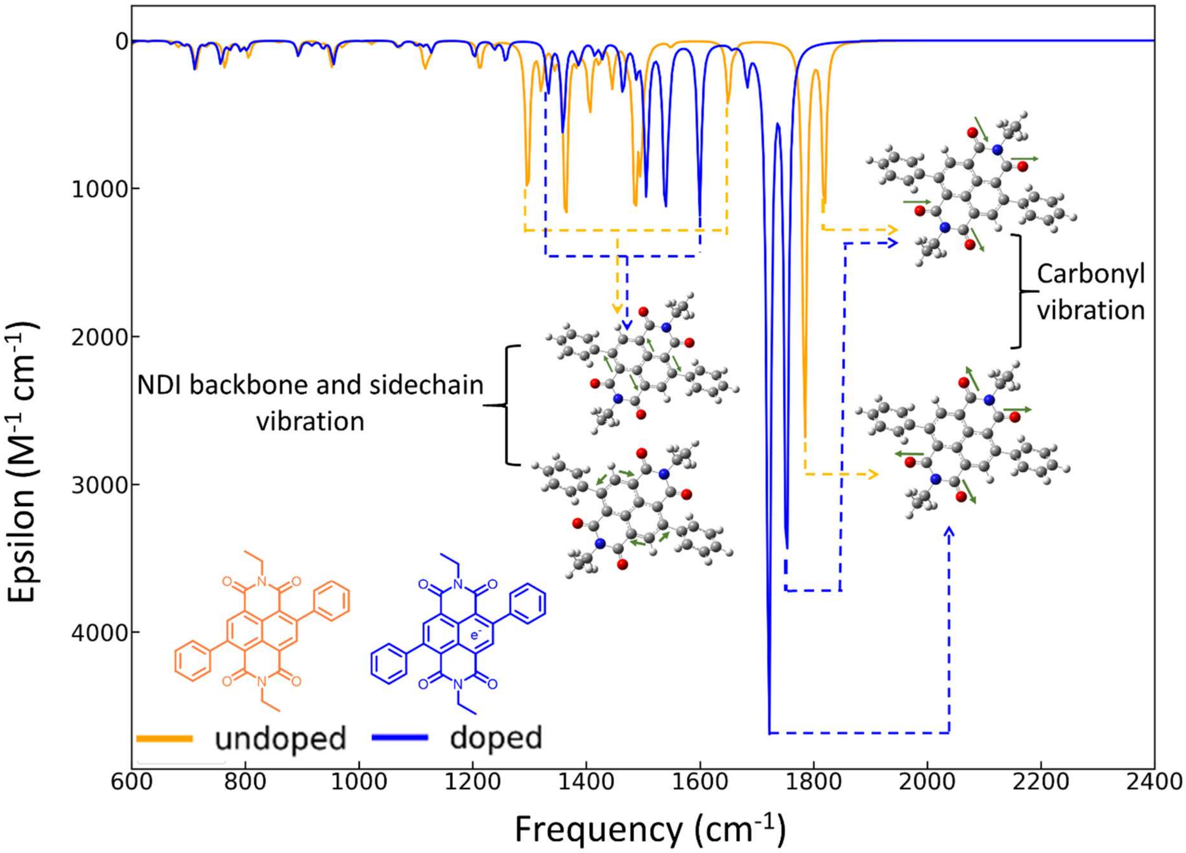

Figure S10. Simulated infrared spectra of neutral and radical-anion NDI.

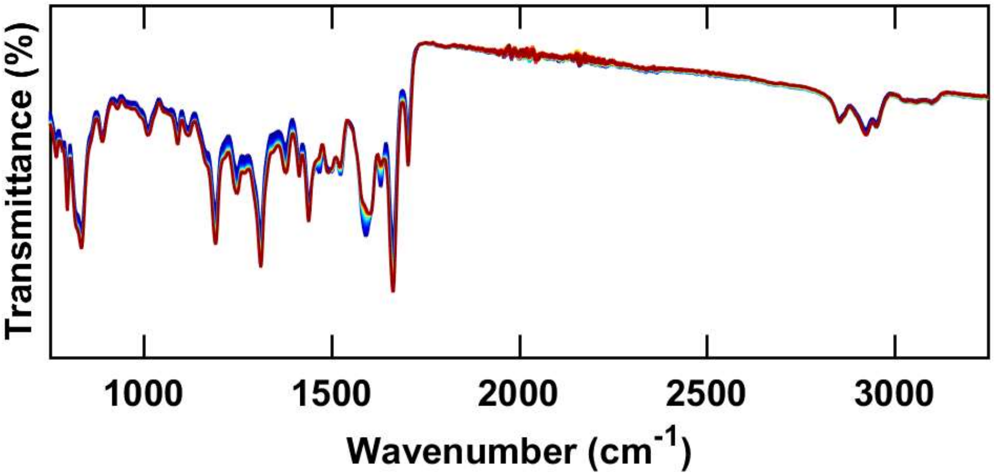

Figure S11. FT-IR spectra during temporal evolution of fully doped TAPPy-NDI upon exposure to air over the course of one hour. Isosbestic points are suggestive of a complete transformation from one species to another.

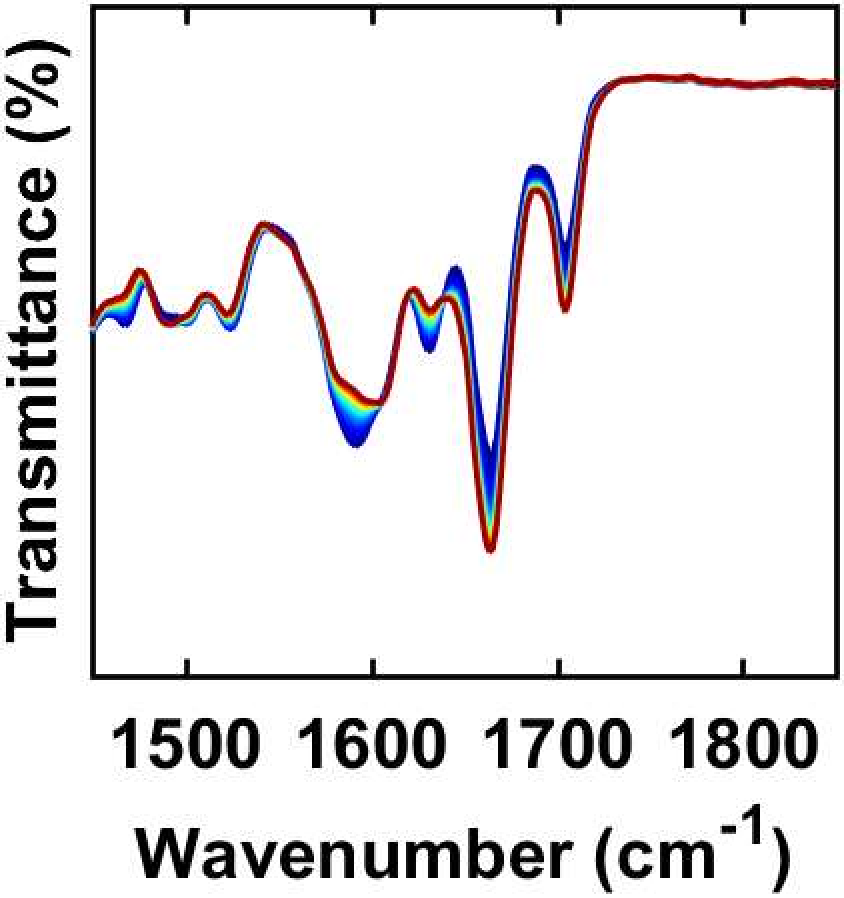

Figure S12. FT-IR spectra over a limited frequency range during temporal evolution of fully doped TAPPy-NDI upon exposure to air over the course of one hour. Isosbestic points are suggestive of a complete transformation from one species to another.

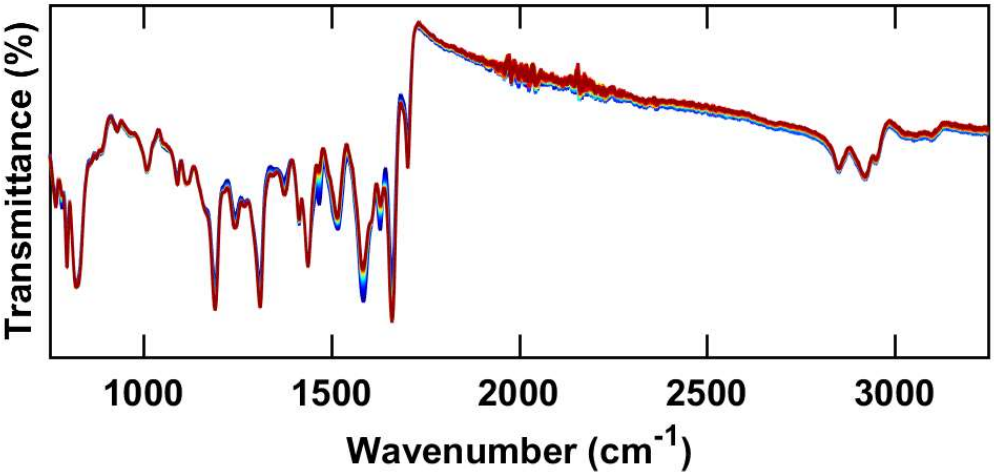

Figure S13. FT-IR spectra during temporal evolution of fully doped TAPB-NDI upon exposure to air over the course of one hour. Isosbestic points are suggestive of a complete transformation from one species to another.

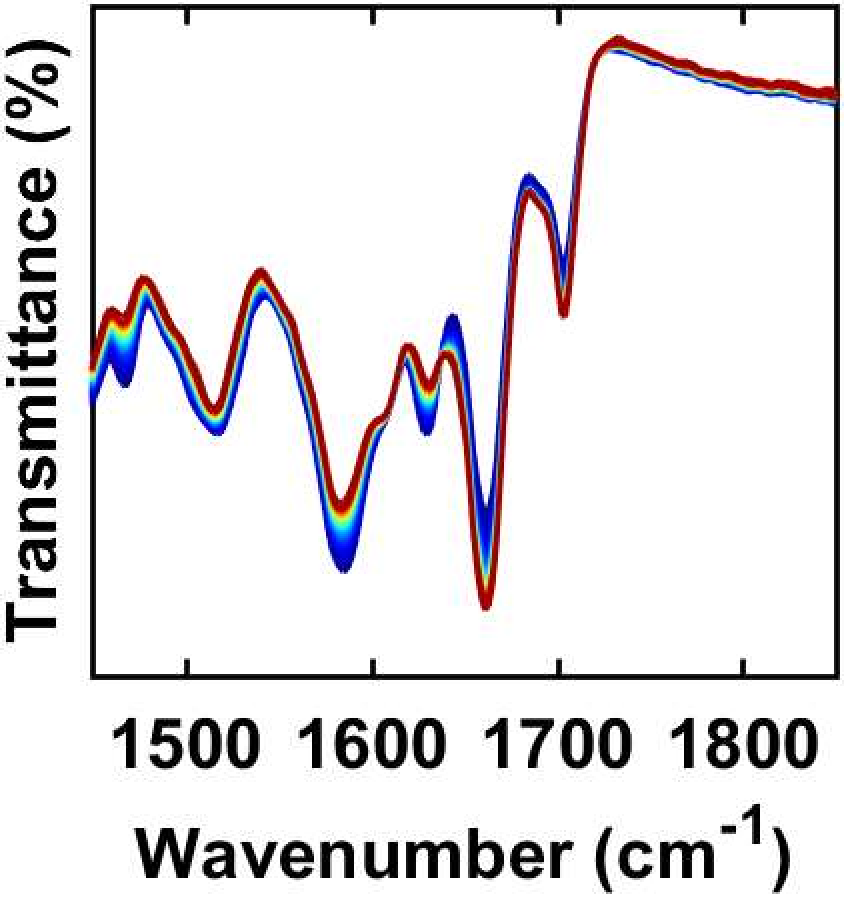

Figure S14. FT-IR spectra over a limited frequency range during temporal evolution of fully doped TAPB-NDI upon exposure to air over the course of one hour. Isosbestic points are suggestive of a complete transformation from one species to another.

E. Transmission Electron Microscopy

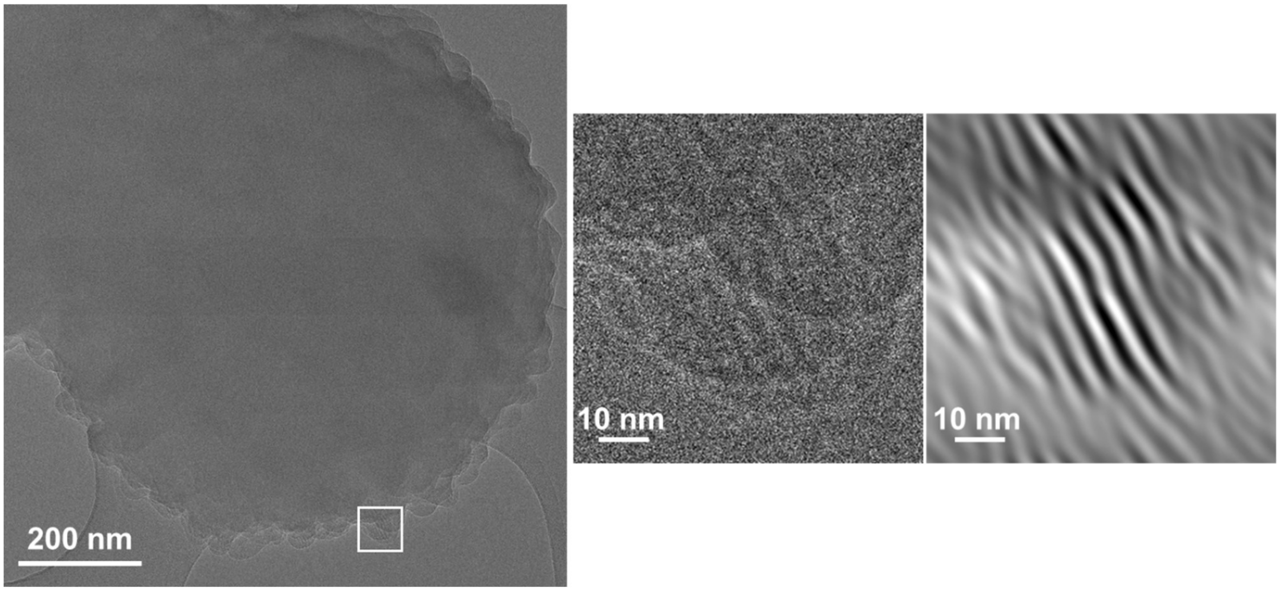

Figure S15. Transmission electron micrographs with a large-field-of-view (left), zoomed in (middle), and band-pass filtered (right) of TAPB-NDI.

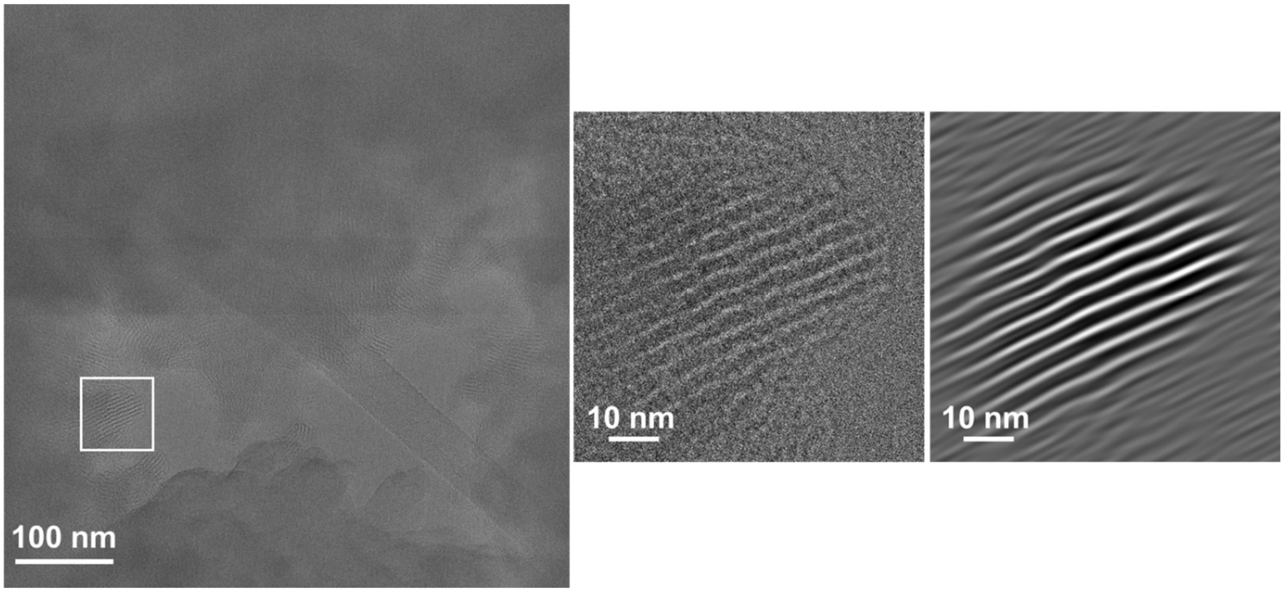

Figure S16. Transmission electron micrographs with a large-field-of-view (left), zoomed in (middle), and band-pass filtered (right) of TAPB-NDI.

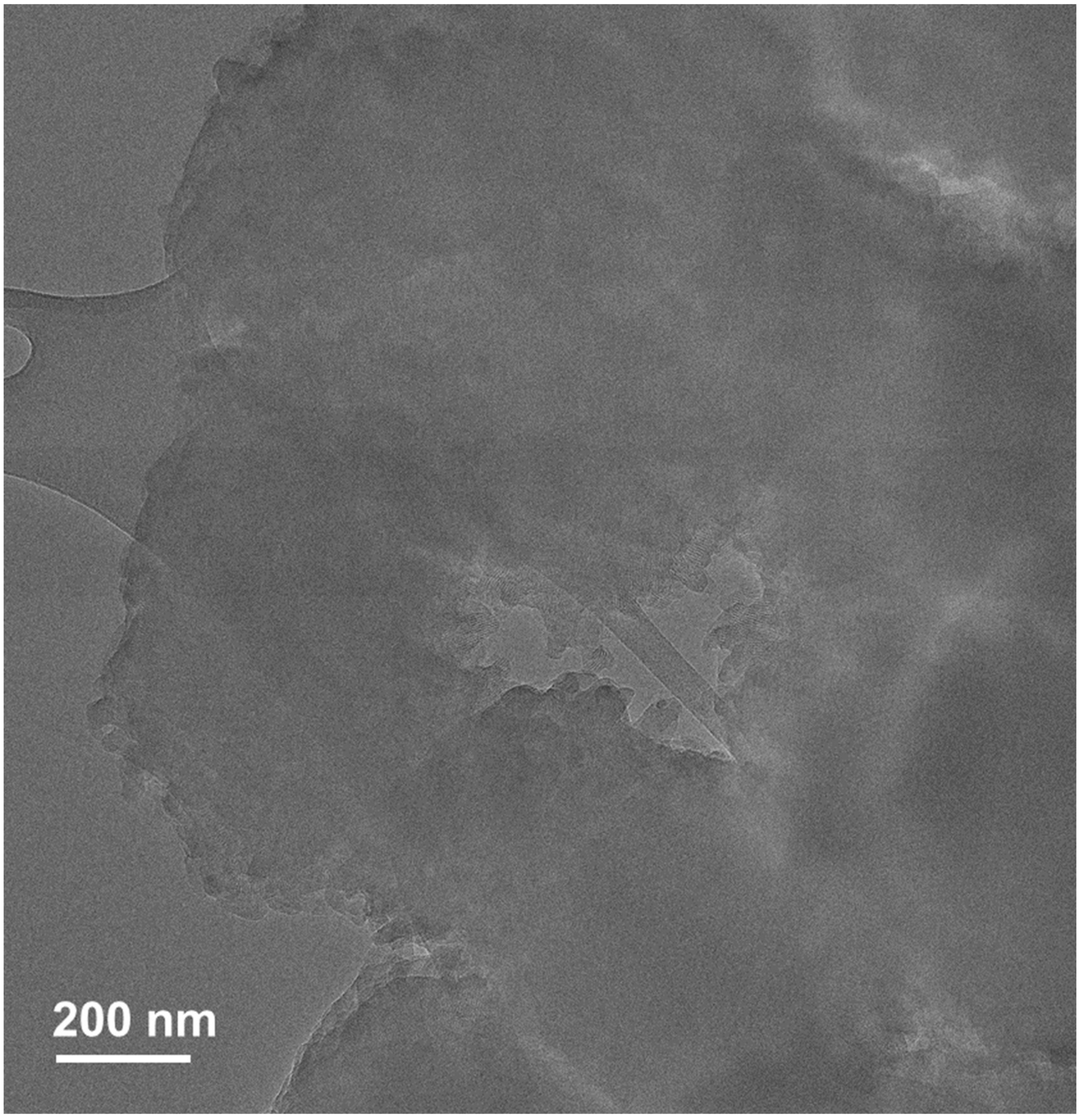

Figure S17. Transmission electron micrographs with a large-field-of-view of TAPB-NDI.

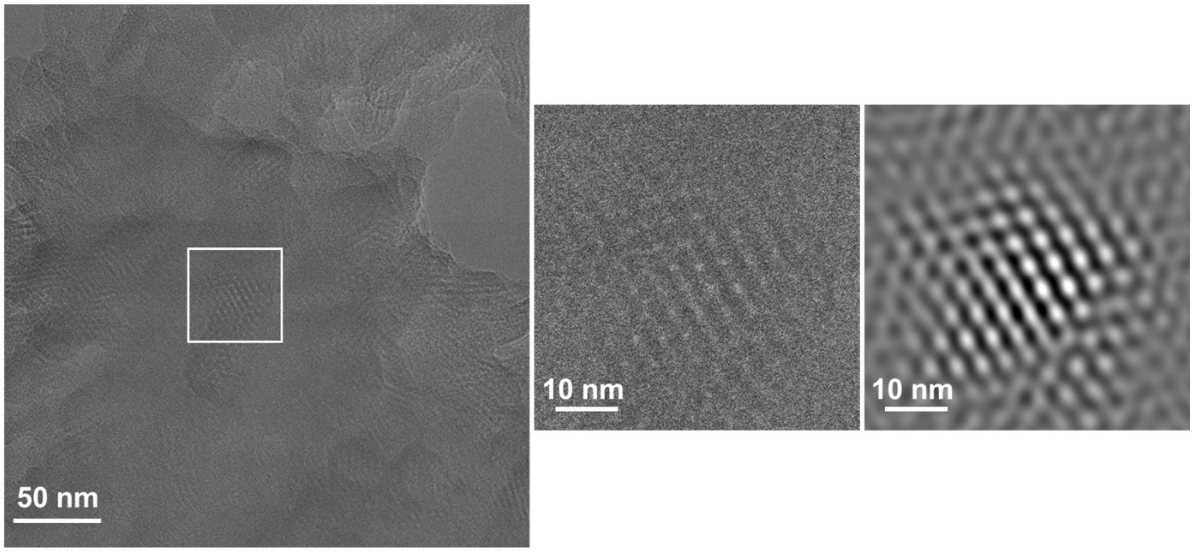

Figure S18. Transmission electron micrographs with a large-field-of-view (left), zoomed in (middle), and band-pass filtered (right) of TAPB-NDI.

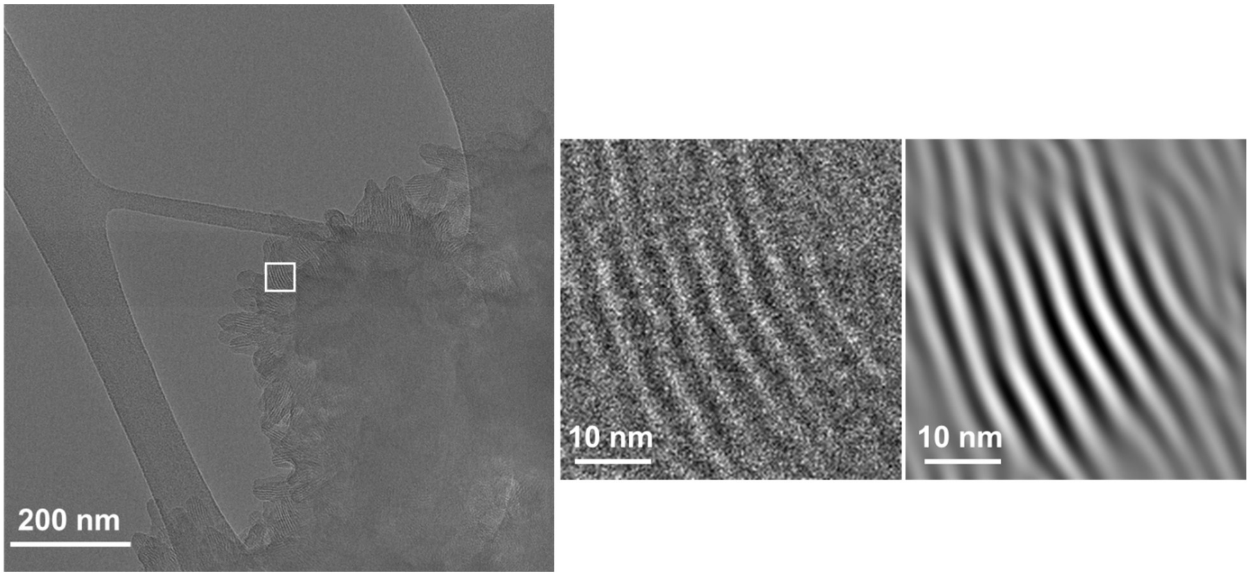

Figure S19. Transmission electron micrographs with a large-field-of-view (left), zoomed in (middle), and band-pass filtered (right) of TAPB-NDI.

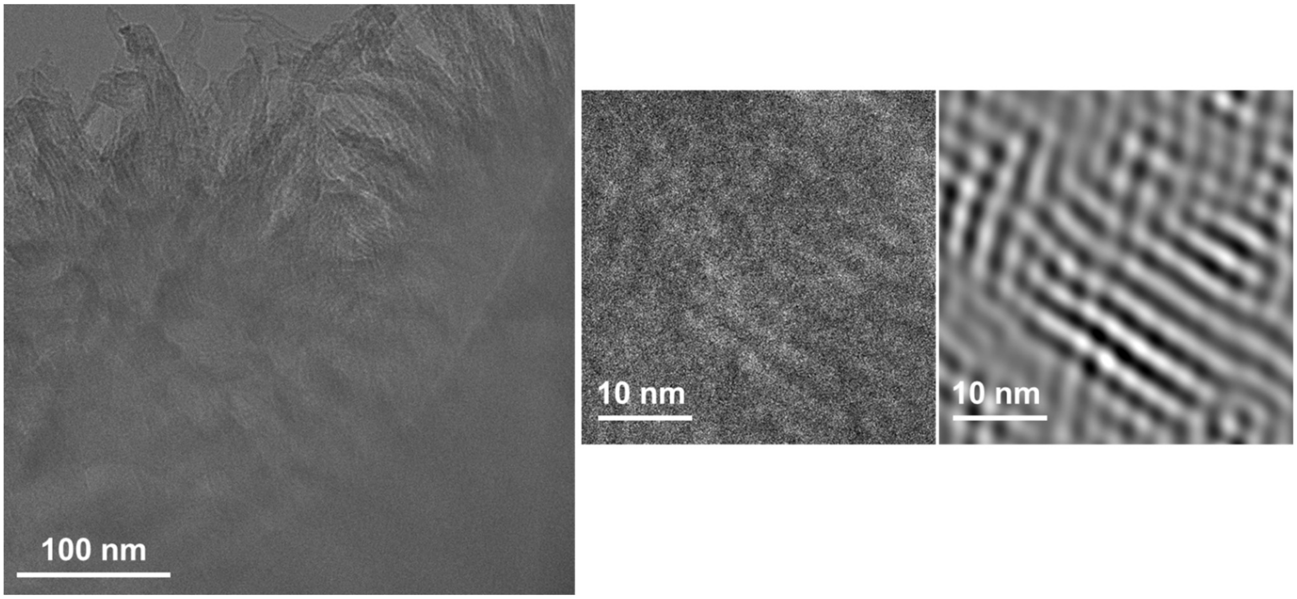

Figure S20. Transmission electron micrographs with a large-field-of-view (left), zoomed in (middle), and band-pass filtered (right) of TAPPy-NDI.

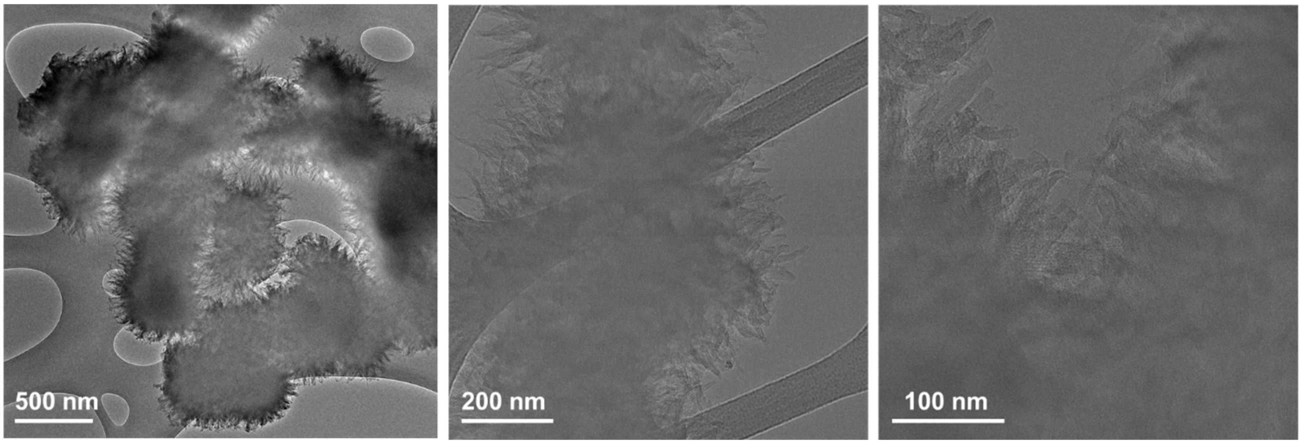

Figure S21. Transmission electron micrographs with a large-field-of-view (left), zoomed in (middle and right) of TAPPy-NDI.

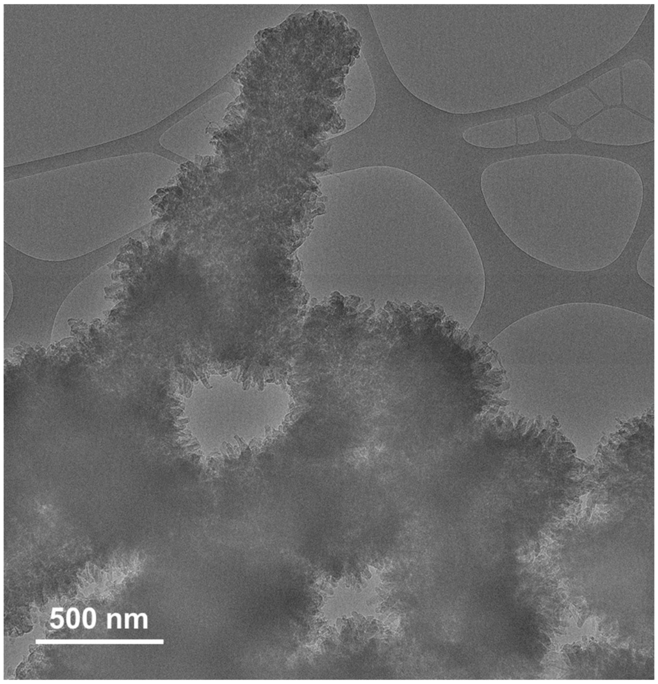

Figure S22. Transmission electron micrographs with a large-field-of-view TAPPy-NDI.

F. Molecular Doping Protocols

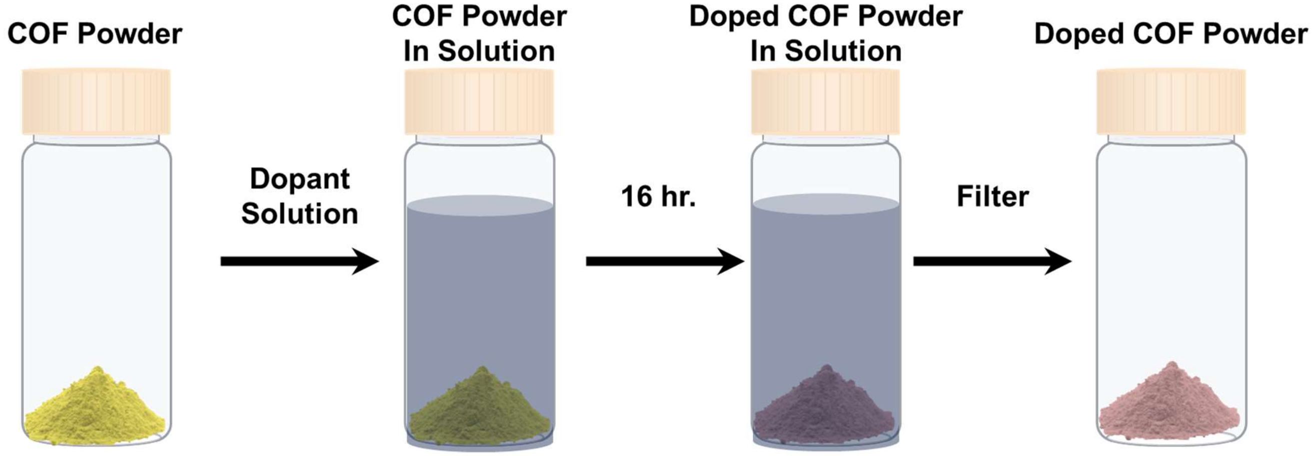

Figure S23. Illustration of the general doping protocol.

General Procedure: polycrystalline powders (typically 25-50 mg) were preweighed into prelabeled vials under a N_2 atmosphere. Then, separately, a $CoCp_2$ solution was prepared at a known concentration in anhydrous THF (See **Table S1** below for representative calculation details). Then, a volume of this molecular dopant solution was added to the powders in amounts to target the desired doping ratio. Nearly immediately the undoped powders were found to transform from a light yellow orange to a dark burgundy. 2DP powders then sat undisturbed within the dopant solution for at least 16 h. These solutions were then filtered and rinsed extensively (50 mL) with clean solvent THF. After doping, the powders were found to be a dark burgundy and were noticeably prone to static charging.

Table S1. Representative calculations for doping of NDI-Based 2DPs.

TAPB-NDI Mass/Redox Center	**868**	**g mol^{-1}**		
TAPPy-NDI Mass/Redox Center	**917**	**g mol^{-1}**		
Molecular Weight CoCp$_2$	**189**	**g mol^{-1}**		
Stock Solution Volume	**100**	**mL**		
Mass of CoCp$_2$	**50**	**mg**		
TAPB-NDI COF Per Sample	50	mg		
Moles Redox Cite Per Sample	0.0576	mmol		
TAPB-NDI Doping	Equiv.	CoCp$_2$ (mmol)	CoCp$_2$ (mg)	CoCp$_2$ (mL)
0.0 Equiv	0	0.00	0.0	**0.0**
0.2 Equiv	0.2	0.01	2.2	**4.4**
0.33 Equiv	0.33	0.02	3.6	**7.2**
0.4 Equiv	0.4	0.02	4.4	**8.7**
0.6 Equiv	0.6	0.03	6.5	**13.1**
0.8 Equiv	0.8	0.05	8.7	**17.4**
1.0 Equiv	1	0.06	10.9	**21.8**
TAPPy-NDI COF Per Sample	50	mg		
Moles Redox Cite Per Sample	0.0545	mmol		
TAPPy-NDI Doping	Equiv.	CoCp$_2$ (mmol)	CoCp$_2$ (mg)	CoCp$_2$ (mL)
0.0 Equiv	0	0.00	0.0	**0.0**
0.2 Equiv	0.2	0.01	2.1	**4.1**
0.4 Equiv	0.4	0.02	4.1	**8.2**
0.5 Equiv	0.5	0.03	5.2	**10.3**
0.6 Equiv	0.6	0.03	6.2	**12.4**
0.8 Equiv	0.8	0.04	8.2	**16.5**
1.0 Equiv	1	0.05	10.3	**20.6**

G. Optical Images

Figure S24. Representative photographs following molecular reduction of NDI-based 2DPs. 2DP powders start orange-red but immediately turn dark upon exposure to any amount of $CoCp_2$.

Figure S25. Representative photograph of molecular reduction of NDI-based 2DPs. Dark 2DP powders have settled to the bottom of the vial.

H. Diffuse Reflectance Ultraviolet Visible Spectroscopy

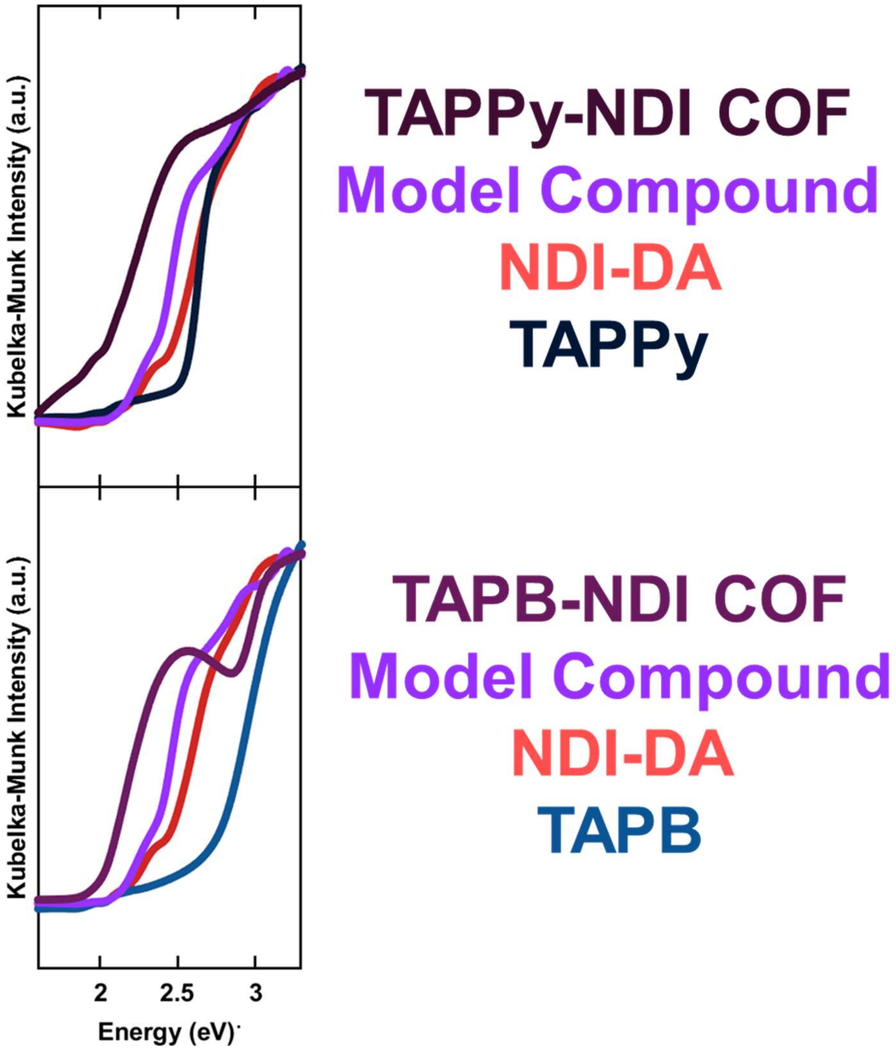

Figure S26. Overlain diffusion-reflectance spectroscopy of monomers, model compounds, and covalent organic frameworks.

I. Photoelectron Spectroscopy

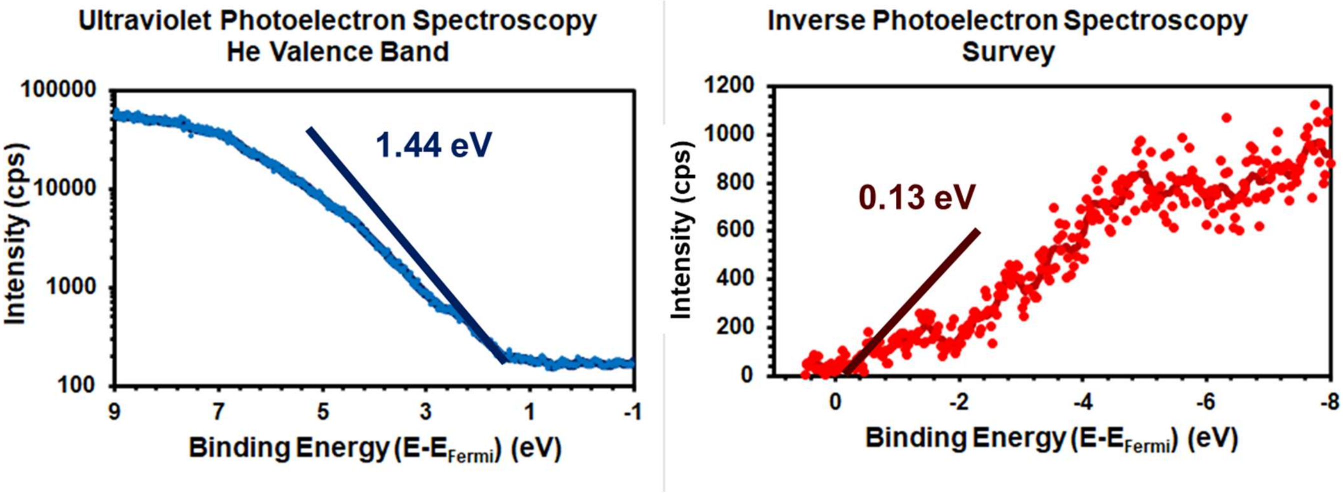

Figure S27. Ultraviolet photoelectron spectroscopy (left) and inverse photoelectron spectroscopy (right) spectra measured from a TAPPy-NDI film. The onsets of the highest occupied molecular orbital (HOMO) and lowest unoccupied molecular orbital (LUMO) for this material are at 1.44 eV below and 0.13 eV above the Fermi level, respectively. Consequently, the single-particle gap is 1.57 eV.

J. Flash-Photolysis Time-Resolved Microwave Conductivity

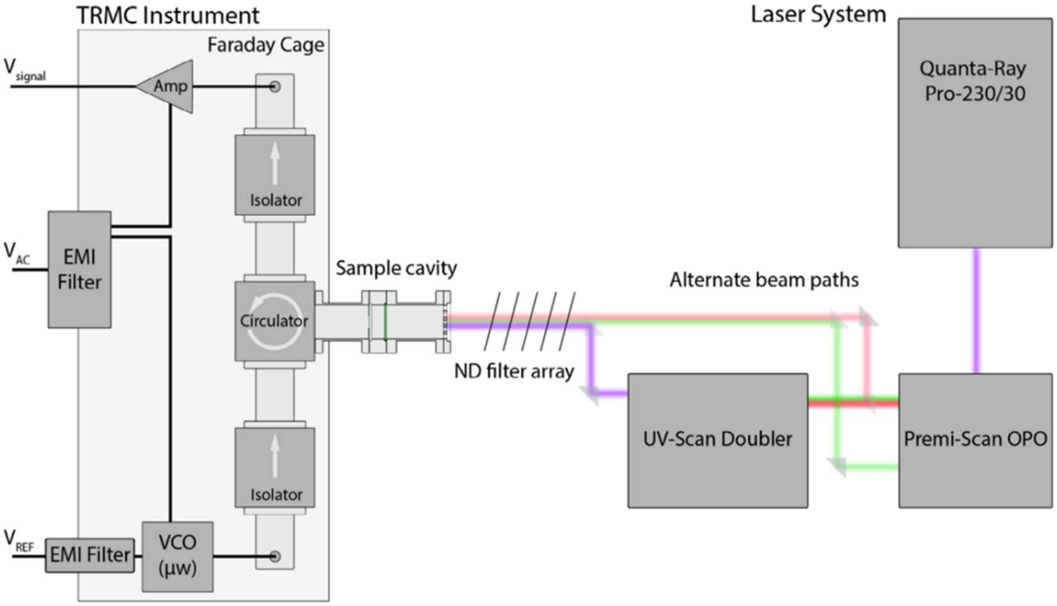

Figure S28. Schematic of the fp-TRMC experimental setup, which we have described previously.[6]

Flash-photolysis time-resolved microwave conductivity (fp-TRMC) measurements were performed at three photon energies (1.55, 2.07, and 2.76 eV) on undoped TAPB-NDI, TAPPy-NDI, and NDI monomer films to 1) establish photoconductivity at photon energies greater than or equal to the optical band edges described in the previous section, and 2) identify differences in photoconductivity and free charge lifetimes between the NDI-2DPs. Since our ~9 GHz microwave probe is only sensitive to free charges, this contactless measurement selectively detects free electrons and holes resulting from photoexcitation using a *ca.* 5 ns laser pulse at a single wavelength. Assuming negligible recombination within the instrument response, the maximum change in conductance (ΔG) due to photoinduced carriers is quantitatively related to the yield-mobility product ($\varphi\Sigma\mu$) shown in the left-hand side equation 2 (below),[3]

$$\phi \sum_i \mu_i = \phi(\mu_e + \mu_h) = \frac{\Delta G}{\beta e \mathrm{I_o} F_A} \text{ (Equation 2)}$$

where φ is quantum yield of free electrons and holes, Σμ is the sum of the GHz electron (μ_e) and hole (μ_h) mobilities, β is ratio of the microwave cavity dimensions, *e* is elementary charge, I_o is the laser intensity in units of photons cm^{-2} pulse^{-1}, and F_A is the fraction of photons absorbed at the excitation frequency.

Results from fp-TRMC, including $\varphi\Sigma\mu$ values at different excitation energies and lifetime values from a global biexponential fit over all fluences are shown in **Table S2**. Since there is little-to-no fluence dependence for $\varphi\Sigma\mu$ in these 2DPs, we report the average $\varphi\Sigma\mu$ and its standard deviation based on values at each fluence that are calculated from the sum of the amplitudes (a_1 and a_2, **Table S3**) of the biexponential fit. When excited at 2.76 and 2.07 eV, TAPB-NDI:polystyrene and TAPPy-NDI:polystyrene films showed appreciable photoconductivity and comparable $\varphi\Sigma\mu$ values (*ca.* 5 x 10^{-5} cm^2 V^{-1} s^{-1}). In agreement with the DR-UVVis spectra from earlier, TAPB-NDI showed no measurable photoconductivity when excited with 1.55 eV photons (i.e. sub-optical gap) whereas TAPPy-NDI demonstrated $\varphi\Sigma\mu$ values similar to measurements using greater photon energies. An NDIDA monomer (**Figure S1**)-polystyrene film was used as a control to establish that the photoconductivity response of the 2DPs differed from precursor compounds in a way that is consistent with our optical measurements. Indeed, the NDI monomer with an optical gap >2.5 eV only showed appreciable photoconductivity ($\varphi\Sigma\mu \sim 0.9 \times 10^{-5}$ cm^2 V^{-1} s^{-1}) at 2.76 eV, based on the lack of signal above the microwave cavity background at <2.07 eV photon energies. We suspect $\varphi\Sigma\mu$ values for the NDI monomer-polystyrene film approaching those for 2DPs (*ca.* 1 × 10^{-5} cm^2 V^{-1} s^{-1}) at 2.76 eV is likely explained by the presence of sizable NDI aggregates or perhaps crystallites that form during the relatively slow film drying time typical of drop casting. Since NDI materials are well known *n*-type transport materials,[7] the values measured here likely originate from a small number of photoinduced free electrons (i.e. low φ) with sizable mobilities.

We are not able to definitively assign the origin of the biexponential decay due to the lack of understanding around the charge generation mechanism and thus recombination in these new, neat (i.e. no complementary electron donor or acceptor present) 2DP materials. Although it is possible that these transients could be described by bimolecular charge-charge and/or exciton-charge annihilation, the low charge yields (<<5%) and the lack of fluence-dependence in $\phi\Sigma\mu$ observed in these 2DPs mean the former and latter scenarios, respectively, do not likely contribute strongly to these transients. As a result, we speculate that this is consistent with preferential trapping of either electrons or holes on the ~12 ns timescale, and that the complementary (non-trapped) charges have reasonably long (~100's of ns) lifetimes.

$\varphi\Sigma\mu$ values for the 2DPs reported here are comparable to a zinc porphyrin 2DP from our previous work measured under similar conditions.[8] In reference to the Kubo analysis performed in that study – although the average crystallite size (~100 nm) in TAPB-NDI and TAPPy-NDI powders in this work is greater than that (~30 nm) for Thomas et al., we argue that one should expect similar limitations to the maximum attainable AC mobility (*ca.* 10^{-2} cm^2 V^{-1} s^{-1}). In addition to possible crystalline imperfections and a low, but realistic charge yield (likely < 10%),[2, 6, 8, 9] we believe the (electron + hole) GHz AC mobility within these 2DP crystallites of *ca.* 10^{-4} cm^2 V^{-1} s^{-1} or greater is reasonable.

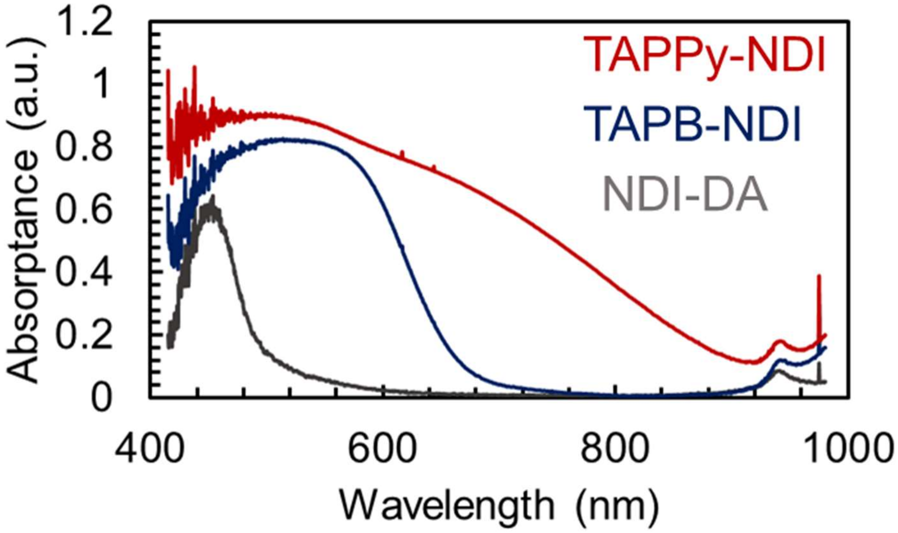

Figure S29. Integrating sphere absorption measurements of TAPPy-NDI (red), TAPB-NDI (blue), and molecular NDI-DA (grey).

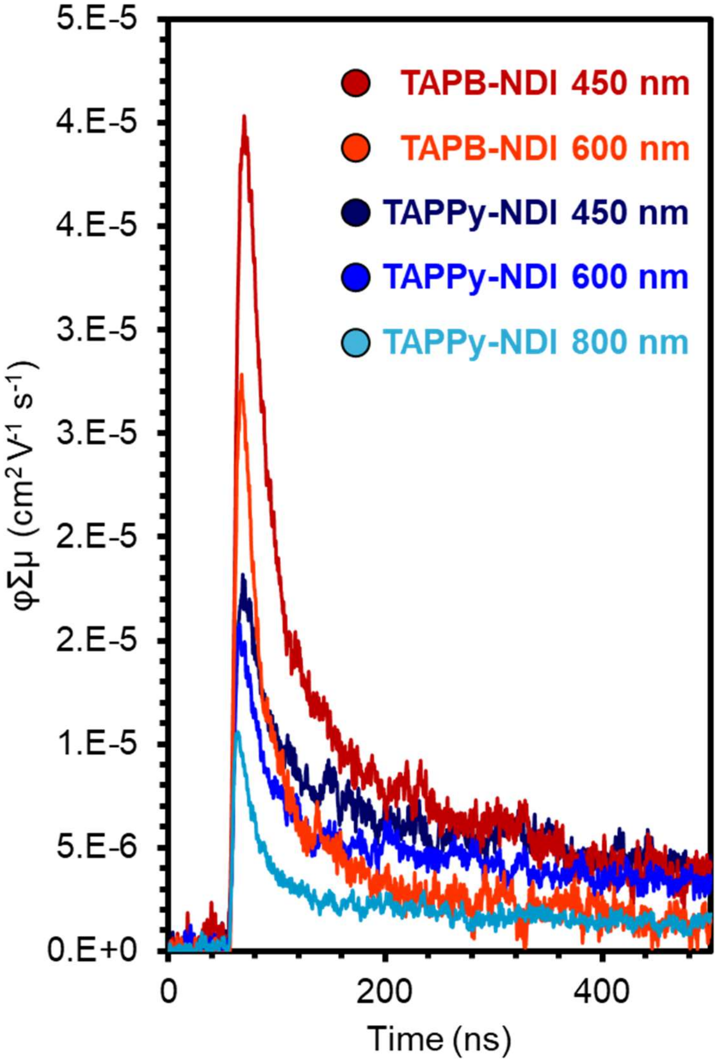

Figure S30. Fp-TRMC of both 2DPs at several excitation wavelengths. Fluences: 450 nm (3 × 10^{15} photons cm^{-2}), 600 nm (2.16 × 10^{15} photons cm^{-2}), 800 nm (8.2 × 10^{15} photons cm^{-2})

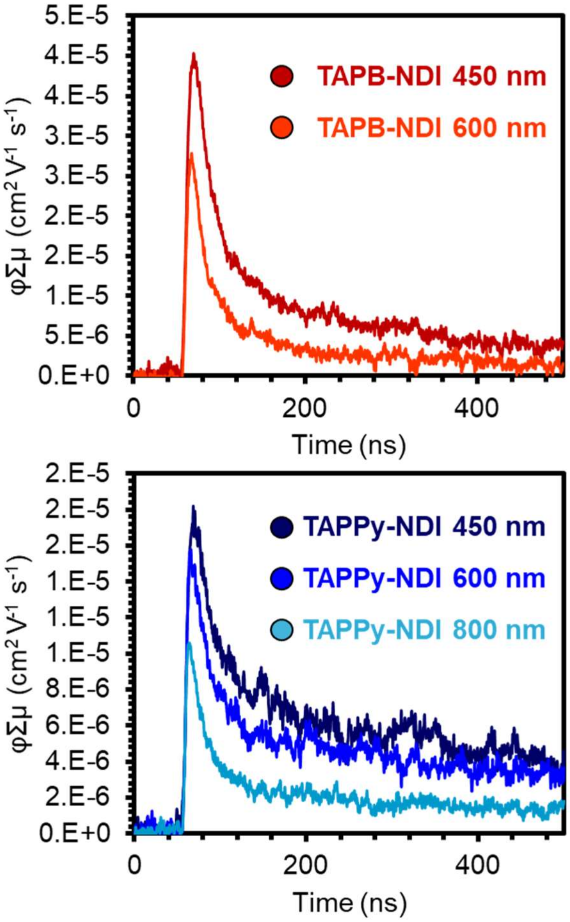

Figure S31. Fp-TRMC of both 2DPs at several excitation wavelengths. Fluences: 450 nm (3 × 10^{15} photons cm^{-2}), 600 nm (2.16 × 10^{15} photons cm^{-2}), 800 nm (8.2 × 10^{15} photons cm^{-2})

Table S2. fp-TRMC results at three excitation energies: Amplitude-weighted average time constants (<t>), and biexponential, global fit parameters.

	Exc. (eV)	NDI-DA:PS	TAPB-NDI:PS	TAPPy-NDI:PS
$\varphi\Sigma\mu$ (10^{-5} cm^2 V^{-1} s^{-1})	2.76	~0.9	6 ± 2	5 ± 1
	2.07		8 ± 2	5 ± 1
	1.55			3 ± 2
<t> (ns)	2.76	~300	56 ± 3	96 ± 5
	2.07		32 ± 15	66 ± 4
	1.55			28 ± 7

Table S3. Summary of global biexponential fit parameters for a representative fluence. Common fit parameters to all samples: gaussian-exponential convoluted IRF peak position = 5.76 ns, IRF sigma = 1.7 ns, IRF decay = 10 ns. PS = polystyrene.

TAPB-NDI:PS				
Exc. (eV)	**a_1**	**τ_1 (s)**	**a_2**	**τ_2 (s)**
2.76	6.21E-05	1.21E-08	1.07E-05	2.97E-07
2.07	1.41E-04	9.42E-09	8.36E-06	2.77E-07
TAPPy-NDI:PS				
	a_1	**τ_1 (s)**	**a_2**	**τ_2 (s)**
2.76	4.40E-05	7.60E-09	1.35E-05	4.15E-07
2.07	8.72E-05	6.04E-09	1.47E-05	3.84E-07
1.55	7.26E-05	4.16E-09	7.47E-06	3.51E-07
NDIDA monomer:PS				
	a_1	**τ_1 (s)**	**a_2**	**τ_2 (s)**
2.76	3.06E-06	1.85E-08	6.17E-06	4.43E-07

K. Density Functional Theory Calculations

The electronic-structure calculations were carried out at the density functional theory (DFT) level. To reduce computational time, all hexyl side chains of TAPB-NDI and TAPPy-NDI were replaced with ethyl groups. The geometry optimizations were performed at the PBE level with D3 van der Waals (vdW) dispersion corrections,[10] using the Vienna Ab initio Simulation Package (VASP)[11]. Γ-centered Monkhorst-Pack *k*-meshes of 1 × 1 × 13 and 1 × 1 × 9 were adopted in the geometry optimizations of TAPB-NDI and TAPPy-NDI, respectively. The energy cutoff of plane waves was 500 eV. The lattice parameters obtained after geometry optimization of TAPB-NDI and TAPPy-NDI are shown in **Table S4**. Optimized lattice parameters for bulk TAPB-NDI and TAPPy-NDI. Based on the optimized crystal structures, the electronic band structures were calculated with the PBE0[12] functional and the POB-TZVF[13] basis set, using the CRYSTAL17[14] package.

The projected density of states (PDOS) and optical absorption spectra are calculated using VASP[11] and VASPKIT[15]. Γ-centered Monkhorst-Pack *k*-meshes of 2 × 2 × 28 and 2 × 2 × 14 were used in these calculations. These calculations were performed at the PBE level to reduce the computational cost. The simulated optical absorption spectra show weak absorption peaks around 0.3 and 0.7 eV for TAPPy-NDI and TAPB-NDI, respectively. The weak and broad absorptions in both cases show a charge-transfer character, which is confirmed by the calculated PDOS, where the top valence bands are dominated by contributions from TAPPy/TAPB, and the bottom conduction bands by contributions from the NDI moieties. (We recall that the electronic gaps calculated at the PBE level are much smaller than those at the PBE0[12] level (**Figure 3**), which is related to the over- delocalization of the wave functions at the PBE level).

The neutral and negatively charged NDI molecules with phenyl and ethyl capping groups were optimized at the PBE0 level with the 6-31G(d,p) basis set using Gaussian16[16]. The simulated IR spectra for the neutral and charged species are given in **Figure S10**.

Table S4. Optimized lattice parameters for bulk TAPB-NDI and TAPPy-NDI.

	a(Å)	b(Å)	c(Å)	α(°)	β(°)	γ(°)
TAPB-NDI	55.87	55.87	3.92	90.00	90.00	120.01
TAPPy-NDI	34.28	30.40	4.24	75.51	78.50	40.74

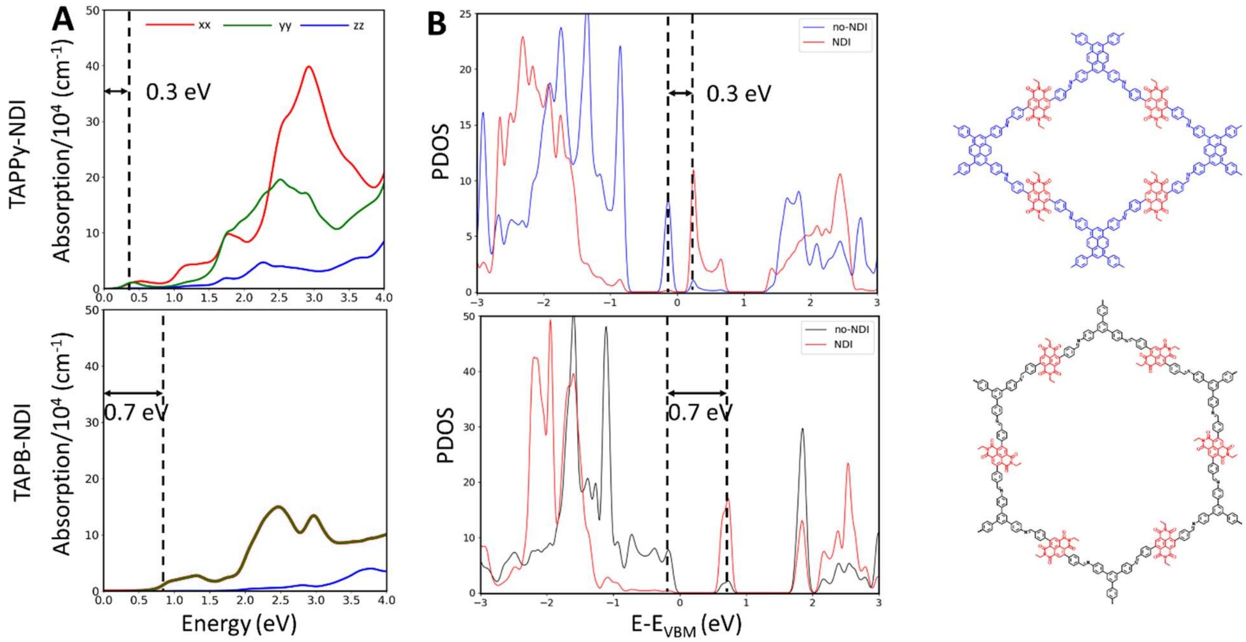

Figure S32. A) Simulated optical absorption spectra for bulk TAPPy-NDI and TAPB-NDI. **B)** Projected density of states to the NDI and non-NDI fragments of the 2DPs.

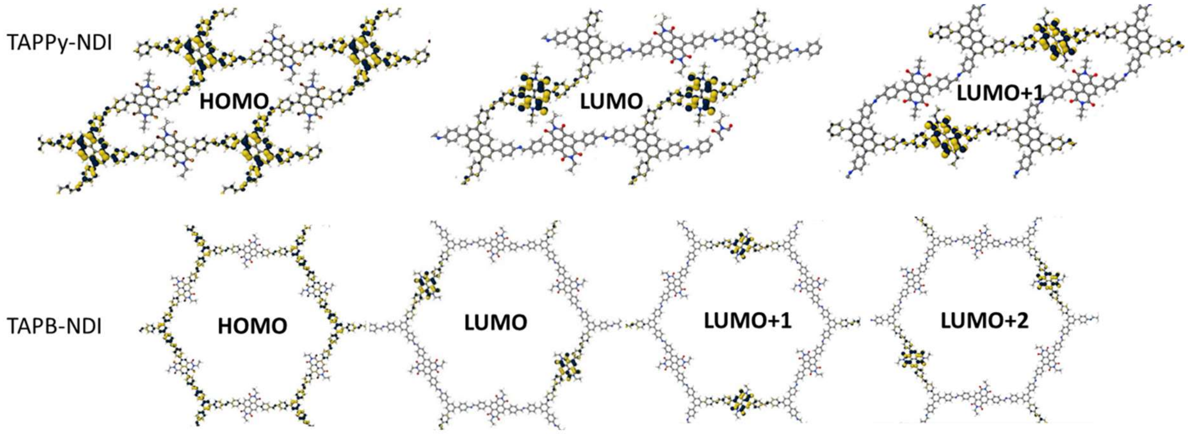

Figure S33. Wave functions at the Γ point for monolayers of TAPPy-NDI and TAPB-NDI.

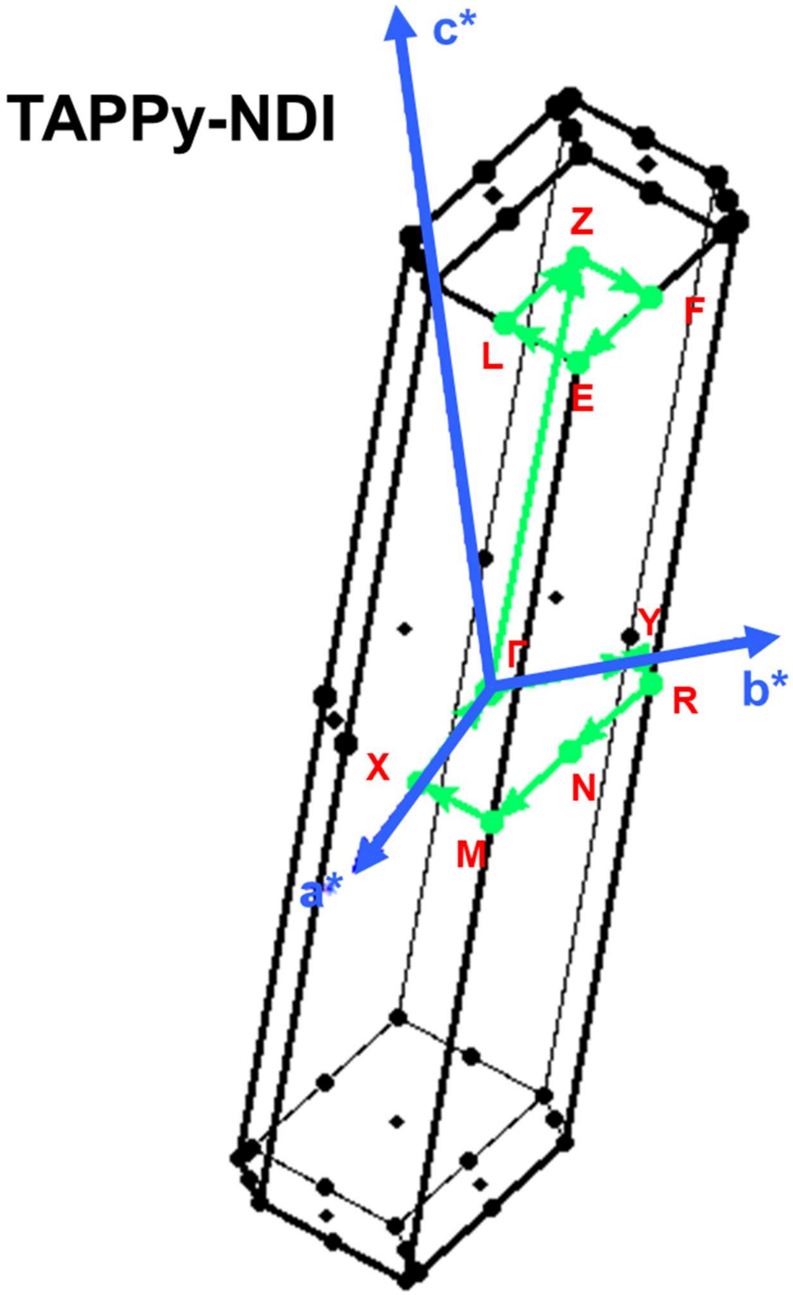

Figure S34. Brillouin zone of bulk TAPPy-NDI.

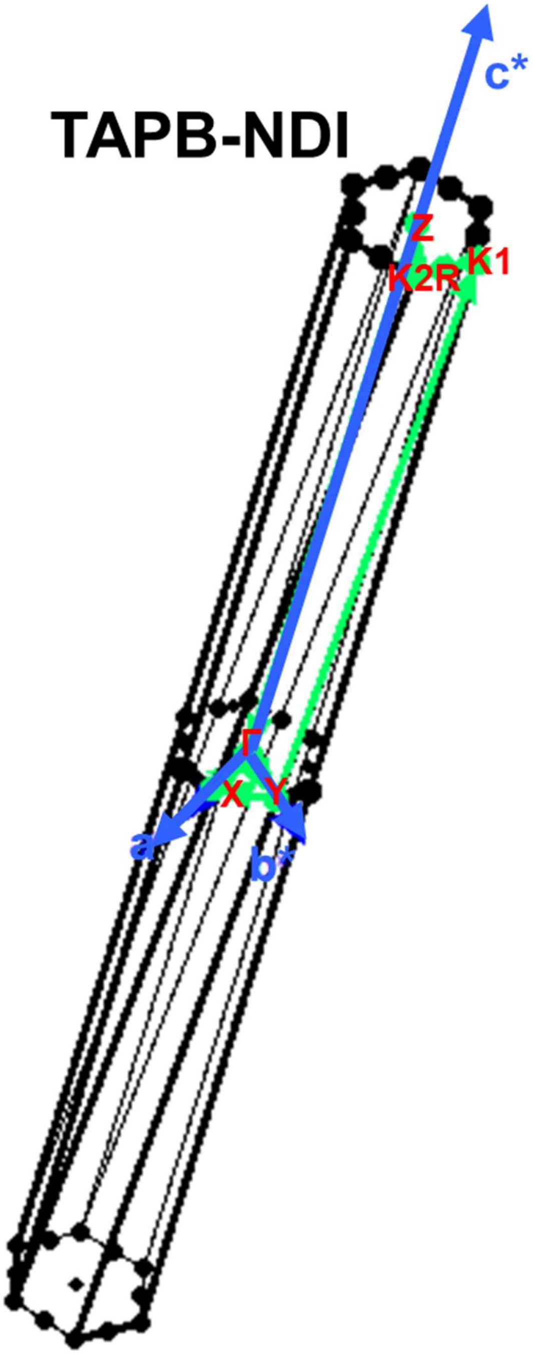

Figure S35. Brillouin zone of bulk TAPB-NDI.

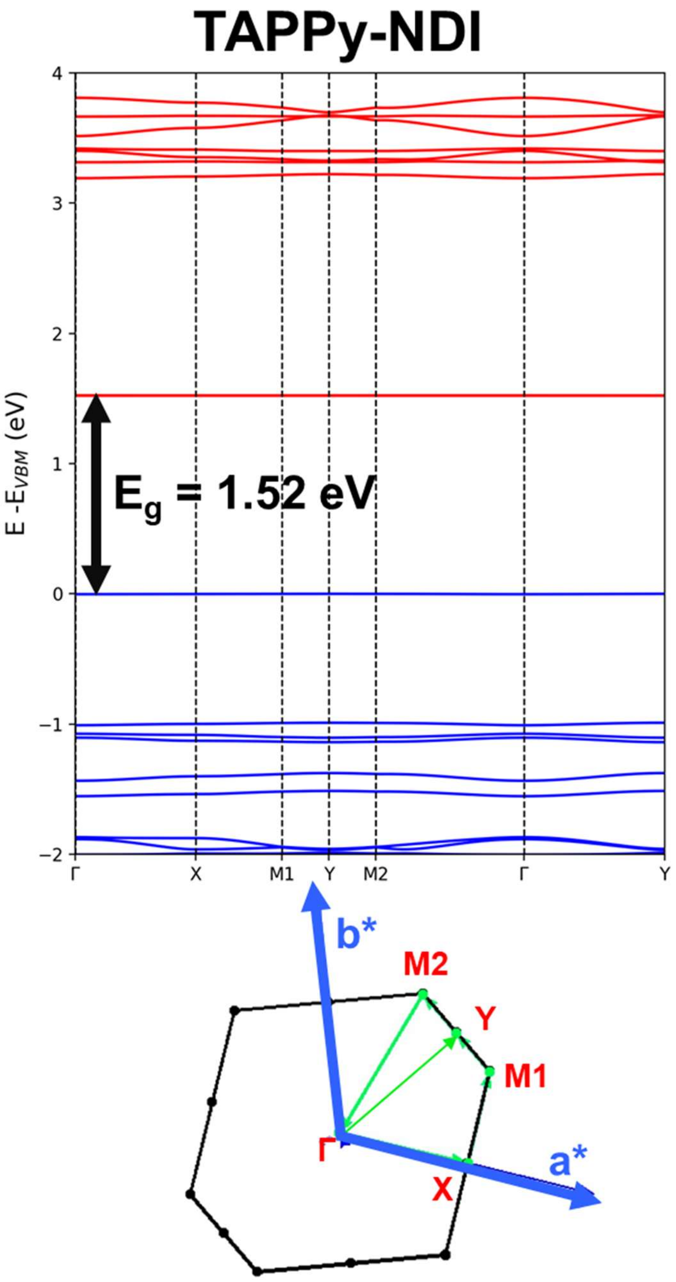

Figure S36. Electronic band structure of a monolayer of TAPPy-NDI.

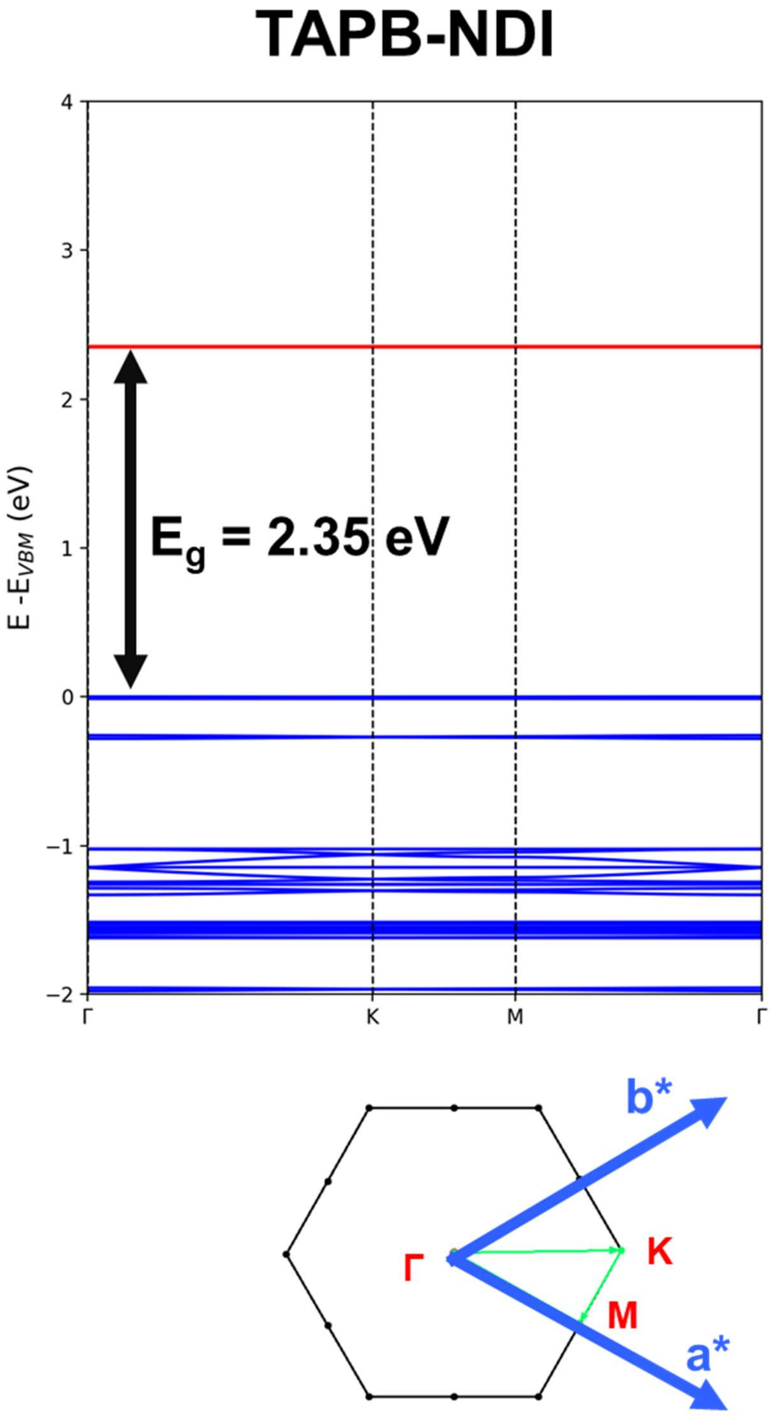

Figure S37. Electronic band structure of a monolayer of TAPB-NDI.

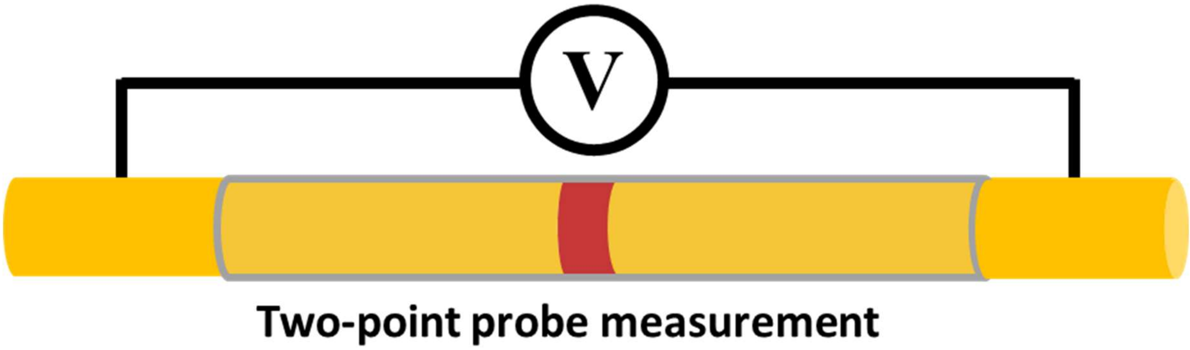

Figure S38. Schematic of two-point probe measurement.

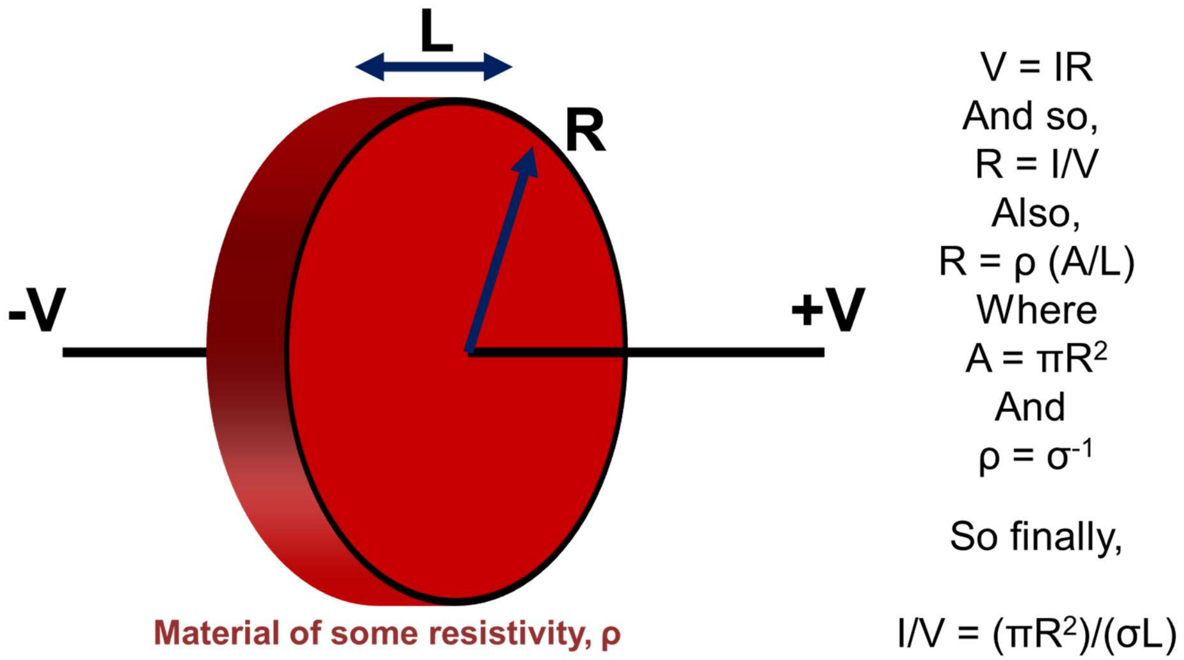

$V = IR$
And so,
$R = I/V$
Also,
$R = \rho\ (A/L)$
Where
$A = \pi R^2$
And
$\rho = \sigma^{-1}$

So finally,

$I/V = (\pi R^2)/(\sigma L)$

Figure S39. Scaling law of an Ohmic resistor.

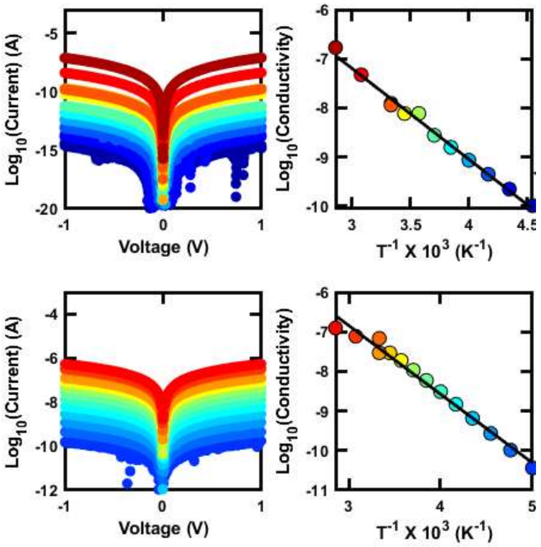

Figure S40. Arrhenius behavior of doped 2DP semiconductors. Top: TAPPy-NDI at 0.5 equiv. doping. Bottom: TAPB-NDI at 1.0 equiv. doping with $CoCp_2$.

L. Electron Paramagnetic Resonance Spectra

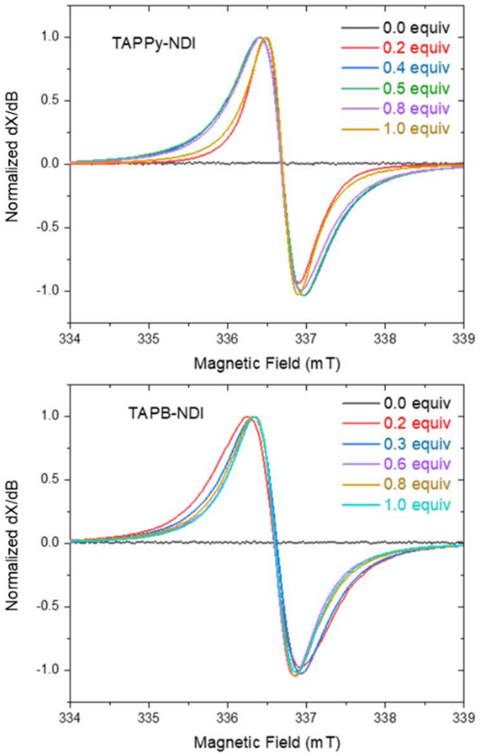

Figure S41. Normalized X-band EPR spectra for variable doped NDI-based 2DPs recorded at 5.0 K.

All EPR spectra exhibit a Lorentzian line shape (see Fig S41-S45) suggesting that unpaired electrons most probably reside in the collective delocalized orbitals, as localized states would experience (un)resolved hyperfine splitting that would result in a Gaussian lineshape.[17] The TAPB-NDI series shows somewhat broader linewidth compared to TAPPy-NDI series that systematically decreases with the doping level suggesting motional narrowing or a narrowing mechanism that effectively reduces dipolar broadening and other inhomogeneous contributions to the resonance width upon increased doping. The linewidth of TAPPy series on the other hand is narrower compared to TAPPB series, however it increases with doping up to the concentration of 0.8 equivalents most probably due to enhanced interaction between like spins.[18]

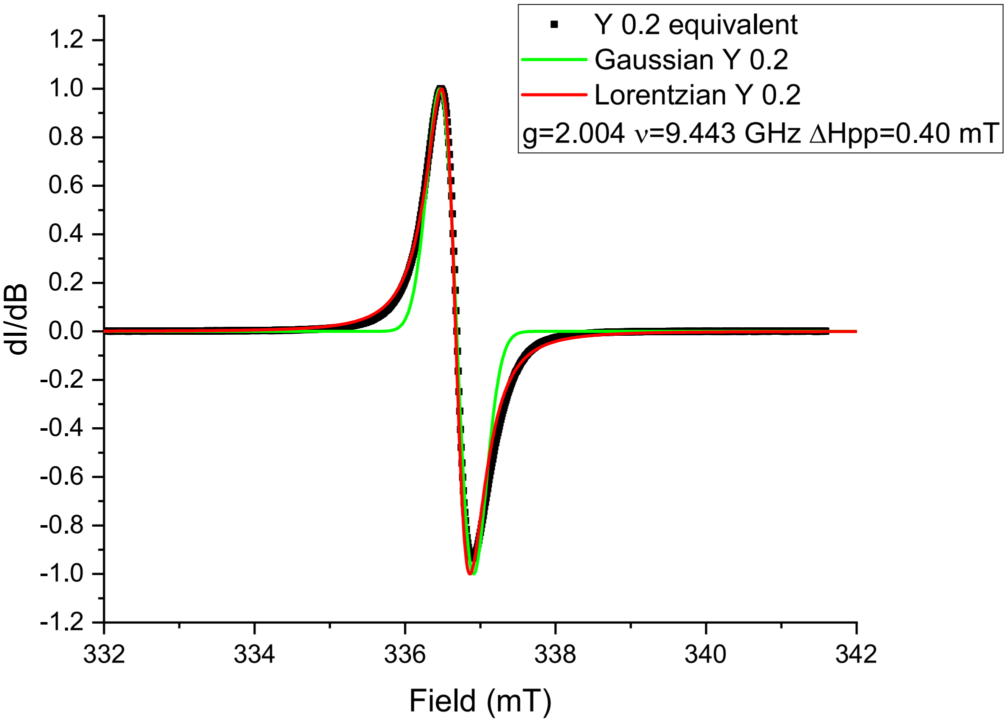

Figure S42. EPR spectra for TAPPy-NDI doped with 0.2 equiv of $CoCp_2$. Fitting parameters are shown in the inset.

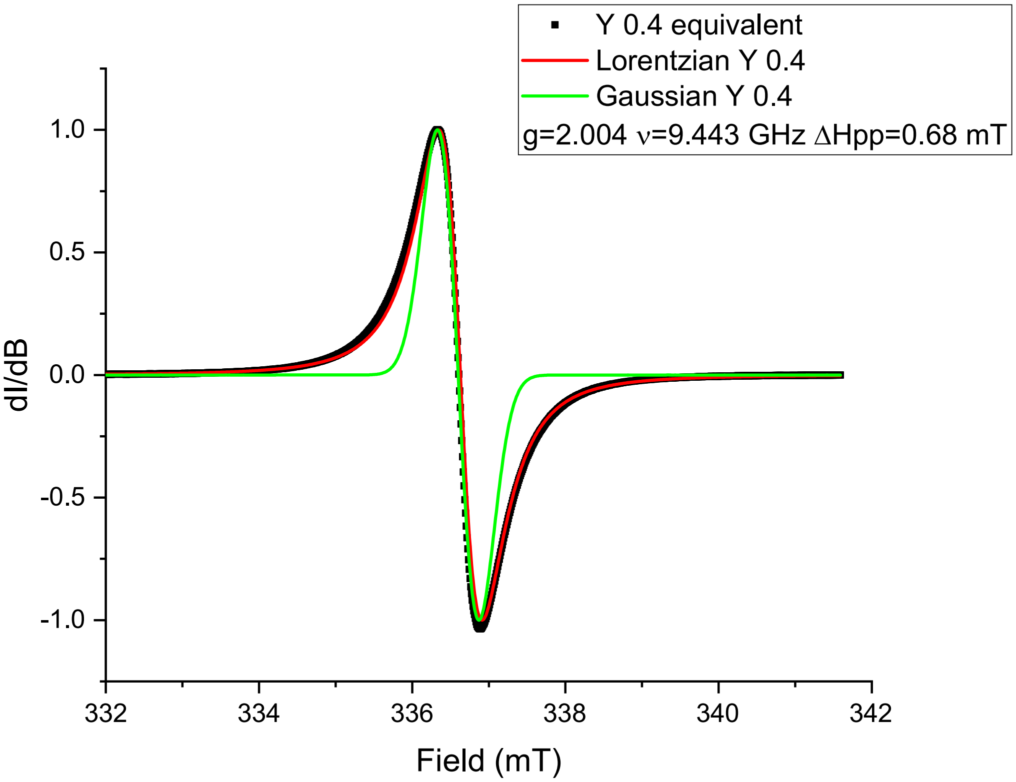

Figure S43. EPR spectra for TAPPy-NDI doped with 0.4 equiv of $CoCp_2$. Fitting parameters are shown in the inset.

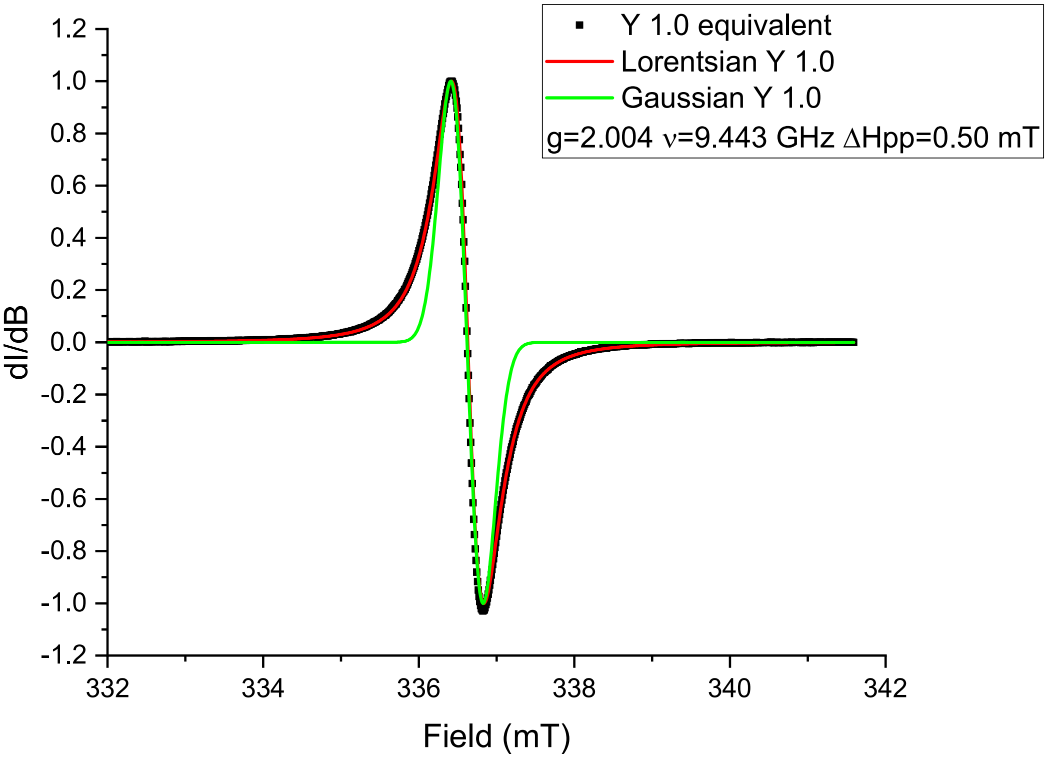

Figure S44. EPR spectra for TAPPy-NDI doped with 1.0 equiv of $CoCp_2$. Fitting parameters are shown in the inset.

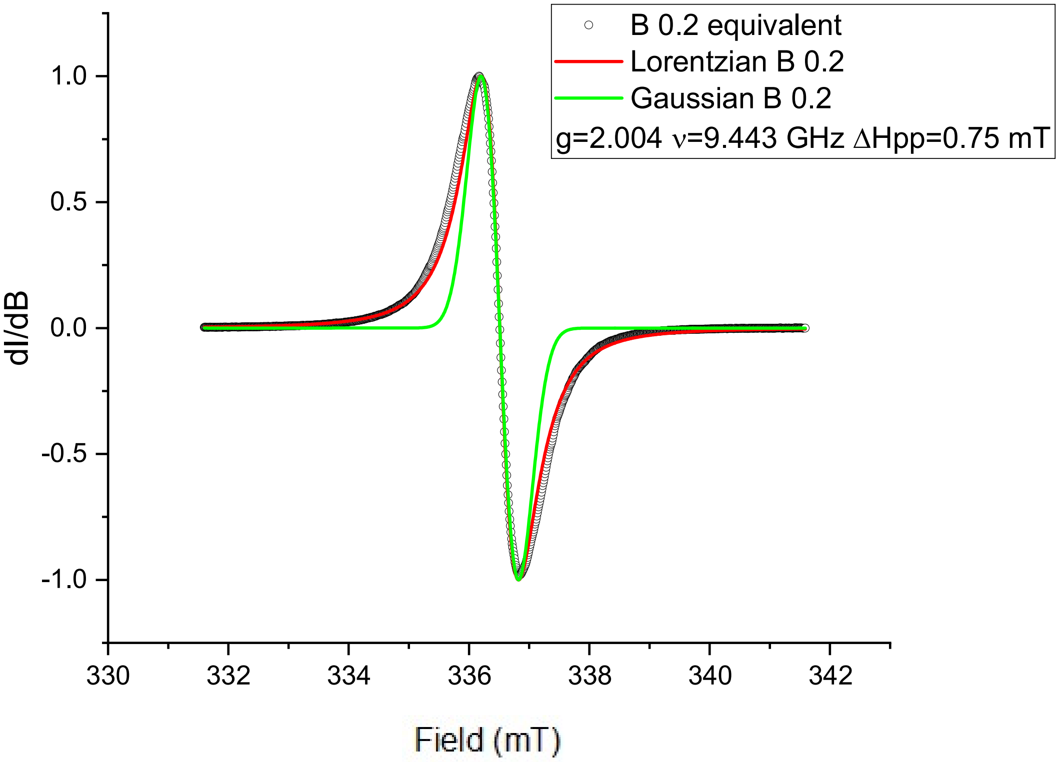

Figure S45. EPR spectra for TAPB-NDI doped with 0.2 equiv of $CoCp_2$. Fitting parameters are shown in the inset.

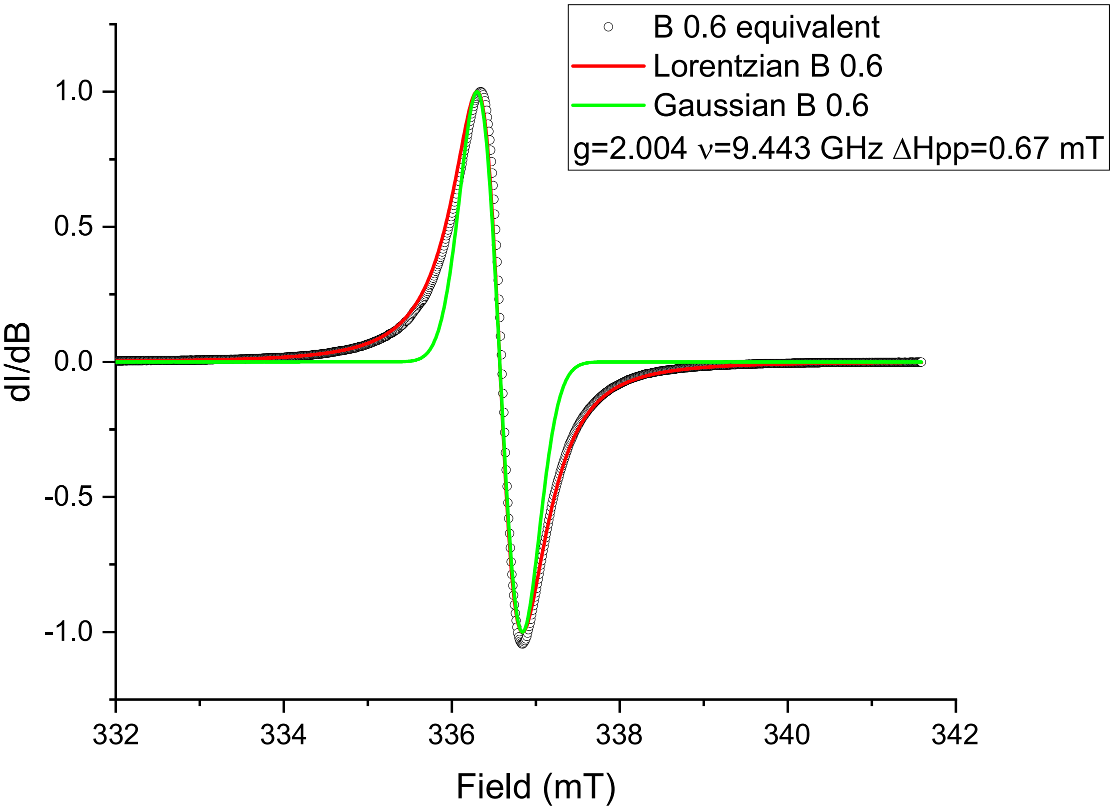

Figure S46. EPR spectra for TAPB-NDI doped with 0.6 equiv of $CoCp_2$. Fitting parameters are shown in the inset.

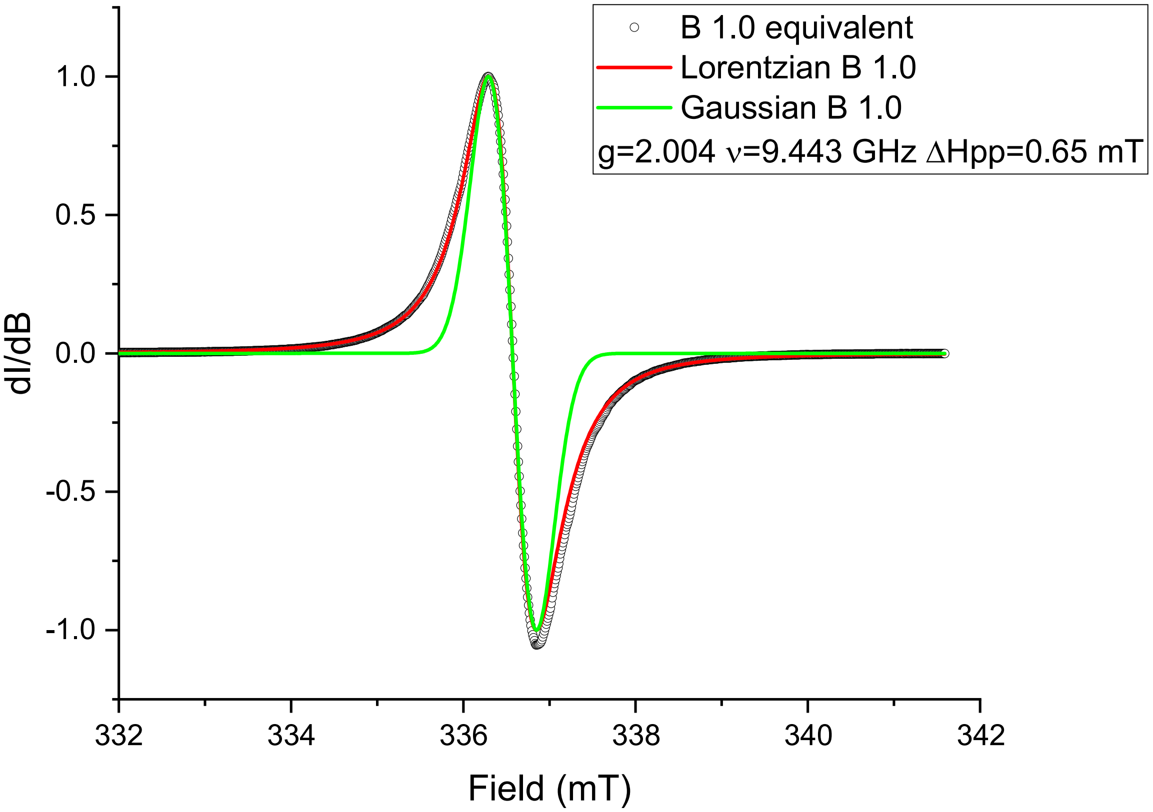

Figure S47. EPR spectra for TAPPy-NDI doped with 1.0 equiv of $CoCp_2$. Fitting parameters are shown in the inset.

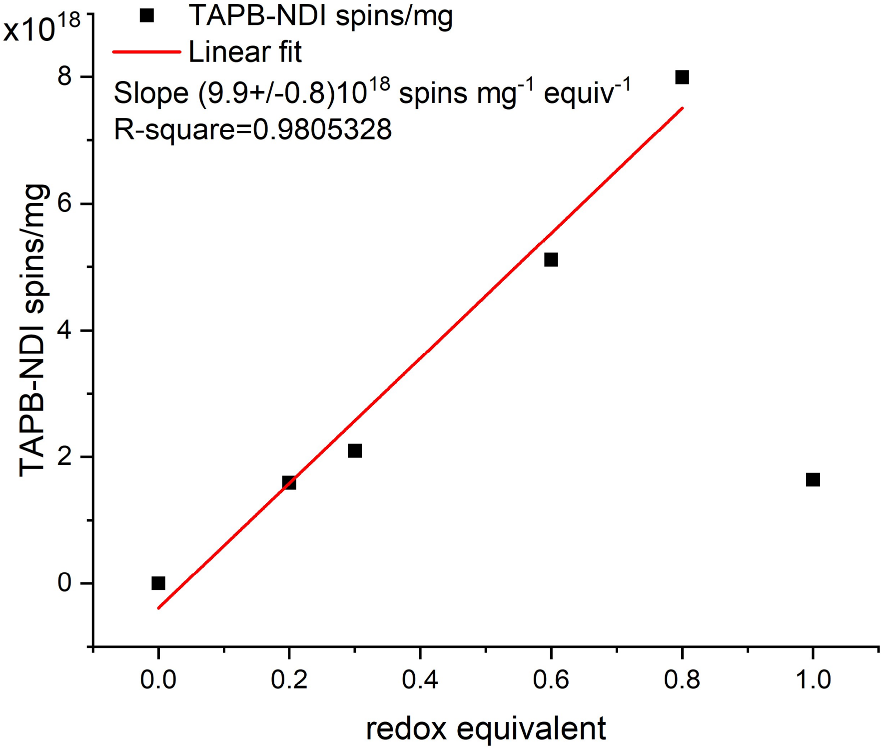

Figure S48. Quantitative analysis of TAPB-NDIsamples obtained using *X-EPR Quantitative Analysis, SpinCount Module*. The number of measured spins were obtained from the surface area of each signal by double integrating the signal, and the number of spins per volume were determined by measuring the volume of each sample (EPR tube inner diameter and the sample height). The number of spins were corrected for the active length of the ER 4122SHQE resonator, variation in signal over this length, and the effective filling factor. Along with the effects of modulation amplitude, power, time constant and other experimental parameters, these corrections were directly accounted for.

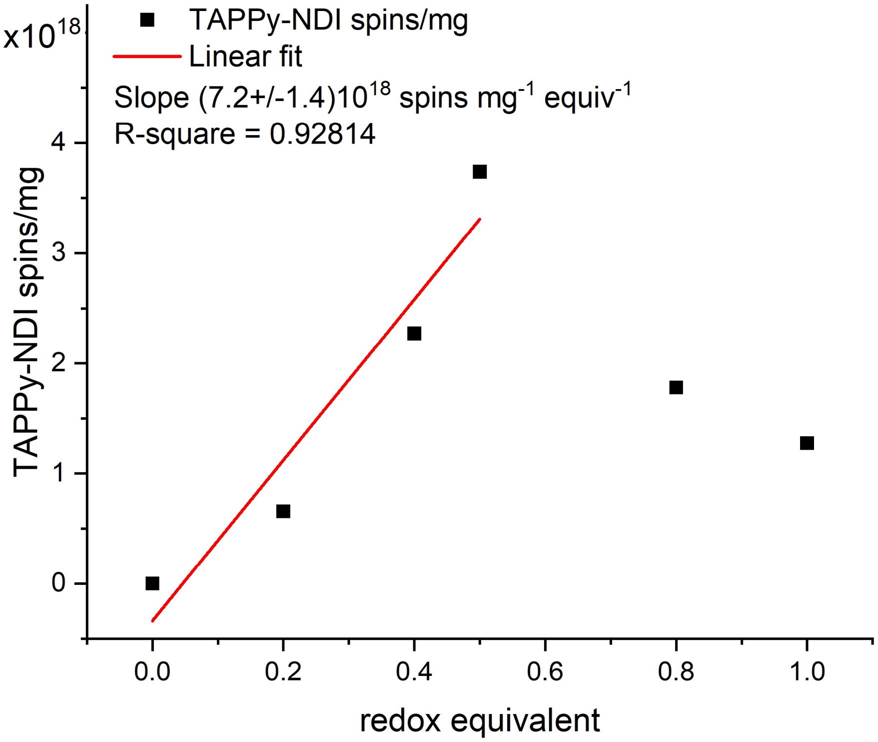

Figure S49. Quantitative analysis of TAPPy-NDI samples obtained using *X-EPR Quantitative Analysis, SpinCount Module*. The number of measured spins were obtained from the surface area of each signal by double integrating the signal, and the number of spins per volume were determined by measuring the volume of each sample (EPR tube inner diameter and the sample height). The number of spins were corrected for the active length of the ER 4122SHQE resonator, variation in signal over this length, and the effective filling factor. These effects and effects of modulation amplitude, power, time constant and other experimental parameters were directly accounted for using Bruker proprietary software.

M. Cyclic Voltammetry

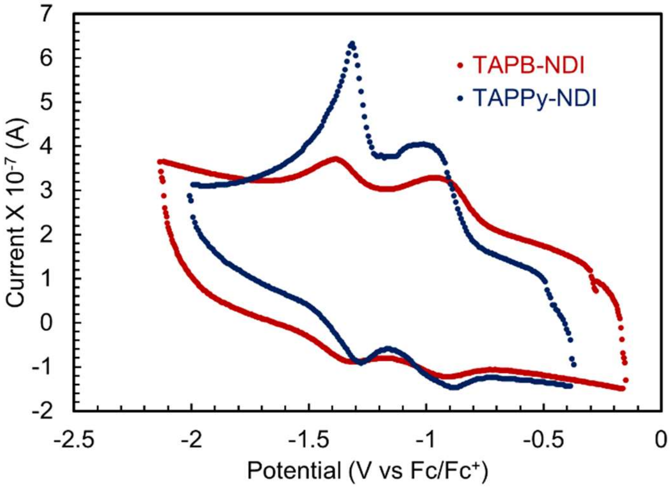

Figure S50. Cyclic voltammetry performed on doped NDI-based 2DPs.

N. References

[1] A. S. Stefan Stoll, *J. Magn. Reson.* **2006**, *178*, 42.
[2] O. G. Reid, D. T. Moore, Z. Li, D. Zhao, Y. Yan, K. Zhu, G. Rumbles, *J. Phys. D Appl. Phys.* **2017**, *50*, 493002.
[3] T. J. Savenije, A. J. Ferguson, N. Kopidakis, G. Rumbles, *J. Phys. Chem. C* **2013**, *117*, 24085.
[4] S. Jhulki, C. H. Feriante, R. Mysyk, A. M. Evans, A. Magasinski, A. S. Raman, K. Turcheniuk, S. Barlow, W. R. Dichtel, G. Yushin, S. R. Marder, *ACS Appl. Energy Mater.* **2020**.
[5] F. Auras, L. Ascherl, A. H. Hakimioun, J. T. Margraf, F. C. Hanusch, S. Reuter, D. Bessinger, M. Döblinger, C. Hettstedt, K. Karaghiosoff, S. Herbert, P. Knochel, T. Clark, T. Bein, *J. Am. Chem. Soc.* **2016**, *138*, 16703.
[6] O. G. Reid, R. D. Pensack, Y. Song, G. D. Scholes, G. Rumbles, *Chem. Mater.* **2014**, *26*, 561.
[7] M. Al Kobaisi, S. V. Bhosale, K. Latham, A. M. Raynor, S. V. Bhosale, *Chem. Rev.* **2016**, *116*, 11685; N. Sakai, J. Mareda, E. Vauthey, S. Matile, *Chem. Commun.* **2010**, *46*, 4225; G. Andric, J. F. Boas, A. M. Bond, G. D. Fallon, K. P. Ghiggino, C. F. Hogan, J. A. Hutchison, M. A.-P. Lee, S. J. Langford, J. R. Pilbrow, *Aust. J. Chem.* **2004**, *57*, 1011.
[8] S. Thomas, H. Li, R. R. Dasari, A. M. Evans, I. Castano, T. G. Allen, O. G. Reid, G. Rumbles, W. R. Dichtel, N. C. Gianneschi, S. R. Marder, *Mater. Horizon* **2019**, *6*, 1868.
[9] O. G. Reid, G. Rumbles, *J. Phys. Chem. Lett.* **2013**, *4*, 2348; O. G. Reid, J. A. N. Malik, G. Latini, S. Dayal, N. Kopidakis, C. Silva, N. Stingelin, G. Rumbles, *J. Polym. Sci., Part B: Polym. Phys.* **2012**, *50*, 27.
[10] S. Grimme, S. Ehrlich, L. Goerigk, *Journal of Computational Chemistry* **2011**, *32*, 1456; J. P. Perdew, K. Burke, M. Ernzerhof, *Physical Review Letters* **1996**, *77*, 3865.
[11] G. Kresse, J. Furthmüller, *Computational Materials Science* **1996**, *6*, 15.
[12] C. Adamo, G. E. Scuseria, V. Barone, *The Journal of Chemical Physics* **1999**, *111*, 2889.
[13] M. F. Peintinger, D. V. Oliveira, T. Bredow, *Journal of Computational Chemistry* **2013**, *34*, 451.
[14] R. Dovesi, A. Erba, R. Orlando, C. M. Zicovich-Wilson, B. Civalleri, L. Maschio, M. Rérat, S. Casassa, J. Baima, S. Salustro, B. Kirtman, *WIREs Computational Molecular Science* **2018**, *8*, e1360.
[15] V. Wang, N. Xu, J. C. Liu, G. Tang, W.-T. Geng, *arXiv:1908.08269* **2020**.
[16] Gaussian 16, Revision C.01, M. J. Frisch, G. W. Trucks, H. B. Schlegel, G. E. Scuseria, M. A. Robb, J. R. Cheeseman, G. Scalmani, V. Barone, G. A. Petersson, H. Nakatsuji, X. Li, M. Caricato, A. V. Marenich, J. Bloino, B. G. Janesko, R. Gomperts, B. Mennucci, H. P. Hratchian, J. V. Ortiz, A. F. Izmaylov, J. L. Sonnenberg, Williams, F. Ding, F. Lipparini, F. Egidi, J. Goings, B. Peng, A. Petrone, T. Henderson, D. Ranasinghe, V. G. Zakrzewski, J. Gao, N. Rega, G. Zheng, W. Liang, M. Hada, M. Ehara, K. Toyota, R. Fukuda, J. Hasegawa, M. Ishida, T. Nakajima, Y. Honda, O. Kitao, H. Nakai, T. Vreven, K. Throssell, J. A. Montgomery Jr., J. E. Peralta, F. Ogliaro, M. J. Bearpark, J. J. Heyd, E. N. Brothers, K. N. Kudin, V. N. Staroverov, T. A. Keith, R. Kobayashi, J. Normand, K. Raghavachari, A. P. Rendell, J. C. Burant, S. S. Iyengar, J. Tomasi, M. Cossi, J. M. Millam, M. Klene, C. Adamo, R. Cammi, J. W. Ochterski, R. L. Martin, K. Morokuma, O. Farkas, J. B. Foresman, D. J. Fox, Wallingford, CT 2016.

[17] A. S. Luka Ćirić, Dejan M. Djokić, Rita Smajda, Arnaud Magrez, Tommy Kaspar, Reinhard Nesper, László Forró,, *Phys. Status Solidi B* **2010**; V. L. BinWang, Alistair J.Fielding, Robert A.W.Dryfe, *Carbon* **2020**, *160*, 236.

[18] M. M. Barney L Bales, Steve Smith, Miroslav Peric, *J. Phys. Chem. A* **2009**, *113*, 4930; H. A. F. Charles P. Poole, *Bull. Mag. Res.* **1979**, *1*.